Observations and modeling of the seismic rupture development based on the analysis of source time functions

Julien Renou

UNIVERSITÉ DE PARIS

Thèse préparée à l'Institut de Physique du Globe de Paris
École Doctorale STEP'UP – ED 560
IPGP – Équipe de Sismologie

Observations and modeling of the seismic rupture development based on the analysis of source time functions

par

Julien Renou

dirigée par
Martin Vallée et Pascal Bernard

Thèse de doctorat de Sciences de la Terre et de l'environnement

présentée et soutenue publiquement le
16 janvier 2020

devant un jury composé de

Françoise Courboulex	Directrice de recherche (Géoazur, Nice, France)	Rapportrice
František Gallovič	Associate professor (Charles University, Prague, République Tchèque)	Rapporteur
Soumaya Latour	Maître de conférences (Univ. P. Sabatier, Toulouse, France)	Examinatrice
Hélène Lyon-Caen	Directrice de recherche (ENS, Paris, France)	Examinatrice
Matthieu Causse	Chargé de recherche (ISTerre, Grenoble, France)	Examinateur
Martin Vallée	Physicien ajdoint (IPGP, Paris, France)	Directeur de thèse
Pascal Bernard	Physicien (IPGP, Paris, France)	Co-directeur de thèse

UNIVERSITÉ DE PARIS

Thèse préparée à l'Institut de Physique du Globe de Paris
École Doctorale STEP'UP – ED 560
IPGP – Équipe de Sismologie

Observations and modeling of the seismic rupture development based on the analysis of source time functions

par
Julien Renou

dirigée par
Martin Vallée et Pascal Bernard

Thèse de doctorat de Sciences de la Terre et de l'environnement

présentée et soutenue publiquement le
16 janvier 2020

devant un jury composé de

Françoise Courboulex	Directrice de recherche (Géoazur, Nice, France)	Rapportrice
František Gallovič	Associate professor (Charles University, Prague, République Tchèque)	Rapporteur
Soumaya Latour	Maître de conférences (Univ. P. Sabatier, Toulouse, France)	Examinatrice
Hélène Lyon-Caen	Directrice de recherche (ENS, Paris, France)	Examinatrice
Matthieu Causse	Chargé de recherche (ISTerre, Grenoble, France)	Examinateur
Martin Vallée	Physicien ajdoint (IPGP, Paris, France)	Directeur de thèse
Pascal Bernard	Physicien (IPGP, Paris, France)	Co-directeur de thèse

Institut de Physique du Globe de Paris – Équipe de Sismologie – 1 rue Jussieu, 75238 Paris cedex 05, France

Résumé

Notre compréhension de la physique de la source sismique, qui donne naissance à des séismes de toute magnitude, requiert l'observation d'une large population d'événements. Les méthodes d'analyse systématique de la sismicité mondiale remplissent ce rôle et permettent d'extraire les propriétés des séismes puis de les confronter aux modèles de rupture sismique. La méthode SCARDEC fait partie de ces méthodes et retrouve les fonctions source d'événements sur une large gamme de magnitudes ($M_w > 5.7$). La fonction source, puisqu'elle décrit l'évolution temporelle du taux de moment, est un observable privilégié pour l'analyse des propriétés transitoires de la rupture. L'objectif de notre étude est d'observer le développement de la rupture lors de ces séismes afin de plus précisément contraindre les modèles cinématiques et dynamiques de la source. La première partie de notre travail s'intéresse au développement des séismes à partir du catalogue SCARDEC. La phase menant au pic de la fonction source ("phase de développement") est extraite pour caractériser son évolution. À partir du calcul des accélérations de moment pour des taux de moment donnés, nous observons que l'évolution du taux de moment pendant la phase de développement est indépendante de la magnitude finale. Une analyse quantitative de l'augmentation du taux de moment en fonction du temps indique que cette phase ne respecte pas la dépendance en t^2 de la loi auto-similaire, suggérant une variation transitoire de la vitesse de rupture et/ou de la chute de contrainte. Ces observations sont dans un deuxième temps confrontées aux modèles cinématiques de la source. Un modèle de crack avec des variations radiales de la vitesse de rupture, associées à une faible chute de contrainte, met en évidence que la corrélation entre vitesse de rupture et vitesse de glissement est un ingrédient nécessaire au comportement transitoire de la phase de développement vu dans les observations. Nous générons ensuite à partir du modèle composite fractal RIK des catalogues synthétiques de fonctions source. Ces derniers montrent également que la corrélation entre la vitesse de rupture et la vitesse de glissement, ainsi que la durée du temps de montée, ont une influence sur les valeurs de l'accélération de moment. Nous développons finalement des modèles dynamiques hétérogènes qui prennent en compte la physique de la rupture. Les distributions hétérogènes du paramètre de friction D_c et de la contrainte initiale τ_0 sur la faille participent à générer des scénarios de rupture particulièrement réalistes. La propagation de la rupture est en particulier influencée par ces deux paramètres dynamiques qui entraînent une direction de propagation préférentielle couplée à une variabilité plus locale de la vitesse de rupture. La corrélation entre vitesse de rupture et vitesse de glissement, mise en lumière dans les modèles cinématiques précédents, est retrouvée et permet la reproduction des observations SCARDEC. Ces résultats devraient fournir des contraintes additionnelles pour la constitution de scenarios réalistes de la dynamique de la rupture.

Mots-clés : développement de la rupture, fonctions source, auto-similarité, cinématique de la source, chute de contrainte, vitesse de rupture, vitesse de glissement, modèles dynamiques

Summary

Our knowledge of earthquake source physics, giving rise to events of very different magnitudes, requires observations of a large population of earthquakes. The development of systematic analysis tools for the global seismicity meets these expectations, and allows us to extract the generic properties of earthquakes, which can then be integrated into models of the rupture process. Following this approach, the SCARDEC method is able to retrieve source time functions of events on a large range of magnitude ($M_w > 5.7$). The source time function (which describes the temporal evolution of the moment rate) is suitable for the analysis of transient rupture properties which provide insights into the generation of earthquakes of various sizes. The purpose of our study is to observe the rupture development of such earthquakes in order to add better constraints on kinematic and dynamic source models. The first part of our work focuses on the development of earthquakes through the analysis of the SCARDEC catalog. The phase leading to the peak of the source time function ("development phase") is extracted to characterize its evolution. From the computation of moment accelerations at prescribed moment rates, we observe that the evolution of the moment rate during the developement phase is independent of the final magnitude. A quantitative analysis of the moment rate increase as a function of time further indicates that this phase does not respect the steady t^2 self-similar growth, suggesting a transient variation of rupture velocity and/or stress drop. In a second part, these observations are compared with kinematic source models. A crack model with radial variations of the rupture velocity combined with low stress drop highlights that correlation between rupture velocity and slip velocity is a key feature for the transient behavior of the development phase previously observed. We then generate, using the composite fractal RIK model, synthetic catalogs of source time functions. This also supports that the correlation between rupture velocity and slip velocity, as well as the duration of the rise-time, have a strong effect on moment acceleration values. We finally develop heterogeneous dynamic models which take into consideration rupture physics. Heterogeneous distributions of the friction parameter D_c and the initial stress τ_0 contribute to generate highly realistic rupture scenarios. Rupture propagation is strongly influenced by these two dynamic parameters which induce a clear preferential direction of propagation together with a local variability of the rupture velocity. The correlation between rupture velocity and slip velocity highlighted by the previous kinematic models is retrieved and allows to reproduce the SCARDEC observations. These findings are expected to put further constraints on future realistic dynamic rupture scenarios.

Keywords : rupture development, source time functions, self-similarity, source kinematics, stress drop, rupture velocity, slip velocity, dynamic models

Remerciements

Ce paragraphe me donne l'occasion de remercier les personnes qui ont contribué de près ou de loin au bon déroulement de ces trois ans (et 3 mois !) de doctorat à l'IPGP. Mes premiers remerciements vont à mon jury de thèse, Françoise Courboulex, Frantisek Gallovic, Hélène Lyon-Caen, Soumaya Latour et Mathieu Causse, qui a accepté de juger mon travail et d'apporter des remarques constructives à ce manuscrit de thèse.

Je remercie mon co-directeur Pascal, et les membres de mon comité de thèse Alex et Claudio, pour leur présence lorsqu'il fallait discuter source sismique, mécanique des séismes, et même du choix de la "colorbar" ! Je remercie aussi Men-Andrin qui m'a donné l'opportunité de passer quelques semaines à Caltech et de vivre au plus près des laboratoires californiens. Je tiens à remercier également Pierre et Hideo qui ont accepté de participer à ce projet et m'ont initié à l'étude dynamique des séismes. En particulier, merci à toi Hideo pour ton implication et ta disponibilité, je garde un excellent souvenir de nos réunions du jeudi après-midi à l'ENS à discuter dynamique de la rupture. Enfin, je remercie bien sûr Martin, pour bien des raisons. Pour n'en citer que quelques unes, merci de m'avoir fait confiance dès le stage de master 2 puis de m'avoir ensuite guidé durant la thèse en étant toujours disponible et attentif à mes envies. J'ai beaucoup apprécié la complicité dans le travail que nous avons développée au cours de ces dernières années, et je te suis très reconnaissant d'avoir dépassé ta fonction de directeur lorsqu'il s'agissait de préparer mes prochains projets.

Ces trois dernières années ont aussi été l'occasion de rencontrer des personnes qui ont contribué à ce que je profite pleinement de cette thèse. Je remercie tous ces "vieux" doctorants et post-docs, qui ont su être bienveillants et à l'écoute quand j'avais des questions tant sur le plan scientifique que sur la gestion plus personnelle d'une thèse. Merci aux potes de la promo de master pour nos week-end d'aventuriers à la montagne et de manière générale pour cette belle amitié. Merci aux deux acolytes nantais expatriés à Paris pour notre séjour islandais et nos parties de baby-foot enflammées ! Merci aux potes vendéens pour ces journées d'été sur la côte qui faisaient oublier le quotidien parisien. Merci aux compères d'entraînement pour la natation, le vélo, la course à pied et le désormais mondialement connu FC IPGP ! Un merci tout particulier aux doctorants de l'équipe de sismologie de ma promotion graĉe à qui la rédaction de ce manuscrit durant les derniers mois de thèse aura été beaucoup moins déroutante. Je remercie également celles et ceux qui durant cette période m'ont permis de garder un pied dans le vrai monde. Enfin, merci à mes parents et ma sœur, dont la présence paraît naturelle mais a été indispensable depuis le début.

Table des matières

Table des figures

Préambule

Les séismes sont des événements soudains conduisant à relâcher, en partie sous forme d'ondes sismiques, la contrainte accumulée au niveau des failles. Les observables sismologiques sont donc porteurs d'information sur la source sismique, en plus de celles sur la complexité du milieu traversé. Les enregistrements de ces ondes révèlent une grande diversité parmi les séismes, en premier lieu à cause de leur taille très variable. Un séisme peut se produire sur une zone de quelques mètres, ou bien rompre des centaines de kilomètres de faille. Cette variété au sein de la dimension des événements soulève une question fondamentale : petits et grands séismes partagent-ils le même mécanisme de rupture ? Si oui, comment se développent-ils ? Pour répondre à cette question, il est nécessaire de pouvoir analyser les ondes générées par les séismes pour une large gamme de magnitude. Bénéficiant de la bonne résolution des données sismologiques à distance télésismique, le catalogue SCARDEC est un outil privilégié pour une analyse systématique de la sismicité mondiale. Cette base de données contient les fonctions source d'événements d'une magnitude variant de $M_w = 5.7$ à $M_w = 9.1$, et offrent par conséquent l'avantage de pouvoir extraire les propriétés de source pour des séismes de magnitudes variables. De par l'histoire spatio-temporelle de la rupture qu'elle décrit, la fonction source donne également l'opportunité d'étudier les phases transitoires du processus de rupture. Parmi celles-ci, cette thèse va se concentrer sur la caractérisation du développement de la rupture, dans le but de le relier à des modèles cinématiques et dynamiques des séismes.

Cette thèse s'organise en trois axes principaux et un chapitre d'introduction. Ce premier chapitre introduit tout d'abord les concepts fondamentaux de la source sismique et les principales relations entre les différents paramètres de source. Nous décrivons ensuite la méthode SCARDEC afin de présenter la base de données de fonctions source optimales qui constituent nos observations. Un aperçu des études utilisant cette base de données est fourni, de manière à identifier les propriétés globales auto-similaires et transitoires de la source. Les modèles théoriques de source sont finalement exposés pour distinguer les différents types de comportement proposés pour le développement de la rupture.

Dans le second chapitre, nous utilisons les fonctions source optimales comme observables du développement des séismes. En utilisant une méthode calculant les accélérations de moment à des taux de moment donnés, nous montrons que l'évolution du taux de moment vers le pic de la fonction source est indépendante de la magnitude du séisme. Une analyse quantitative de l'augmentation du taux de moment nous permet d'extraire le comportement caractéristique de la phase de développement des séismes. Les observations sont mises en relation avec le cas de la croissance d'un crack auto-similaire.

Le chapitre 3 explore les origines de nos observations à partir de modèles cinématiques de la source. Une première analyse utilise la base de données $SRCMOD$ rassemblant des distributions du glissement de séismes afin de calculer la chute de contrainte sur les zones les plus actives de la faille considérées comme représentatives de la phase de développement. Un modèle de crack avec des variations radiales de la vitesse de rupture est ensuite développé afin d'estimer l'effet de la variabilité de la vitesse de rupture et de la valeur de la chute de contrainte sur la phase de développement. Le modèle composite RIK, dont la distribution du glissement est fractale, est utilisé pour générer des fonctions source diverses. Nous estimons le rôle d'une vitesse de rupture variable et du temps de montée sur les valeurs d'accélération de moment.

Enfin dans la chapitre 4, nous utilisons des modèles dynamiques afin d'avoir une description complète du processus de rupture lors de la phase de développement. Des distributions hétérogènes du paramètre de friction D_c et de la contrainte initiale sont imposées sur la faille et génèrent des propagations complexes de la rupture. Nous estimons l'effet de ces deux paramètres dynamiques sur le comportement des paramètres cinématiques durant la phase de développement.

Cette thèse se conclut par une synthèse des résultats obtenus et des perspectives d'amélioration des modèles développés dans les précédents chapitres. Nous mentionnons finalement les implications de nos travaux pour la dynamique de la source.

Chapitre 1

L'apport des fonctions source : de la description globale des séismes à celle du détail de leurs processus

Ce premier chapitre aborde dans un premier temps les principales notions nécessaires à la description de la source sismique, avec un accent mis sur le lien entre la taille finale d'un séisme et les paramètres globaux de la rupture. Les principales étapes de la méthode SCARDEC sont ensuite exposées afin d'introduire le lecteur à la fonction source qui est l'observable principal de ce manuscrit. Dans un second temps, un bilan des études utilisant la richesse d'informations du catalogue sur le processus de rupture permet d'aborder le concept d'auto-similarité. Enfin, ce chapitre se termine par une description plus détaillée sur le développement de la rupture sismique, avec l'analyse des propriétés des fonctions source dans leur période de croissance en lien avec les modèles théoriques de propagation de la rupture.

1.1 Généralités sur la source sismique

Un séisme est la conséquence d'une augmentation des contraintes tectoniques le long d'une zone de faiblesse existante, appelée faille. Lorsque la contrainte exercée sur cette faille devient trop importante, la déformation accumulée est rapidement relâchée et les deux blocs séparés par la faille glissent. L'état de contrainte global de la zone rompue avant et après le séisme n'étant pas connu, une grandeur caractéristique associée à un séisme est la chute de contrainte. Puisque la modification de la contrainte est à l'origine du glissement le long de la faille, la vision statique d'un séisme est résumée par la relation liant le glissement moyen D à la chute de contrainte statique moyenne $\Delta\sigma$:

$$\Delta\sigma \;=\; c\mu\frac{D}{L}, \tag{1.1}$$

avec c une constante, μ la rigidité du milieu environnant et L la longueur caractéristique de la faille. Même si la distribution de la contrainte initiale est très hétérogène sur le plan de faille, conduisant à une variation spatiale complexe du glissement et de la chute de contrainte statique, l'équation 1.1 est une robuste approximation pour estimer les paramètres globaux de la rupture. Elle implique que la valeur de la chute de contrainte est notamment contrôlée par le rapport entre D et la longueur caractéristique L.

Afin de quantifier la taille des séismes et d'apporter un éclairage sur les processus les caractérisant, la théorie de la dislocation élastique est appliquée à la sismologie. Le moment sismique M_0 est utilisé pour définir la taille d'un séisme (Aki, 1967). Une faille de surface S avec un glissement D est représentée par un système de forces double couple dont le moment M_0 pour chaque couple s'écrit comme

$$M_0 \;=\; \mu DS, \tag{1.2}$$

avec S la surface de la faille rompue. L'amplitude des ondes longue-période générées par le séisme est proportionnelle à M_0, qui peut donc être évalué une fois la géométrie de la source et les effets de propagation corrigés. En considérant μ comme un paramètre variant peu pour les séismes peu profonds, un séisme avec un fort moment sismique est donc la résultante d'un glissement important sur une grande surface, ce qui implique également une grande valeur pour L. Cette relation entre D et L a une conséquence importante,

en particulier sur l'évolution de la chute de contrainte en fonction du moment sismique. Si ces deux paramètres augmentent en moyenne de la même manière, alors la chute de contrainte est constante pour tous les séismes. Plus précisément, pour une faille de longueur L et largeur l proportionnelles ($S \propto L^2$), on peut écrire grâce aux équations 1.1 et 1.2 :

$$\Delta\sigma \propto \frac{M_0}{L^3}. \tag{1.3}$$

C'est dans cette optique que des études estimant le moment sismique puis les dimensions de la faille ont été menées pour déterminer la valeur moyenne de la chute de contrainte sur des larges gammes de moment sismique (Chinnery, 1964; Kanamori and Anderson, 1975; Abercrombie and Leary, 1993). Ces analyses suggèrent une valeur variable en fonction des séismes mais sans dépendance systématique du moment sismique, et indiquent par conséquent un processus de relâchement de contraintes similaire quel que soit la taille des séismes.

Au-delà de son aspect purement spatial, un séisme est une fracture qui s'initie à l'hypocentre et se propage le long de la faille en un temps fini. Une vitesse de rupture intervient donc dans la caractérisation de la rupture et quantifie la rapidité avec laquelle la surface de faille va être rompue. Dans un cas de figure simple, on considère une rupture bidimensionnelle et bilatérale, c'est-à-dire que le front de rupture utilise les deux dimensions de la faille, sans direction préférentielle de propagation. Dès lors, ce front de rupture est circulaire et la longueur caractéristique L devient le rayon de ce cercle. À la fin du séisme, si l'on suppose une vitesse de rupture V_r constante, L est égale à $V_r \times T$ avec T la durée totale du séisme. Cette hypothèse permet d'exprimer la taille d'un séisme en fonction de sa durée totale sous la forme

$$M_0 \propto \Delta\sigma V_r^3 T^3, \tag{1.4}$$

et introduit ainsi la notion d'auto-similarité de la rupture, qui sera largement discutée tout au long de ce manuscrit. L'auto-similarité des séismes est une notion développée par Aki (1967) selon laquelle petits et grands séismes sont issus d'un seul et même phénomène physique. Les grands événements sont seulement des versions mises à l'échelle des événements plus petits, sans caractéristiques qui leur sont propres. Cette définition implique donc que la chute de contrainte et la vitesse de rupture sont indépendantes de la taille finale de la source, qui est elle uniquement contrôlée par sa durée totale.

En conséquence, la loi théorique 1.4 a été confrontée aux observations afin de vérifier la dépendance du moment sismique comme le cube de la durée du séisme, confirmant ou non son indépendance avec les paramètres tels que V_r et $\Delta\sigma$. Une première approche est d'analyser le spectre des ondes télésismiques U, à partir d'un spectre théorique utilisant le modèle de source "ω-squared" de Brune (1970)

$$U(f) = \frac{U(0)}{1 + (f/f_c)^2}. \tag{1.5}$$

Ce spectre est caractérisé par un plateau à basse fréquence $U(0)$, proportionnel à M_0, une fréquence coin f_c puis une décroissance inversement proportionnelle au carré de la fré-

quence. f_c est un observable proportionnel à l'inverse de la durée T dans des modèles à V_r constant (avec un coefficient dépendant de la géométrie de la rupture), i.e. $M_0 \propto \Delta\sigma f_c^{-3}$. (Boore, 1983; Boatwright and Choy, 1992). Allmann and Shearer (2009) ont testé ces hypothèses de $\Delta\sigma$ et V_r constants en compilant toutes les études qui permettent d'associer f_c et M_0 des séismes à l'échelle globale. Ils montrent distinctement sur un intervalle de magnitude allant de 10^9 à 10^{22} Nm.s^{-1} un comportement auto-similaire (Figure 1.1). Les droites en pointillés Figure 1.1 de pente $-1/3$ en échelle log-log donnent une estimation des valeurs extrêmes de $\Delta\sigma$, allant de 0.1 à 100 MPa. La même analyse sur l'accord des paramètres de source à la loi auto-similaire a été effectuée dans le domaine temporel, afin de directement comparer les observations à la loi 1.4. Furumoto and Nakanishi (1983) sont parmi les premiers à estimer une durée de source à partir du modèle d'Haskell (Haskell, 1964) en tirant profit du spectre des ondes de surface longue-période. Vidale and Houston (1993) utilisent le contenu courte-période des ondes télésismiques enregistrées dans un dense réseau régional, puis Houston et al. (1998) exploitent plus largement les sismogrammes large-bande pour estimer la durée de la source d'événements à différentes profondeurs. Au-delà de la différence de comportement observée dans ces études entre événements superficiels et profonds, qui n'est pas développée dans ce manuscrit, la principale observation est la distincte augmentation de la durée des séismes comme le cube du moment sismique. Dès lors, l'équation 1.4 sert de référence pour considérer le comportement global des séismes comme auto-similaire. À l'inverse, tout comportement déviant de cette loi est considéré comme atypique, et implique des dépendances de certaines propriétés de la source avec le moment sismique final.

1.2 La méthode SCARDEC : accès à un catalogue de fonctions source pour une description complète de la rupture

Une étape supplémentaire dans la caractérisation du processus de rupture est d'évaluer son évolution temporelle afin d'extraire des paramètres cinématiques. La fonction source remplit ce rôle puisqu'elle offre une vision intégrée sur la faille de la vitesse de glissement au cours du temps. Cette histoire spatio-temporelle de la rupture est décrite par le taux de moment $\dot{M}(t)$ sous la forme :

$$\dot{M}(t) \;=\; \mu \int_S \dot{u}\, \mathrm{d}S, \tag{1.6}$$

avec μ la rigidité considérée constante, $\dot{u}$ la vitesse de glissement et S la surface rompue au temps t. Cette relation montre explicitement que le taux de moment est dépendant de la vitesse de glissement et de la surface rompue, résultant à un temps t en un fort taux de moment quand une grande surface de faille est rapidement activée. Les grandeurs telles que la durée de la source T et le moment sismique M_0 introduites dans la Section 1.1 correspondent à la durée de la fonction source et à son intégrale temporelle, respectivement.

Les fonctions source, appelées STFs (Source Time Functions) dans la suite de ce manuscrit, sont sous certaines hypothèses liées aux déplacements enregistrés à distance dite télésismique, qui correspond à une distance épicentrale Δ comprise entre 30° et 90°. À cette

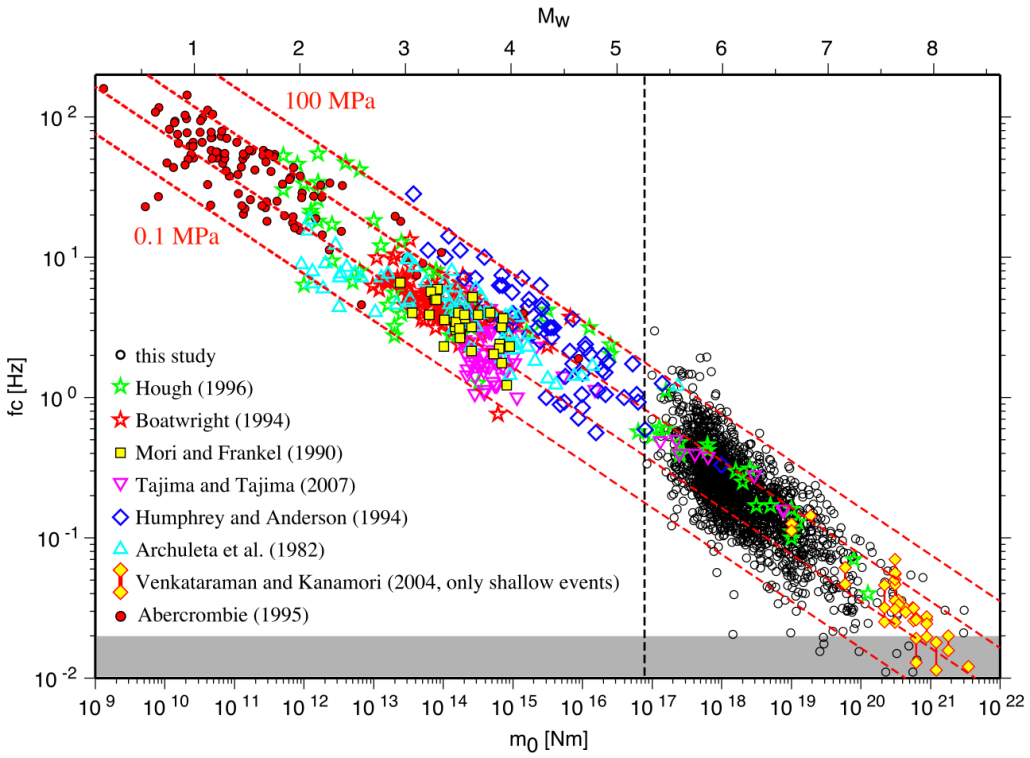

Figure 1.1 – Estimation de la fréquence coin f_c en fonction du moment sismique et de la magnitude pour un ensemble d'études. Les lignes rouges en pointillés ont une pente de $-1/3$ pour indiquer le comportement auto-similaire. La compilation de tous les résultats indiquent que les valeurs de chute de contrainte sont comprises entre 0.1 MPa et 100 MPa. Graphique issu de Allmann and Shearer (2009).

distance suffisamment lointaine de la source, le champ lointain du déplacement prédomine car la longueur d'onde est beaucoup plus petite que la distance source-station. Dans le même temps, cette distance source-station est bien supérieure aux dimensions de la source, ce qui implique que le rayonnement des ondes est approximé par un "point-source". Cette représentation simple d'un séisme implique que dans un milieu infini non-atténué, la fonction source correspond au déplacement de l'onde P, en prenant en compte le diagramme de radiation, la distance à la source et les propriétés élastiques du milieu. Cependant, l'hypothèse d'une source ponctuelle n'est plus vérifiée pour des séismes de magnitude importante, dont l'extension spatiale induit un effet "directif". Cet effet a pour conséquence une représentation différente de la fonction source en fonction de la position de la station, appelée fonction source apparente (ASTF). La méthode SCARDEC (Vallée et al., 2011) a été développée dans le but de prendre en compte cette complexité de la source sans introduire d'hypothèses simplificatrices sur le processus de rupture. Son approche déconvolutive permet d'obtenir différentes ASTFs à chaque station et ainsi s'affranchir de la représentation ponctuelle de la source, tout en retrouvant les caractéristiques globales des séismes (moment sismique, mécanisme au foyer et profondeur). La détermination de ces caractéristiques de source est faite de manière systématique, 45 minutes après le déclenchement de séismes modérés à forts, et est disponible via le lien `http://geoscope.ipgp.fr`. Une version consolidée de ce catalogue, intégrant également les séismes passés depuis 1992 a été rendue disponible sur le lien `http://scardec.projects.sismo.ipgp.fr` (Vallée and Douet, 2016). La méthode SCARDEC, détaillée dans Vallée et al. (2011), est résumée

ci-dessous, et donne naissance à un catalogue de STFs qui sera par la suite notre base observationnelle du processus sismique.

Les ondes de volumes utilisées dans la méthode SCARDEC sont issues des stations FDSN (Federation of the Digital Seismograph Newtork), dans la gamme télésismique ($30° < \Delta < 90°$). L'analyse débute par une estimation de la durée du séisme, difficilement visible dans les signaux bruts notamment en raison de l'interférence entre les ondes directes et les phases de profondeur (pP, sP, sS). Pour les grands séismes ($M_w > 7$), le déplacement vertical est filtré entre 1 Hz et 3 Hz, puis une estimation de la durée est faite dans cette bande de fréquence où l'onde P directe domine le signal. Pour les séismes plus petits, l'équation GCMT (Ekström et al., 2012) est appliquée (voir Figure 1.2). Cette durée est ensuite légèrement augmentée pour déterminer le moment sismique du séisme.

Les ondes à distance télésismique ont la particularité d'être relativement simplement modélisables en raison de la relative homogénéité du manteau. Le calcul de la propagation des ondes dans ce milieu peut être effectué par des techniques basées sur la théorie du rai sismique. Les fonctions de Green des phases directes (P et SH) et réfléchies (PP, SS, PcP et ScS) sont calculées par la méthode de Bouchon (1976) associée à la méthode de réflectivité de Müller (1985). L'inclusion des phases de profondeur dans l'analyse est nécessaire pour les séismes superficiels car leurs arrivées se font avant la fin du passage des ondes directes aux stations. Les temps de trajet des ondes sont calculés par le biais du modèle de Terre radial IASP91 (Kennett and Engdahl, 1991), dans lequel l'expansion géométrique et l'atténuation anélastique du manteau sont également prises en compte.

L'isolation des ondes de volume et la robuste modélisation de leurs fonctions de Green permettent d'introduire l'approche déconvolutive. Pour une Terre radiale, le théorème de représentation (Aki and Richards, 2002) pour une ligne-source permet d'exprimer le déplacement $U(t)$ comme un produit de convolution de la forme :

$$U(t) \;=\; G^0_{\phi,\delta,\lambda}(z_c, t) * F(t), \tag{1.7}$$

avec $G^0_{\phi,\delta,\lambda}(z_c, t)$ le champ d'ondes généré à l'hypocentre par un mécanisme double-couple d'azimut, pendage, rake et profondeur ϕ, δ, λ et z_c respectivement. $F(t)$ est la fonction source apparente propre à chaque station, et peut donc être obtenue via la déconvolution de $G^0_{\phi,\delta,\lambda}(z_c, t)$ à partir de $U(t)$. La stabilité de l'approche déconvolutive est assurée par cinq conditions physiques sur F qui doivent être simultanément satisfaites :

(i) F est positive ;
(ii) F est causale ;
(iii) F a une durée finie ;
(iv) L'intégrale de F est constante à toutes les stations ;
(v) F varie peu entre les stations.

L'ajout de ces conditions permet de contraindre suffisamment la déconvolution pour que les paramètres de source et les ASTFs puissent être correctement retrouvés par une procédure d'inversion.

Les paramètres de source ϕ, δ, λ et z_c sont dans un premier temps estimés à partir des signaux filtrés dans une bande de fréquences donnée (Figure 1.3a)). La limite basse

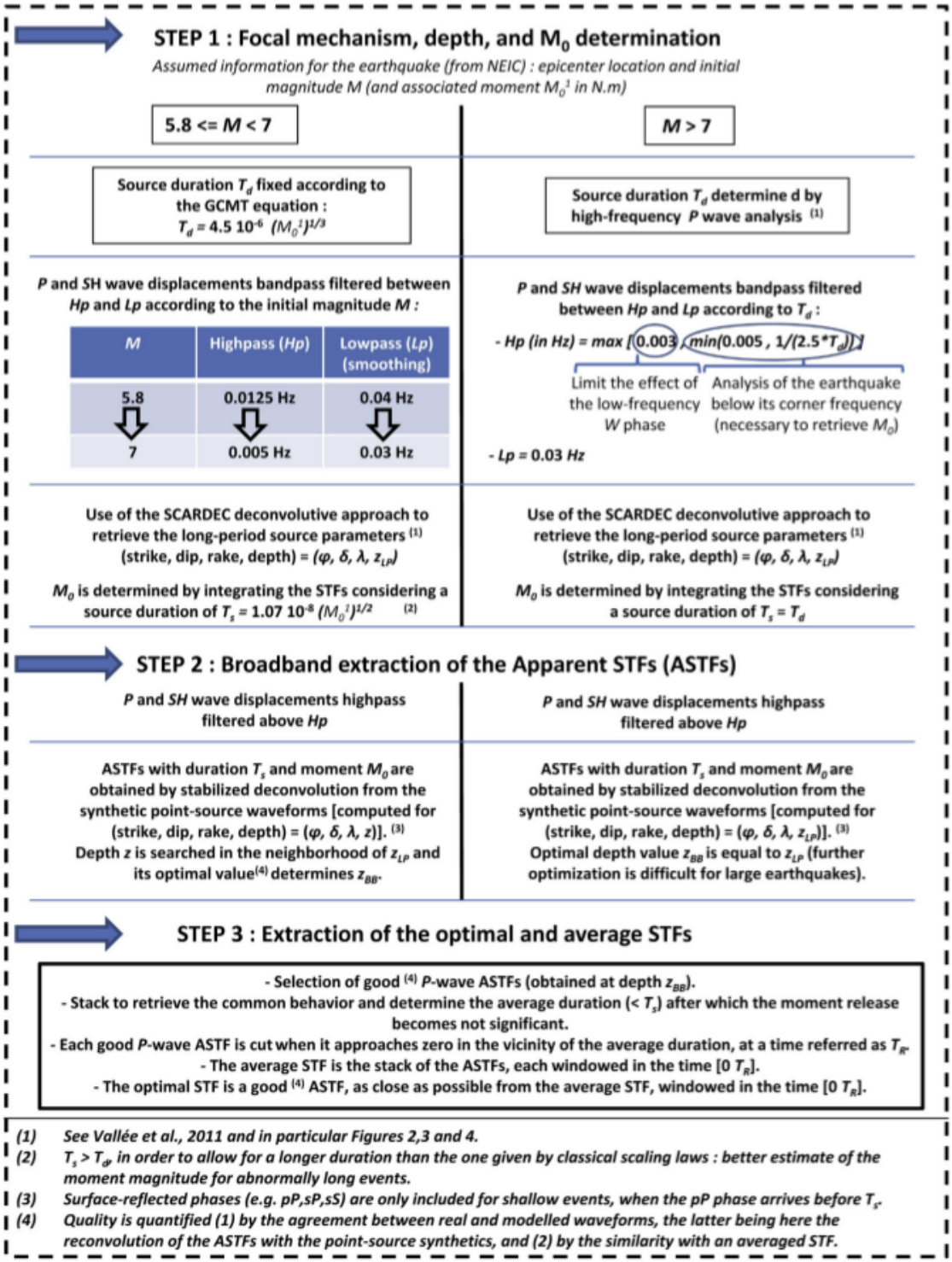

Figure 1.2 – Résumé de la méthode SCARDEC issu de Vallée and Douet (2016). Trois principales étapes sont nécessaires pour obtenir les fonctions source moyenne et optimale. La première étape optimise la valeur des paramètres de source à partir du contenu basse fréquence. La seconde étape utilise une plus grande gamme de fréquence afin d'obtenir les fonctions source relatives (ASTFs) à chaque station. La dernière étape extrait les fonctions source moyenne et optimale. À noter que la méthode diffère légèrement entre les séismes de magnitude modérée ($5.5 < M_w < 7$) et forte $M_w > 7$.

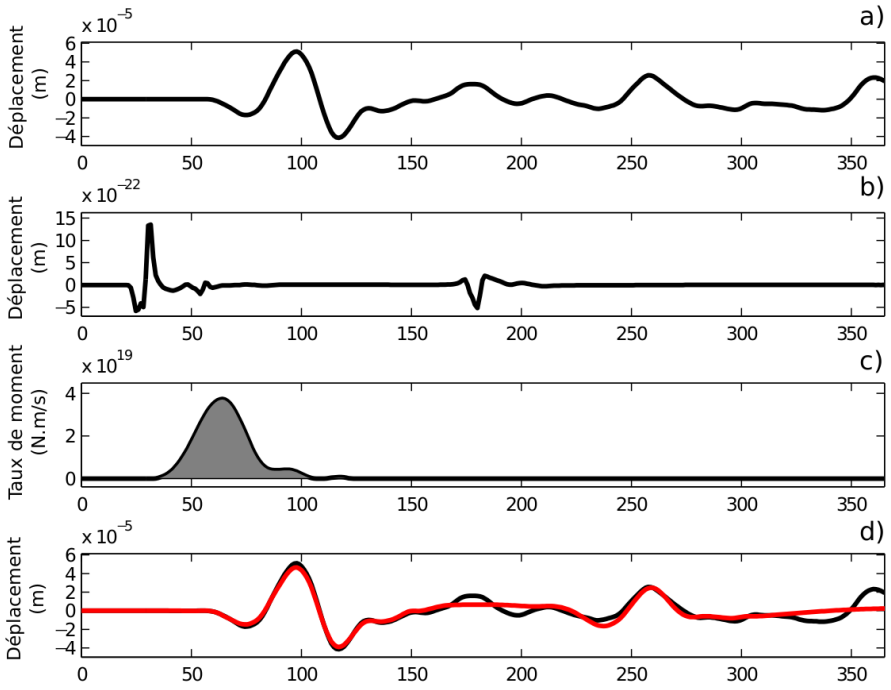

Figure 1.3 – Exemple de la procédure de déconvolution pour la station NWAO pour le séisme de Gorkha (15 avril 2015, M_w 7.9). a) Composante vertical des signaux filtrés. b) Fonction de Green $G^0_{\phi,\delta,\lambda}(z_c,t)$ incluant les ondes directes et réfléchies calculée pour le jeu de paramètres optimal. c) Fonction source apparente obtenue après la déconvolution de b) par a). d) Comparaison entre données brutes et synthétiques. Cette illustration est issue de la thèse de doctorat d'Agnès Chounet (Chounet, 2018).

fréquence varie de 0.0125 Hz pour les séismes de plus faibles magnitudes à 0.003 Hz pour les plus grands afin de ne pas prendre en compte la phase W (Kanamori and Rivera, 2008) tout en ayant une valeur inférieure à la fréquence coin. Un filtre passe-bas est également utilisé dans cette étape, dont le but est de retrouver les caractéristiques moyennes de l'événement. Une première déconvolution de $G^0_{\phi,\delta,\lambda}(z_c,t)$ sur les signaux filtrés est effectuée en tenant compte des hypothèses (i) à (iii), à partir de laquelle le moment sismique des ASTFs est extrait. Le jeu de paramètres ϕ, δ, λ et z_c optimal est alors déterminé grâce à une seconde déconvolution incluant les conditions (iv) et (v) et le moment sismique déterminé précédemment. La détermination du jeu optimal dans l'inversion est basée sur la capacité de ces ASTFs contraintes à expliquer les données, une fois reconvoluées par $G^0_{\phi,\delta,\lambda}(z_c,t)$ (Figure 1.3d)).

A la suite de la procédure d'inversion, une seconde étape consiste à inclure le contenu haute fréquence des sismogrammes afin d'obtenir des ASTFs dont le détail n'est pas contraint par un filtre passe-bas. Une déconvolution finale basée sur la même approche et avec les paramètres de sources optimaux est effectuée. Il ressort de cette étapes deux jeux d'ASTFs, l'un issu des ondes SH, l'autre des ondes P. Par la suite, seules les ASTFs de l'onde P sont utilisées pour déterminer les fonctions moyennes et optimales de chaque séisme. Comme défini précédemment, les ASTFs diffèrent à chaque station, ce qui ne donne pas un accès direct à la fonction source absolue. Un moyen utilisé pour la reproduire est de calculer une fonction source moyenne et optimale. La fonction source moyenne est le "stack" des ASTFs après avoir été corrélées en temps (pour corriger des imprécisions de temps d'arri-

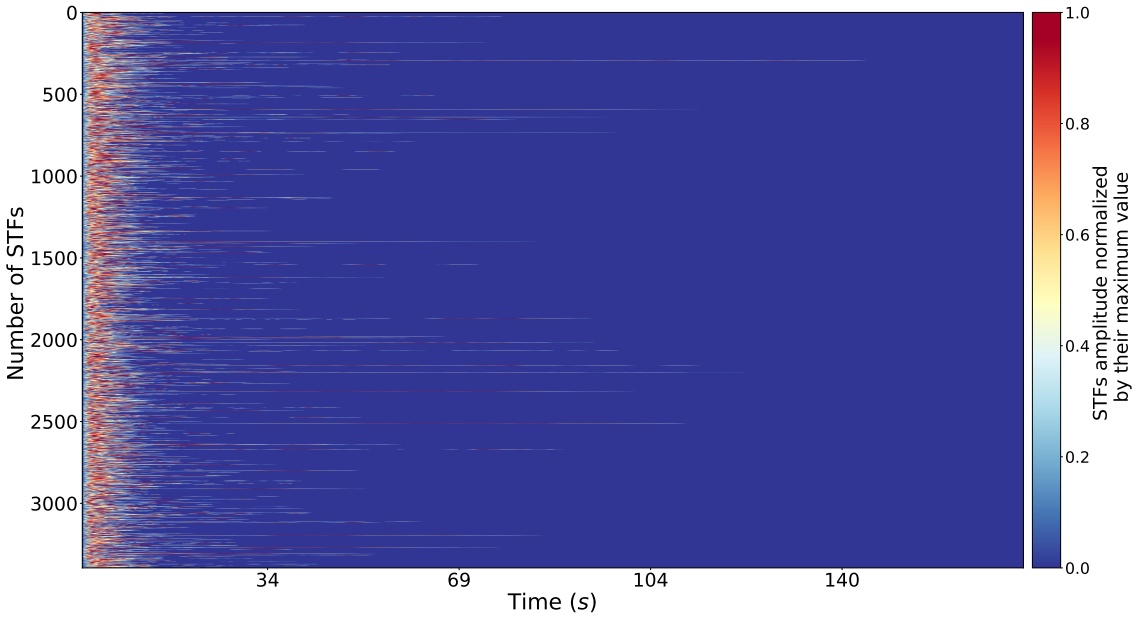

Figure 1.4 – Représentation des 3395 fonctions source optimales du catalogue SCARDEC de 1992 au 31 décembre 2017. Chaque ligne représente une STF avec son amplitude normalisée par rapport au maximum de la fonction. Les magnitudes varient de 5.5 à 9.1 avec le séisme de Tohoku-Oki en 2011.

vée). Cette opération a pour but d'obtenir une STF qui réduit l'effet directif et certaines caractéristiques présents uniquement dans quelques ASTFs. En contrepartie, la fonction source moyenne subit un lissage, qui tend à faire disparaître des variations de courte période. Pour des mesures locales, ce lissage peut avoir des conséquences, par conséquent une fonction source optimale est également extraite, et correspond à l'ASTFs la plus proche de la fonction source moyenne. Elle revêt donc l'avantage de conserver l'ensemble du contenu fréquentiel des données originales tout en étant peu affectée par l'effet directif. L'ensemble des étapes menant à l'obtention du catalogue de STFs est résumé Figure 1.2. À partir de 1992 et jusqu'au 31 décembre 2017, le catalogue SCARDEC contient 3395 STFs d'événements allant d'une magnitude 5.5 à 9.1 avec le séisme de Tohoku-Oki. La Figure 1.4 représente le catalogue : chaque ligne est une STF dont l'amplitude est normalisée par la valeur maximum de la fonction. La longueur des lignes donne une indication sur la durée des STFs. À noter qu'à l'instar du catalogue NEIC-PDE, le catalogue SCARDEC montre que les séismes analysés suivent une loi de Gutenberg-Richter illustrée dans la figure par le grand nombre de séismes ayant une courte durée.

Les limitations de la méthode SCARDEC sont détaillées dans Vallée and Douet (2016), et une attention particulière est portée dans ce manuscrit à la précision du temps hypocentral des STFs. Le temps hypocentral NEIC-PDE est tout d'abord défini comme le temps 0 de chaque ASTF de notre étude. L'hypothèse d'une terre sphérique pour établir le début des ASTFs est une source d'incertitude sur le début des ASTFs, car le calcul des temps de trajet entre le séisme et la station ne rend pas compte des hétérogénéités du milieu traversées par les ondes. Ce biais a été confirmé par une étude de Chounet et al. (2017) où un modèle de Terre 3D améliore le temps d'origine prédit des ASTFs. Afin de calculer la STF moyenne, une recorrélation en temps de toutes les ASTFs est effectuée afin d'obtenir un coefficient de corrélation maximal. Le temps 0 est ensuite désigné comme le temps où

le premier moment sismique est libéré dans la fonction source optimale. Pour des ASTFs cohérentes et avec un clair début, ce temps 0 peut être précisément recalculé. Cependant, l'effet directif génère des ASTFs avec des durées différentes, qui peuvent débuter par des phases peu impulsives pour certaines ASTFs. Ces phases sont vues comme les premiers moments sismiques libérés, mais peuvent être apparues dans le processus de déconvolution à cause d'une mauvaise modélisation de la source et/ou du milieu. Ces écarts de quelques secondes sont en particulier non négligeables pour les séismes faibles et modérés, et doivent être traités en conséquence.

Ces incertitudes impliquent donc que la richesse d'information présente dans le catalogue SCARDEC ne doit pas faire oublier que les références des temps des STFs ne sont pas les paramètres les mieux contraints. Certaines études faites à partir de cette base de données et détaillées dans le paragraphe suivant en prennent compte et déterminent par exemple la durée des STFs de manière indirecte.

1.3 Propriétés globales et transitoires extraites des catalogues de fonctions source et leur lien avec les modèles de rupture

1.3.1 Paramètres de source macroscopiques

Ce paragraphe fait le bilan des études qui ont utilisées le catalogue SCARDEC de manière exhaustive pour caractériser le processus sismique. Le nombre sans précédent de STFs permet d'obtenir des statistiques robustes sur les paramètres de source sur une large gamme de magnitude. En particulier, ces études sont une alternative aux méthodes classiques décrites dans le paragraphe 1.1 car (1) la mesure de la fréquence coin f_c ne contient pas le spectre large-bande de la STF et (2) des observables sur la gamme de magnitude SCARDEC sont souvent issus de méthodes d'extraction différentes qui empêchent une comparaison objective.

Les premières applications tirant profit du catalogue ont cherché à confirmer la comportement auto-similaire à l'échelle globale de tous les séismes superficiels. Cette tendance est confirmée par Vallée (2013), où la loi 1.4 est respectée lorsque la durée totale T est estimée à partir des fonctions source et comparée au moment sismique M_0. Les hypothèses de chute de contrainte $\Delta\sigma$ et de vitesse de rupture V_r constantes sont particulièrement explorées par Courboulex et al. (2016) et Chounet et al. (2017) respectivement, et leur approche quantitative révèle une indépendance de ces deux paramètres avec la magnitude. Ces trois études citées s'inspirent notamment des limitations exposées dans le paragraphe 1.2, et calculent la durée totale comme $T = 2M_0/F_m$ avec F_m le pic de la fonction source. L'incertitude sur le temps hypocentral et la fin du séisme est alors de moindre importance, et permet des extractions robustes de la variabilité des paramètres de source, comme en témoigne la faible valeur de l'écart-type de $\Delta\sigma$ de Courboulex et al. (2016) par rapport aux analyses faites à partir de la fréquence coin.

Ces caractéristiques communes pour les séismes superficiels n'empêchent pas pour autant des disparités dues au contexte tectonique dans lequel s'effectue la rupture. Chounet and Vallée (2018) remarquent par exemple que les séismes de subduction sont en moyenne plus

longs et moins impulsifs que les autres événements. Cette observation est cohérente avec les faibles valeurs de $\Delta\sigma$ de Courboulex et al. (2016), car d'après l'équation 1.4, à vitesse de rupture constante, $\Delta\sigma$ est proportionnel à M_0/T^3 et donc proportionnel à F_m^3/M_0^2.

1.3.2 Propriétés transitoires et déterminisme

Les analyses précédentes tirent profit d'une seule mesure au sein de chaque STF (T, F_m) pour déduire le comportement de paramètres macroscopiques ($\Delta\sigma$, V_r, énergie radiée), donnant par conséquent une vision globale des séismes. Cependant, l'évolution du taux de moment tout au long du séisme est un observable idéal pour (1) reconstruire l'histoire temporelle du processus de rupture et identifier plusieurs phases transitoires au sein des STFs et (2) estimer si l'auto-similarité est un phénomène précoce durant la rupture ou seulement une signature finale des séismes. L'étude de Denolle (2019) utilise toutes les STFs pour statistiquement estimer l'énergie radiée des séismes au cours du temps. La tendance globale indique que la phase de croissance est plus énergétique que la phase d'arrêt de la rupture pour toute la gamme de magnitude du catalogue. L'analyse détaillée de chaque STF conduit également à observer sa complexité, comme le montre Danré et al. (2019) en considérant un séisme comme un ensemble de sous-événements. Ils remarquent que leur nombre croît avec la taille du séisme, mais surtout que l'observation des premiers sous-événements peut potentiellement contenir une information sur la magnitude finale du séisme.

Dans la même optique, deux récentes études se sont focalisées sur l'existence d'un signal déterministe permettant d'estimer si petits et grands séismes partagent un comportement similaire. L'objectif est de détecter si un signal corrélé avec le moment sismique final d'un séisme apparaît bien avant que le séisme ne se termine. Melgar and Hayes (2019) utilisent une approche calculant les pentes moyennes des STFs en divisant le taux de moment par une durée comprise entre le temps hypocentral et plusieurs temps donnés. Une corrélation entre ces pentes et la magnitude apparaît, à partir d'un temps de 10 s. Cette observation s'explique principalement par le fait qu'un temps donné est une fraction plus ou moins conséquente de la durée totale d'un séisme, en fonction de sa magnitude. À partir de temps supérieurs à 10 s, la pente moyenne pour des séismes de faibles magnitudes est statistiquement calculée dans une zone aux alentours du pic voire même de déclin des STFs, résultant en une valeur relativement faible. À l'inverse, à ces même temps, les grands séismes sont majoritairement en plein développement, ce qui induit des valeurs de pentes moyennes relativement fortes. Cette étude est par conséquent utile pour estimer le temps auquel petits et grands séismes se différencient, mais n'implique qu'un "weak determinism" car le signal dépendant de la magnitude n'apparaît que lorsque les séismes du catalogue ont relâché une partie significative de leur moment sismique final. Le travail de Meier et al. (2017) est la seconde étude traitant du comportement déterministe des séismes à partir du catalogue SCARDEC. Ils s'intéressent à la forme standard des STFs en s'affranchissant de la complexité intrinsèque de ces fonctions. La Figure 1.5 reproduit leur méthode qui consiste à utiliser les STFs d'événements supérieurs à $M_w = 7$ et à calculer les médianes des STFs à plusieurs magnitudes cibles. Pour chacune d'entre elles, les 20 STFs avec les magnitudes les plus proches de la magnitude cible sont sélectionnées, et à chaque temps le point médian est calculé. Les STFs avec des magnitudes cibles proches de 7 sont

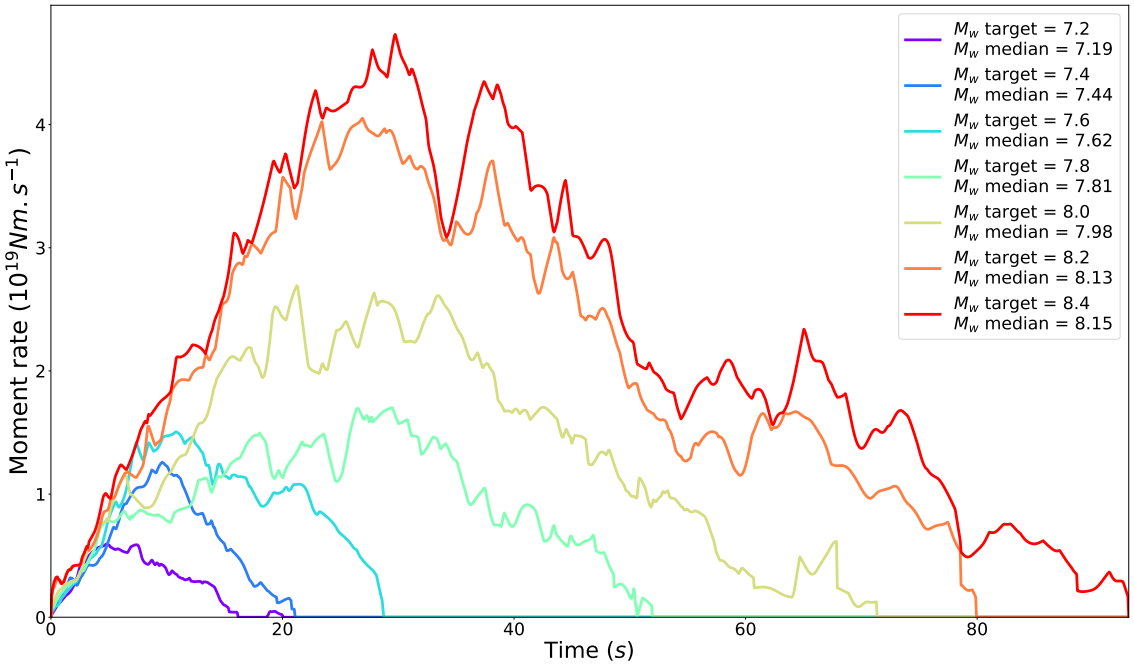

Figure 1.5 – Médianes des STFs calculées par la méthode de Meier et al. (2017). Pour chaque magnitude cible entre 7.2 et 8.4, les 20 STFs avec les magnitudes les plus proches sont utilisées pour calculer la médiane des STFs. La magnitude médiane des 20 STFs est écrite sous chaque magnitude cible. La croissance des médianes est similaire jusqu'à ce qu'elles atteignent leur pic, impliquant un comportement universel des séismes dans la gamme de magnitude analysée.

nombreuses, et la magnitude médiane des 20 STFs sélectionnés est équivalente. Peu de STFs sont proches de la magnitude cible 8.4, ce qui induit donc que la magnitude médiane des 20 STFs sélectionnées sera plus faible. Leur résultat montre une croissance similaire des médianes quel que soit leur intervalle de magnitude, ce comportement universel des séismes ne permettant donc pas d'isoler un signal déterministe avant que la rupture soit dans une phase de déclin. Malgré ce comportement similaire des séismes lorsqu'ils croissent, le terme d'auto-similarité ne peut pour autant être employé, car la croissance des médianes des STFs est linéaire. Comme nous allons le voir dans la partie suivante, le respect d'un comportement auto-similaire à n'importe quel instant de la rupture requiert davantage de contraintes sur l'évolution du taux de moment. Désormais, la croissance des STFs va être la base observationnelle de notre étude, et sera le témoin du développement de la rupture sismique.

1.3.3 Modèles cinématiques du développement de la rupture

La représentation cinématique de la rupture est issue des modèles de source finie et étendue qui permettent de simuler la radiation des ondes. L'approximation d'un séisme est faite en considérant la propagation d'un glissement le long d'un plan de faille, de manière à pouvoir ensuite extraire toutes les caractéristiques de la rupture, et notamment la fonction source. Le modèle de dislocation d'Haskell (Haskell, 1964) est un des premiers modèles reproduisant certaines propriétés importantes des séismes avec une configuration telle qu'un front de rupture linéaire se propage à vitesse constante unilatéralement d'un côté à l'autre d'une faille rectangulaire. Derrière ce front de rupture, un glissement constant se

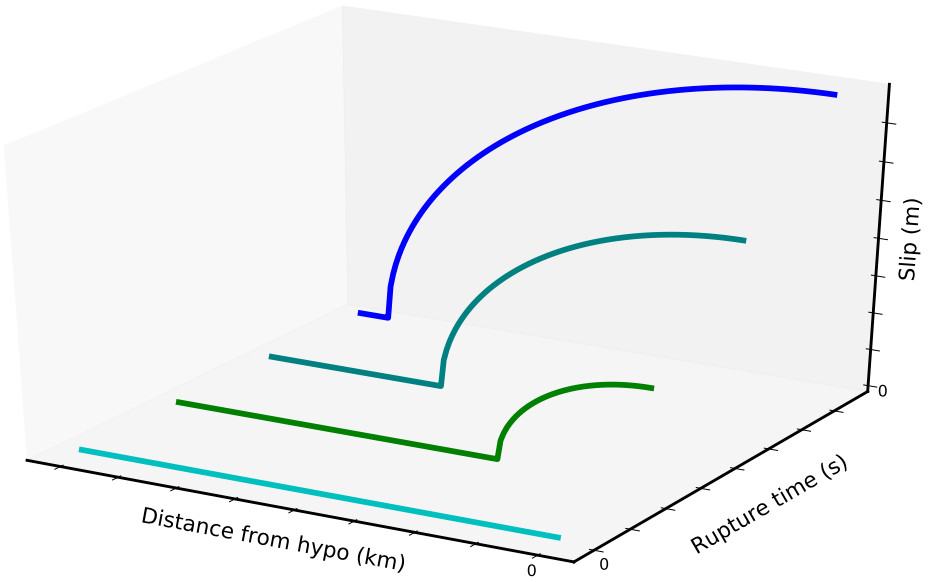

Figure 1.6 – Glissement du modèle de crack circulaire auto-similaire dépendant du temps et de la distance. À chaque temps, le glissement est nul sur le front de rupture et maximum à l'hypocentre.

met en place. Le temps de montée, c'est-à-dire la durée pendant laquelle un point a une vitesse de glissement non-nulle, est lui aussi constant. Bien que la fonction source associée trapézoïdale reproduise le spectre "ω-squared", ce modèle présente des limites car le séisme nuclée instantanément sur la largeur de la faille, et le passage d'une quantité de glissement finie à nulle sur les bords implique une concentration de contraintes en inadéquation avec une vision physique de la rupture.

Un modèle plus adapté à la physique de la rupture nécessite donc un glissement nul aux bords de la faille, ainsi qu'une nucléation qui se fait à partir d'un point. Le modèle de crack circulaire auto-similaire développé par Kostrov (1964) répond à ces attentes et est dès lors une référence pour l'analyse de la source sismique. La rupture se propage du centre d'une faille circulaire avec une vitesse de rupture constante V_r. Le glissement derrière le front de rupture n'est pas constant comme dans le modèle d'Haskell mais est gouverné par la chute de contrainte $\Delta\sigma$ et s'écrit :

$$u(r,t) = \begin{cases} \dfrac{\Delta\sigma}{\mu}\sqrt{(V_r t)^2 - r^2} & \text{pour } r < V_r t, \\ 0 & \text{pour } r > V_r t, \end{cases} \tag{1.8}$$

avec μ la rigidité du milieu, $V_r t$ le rayon du crack au temps t, et r la distance d'un point à l'hypocentre. Le glissement à un temps donné est nul sur le front de rupture et augmente derrière celui-ci pour atteindre une valeur maximum au centre du crack comme le montre la Figure 1.6. Une particularité importante du crack circulaire vient de la forme du glissement qui induit une chute de contrainte $\Delta\sigma$ constante derrière le front de rupture quel que soit t. Cette propriété, associée à une vitesse de rupture constante, fait de la

croissance d'un crack circulaire un processus auto-similaire. L'étude de Sato and Hirasawa (1973) complète ce modèle en y ajoutant une phase d'arrêt de la rupture, ce qui permet de mieux reproduire le spectre du rayonnement en champ lointain grâce à la présence d'un contenu haute fréquence du à l'arrêt du séisme. Cependant, la solution du glissement 1.8 puis celle de la vitesse de glissement 1.9 employées tout au long de ce manuscrit sont issues de l'étude de Kostrov (1964) puisque l'étude du développement de la rupture ne nécessite pas la modélisation de sa phase d'arrêt. La forme analytique du glissement dans l'équation 1.8 permet de simplement déterminer l'expression de la fonction source. En effet, d'après la définition 1.6, la dérivée temporelle du glissement est nécessaire pour calculer l'évolution du taux de moment, et s'écrit :

$$\dot{u}(r,t) = \begin{cases} \dfrac{\Delta\sigma}{\mu} V_r^2 \dfrac{t}{\sqrt{(V_r t)^2 - r^2}} & \text{pour } r < V_r t, \\ 0 & \text{pour } r > V_r t. \end{cases} \tag{1.9}$$

La vitesse de glissement avec sa dépendance temporelle et spatiale est représentée Figure 1.7. Pour un t donné, cette fonction atteint une valeur infinie sur le front de rupture, et décroît derrière le front pour atteindre une valeur constante à l'hypocentre ($r = 0$). Pour un r donné, la vitesse de glissement est nulle avant le passage du front et infinie lorsqu'il l'atteint, et décroît après son passage pour tendre vers la même valeur constante qu'à l'hypocentre. Le temps de montée à l'hypocentre est alors le temps de rupture totale. La singularité au front de rupture est cependant absente dans un modèle où une zone de cohésion au niveau du front permet à la contrainte de varier sur une distance non nulle, ce qui est discuté plus en détail dans le Chapitre 2. En insérant la vitesse de glissement dans l'équation 1.6, l'expression de la fonction source d'un crack circulaire auto-similaire devient :

$$\dot{M}(t) = \mu \frac{\Delta\sigma}{\mu} V_r^2 \int_0^{2\pi} \int_0^{V_r t} \frac{t}{\sqrt{(V_r t)^2 - r^2}} r \, \mathrm{d}r\mathrm{d}\theta \tag{1.10}$$

$$= 2\pi \Delta\sigma V_r^3 t^2. \tag{1.11}$$

Le terme d'auto-similarité employé à l'égard des séismes renvoie donc à l'évolution caractéristique en t^2 du taux de moment lorsque la rupture se développe. De manière théorique, le modèle de crack génère des fonctions source dont seule la durée du développement est liée à la taille finale de la rupture, car les courbes de taux de moment de petits et grands séismes se confondent et se développent en t^2. Cette évolution est également retrouvée dans les modèles de crack elliptiques (Burridge and Willis, 1969; Dong and Papageorgiou, 2003), où la seule nuance avec le crack circulaire vient de l'expansion surfacique plus limitée introduisant un coefficient inférieur à 1 devant l'équation 1.11.

Le modèle auto-similaire de pulse (Heaton, 1990; Nielsen and Madariaga, 2003), qui diffère du modèle de crack car le temps de montée à l'hypocentre est plus court que la durée de la rupture, génère également une fonction source avec une évolution en t^2 du taux de moment

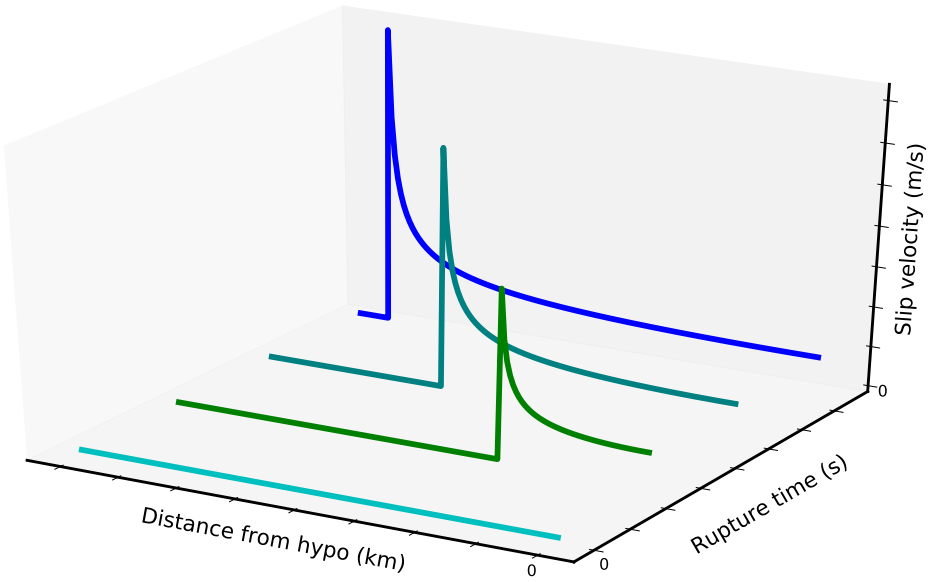

Figure 1.7 – Vitesse de glissement du modèle de crack circulaire auto-similaire dépendant du temps et de la distance. À chaque temps, la vitesse de glissement est maximale au front de rupture (la singularité est ici remplacée par une valeur finie) et atteint un plateau en se rapprochant de l'hypocentre.

à partir d'une fonction vitesse de glissement détaillée dans Ruff (1999). Ce modèle, observé aussi bien en laboratoire (Lykotrafitis et al., 2006; Rubino et al., 2017), sur les séismes réels (Beroza and Mikumo, 1996; Melgar and Hayes, 2017) et dans les simulations dynamiques (Zheng and Rice, 1998; Rubin and Ampuero, 2005), constitue avec le modèle de crack les deux processus décrivant quantitativement la dynamique de la propagation de la rupture.

1.3.4 Modèles en cascade et implications pour le développement de la rupture

La question du déterminisme de la rupture sismique et des modèles associés a été abordée bien avant que des catalogues globaux tels que la base de données SCARDEC puissent offrir une nouvelle caractérisation du processus de source. Les premières études proposant un modèle de l'initiation de la rupture des petits et grands séismes à partir de l'observation de signaux sismologiques analysent le début des fonctions source dans la région de Northridge (Ellsworth and Beroza, 1995; Beroza and Ellsworth, 1996; Ellsworth and Beroza, 1998). Une phase de nucléation dont la durée est proportionnelle au moment final est détectée avant que le taux de moment n'évolue de manière quadratique. Même si ce signal dépendant de la taille finale a été remis en cause en raison d'effets de filtrage (Scherbaum and Bouin, 1997), ces auteurs proposent un modèle de déclenchement des séismes en "cascade" qui est couramment utilisé pour expliquer les observations. Le modèle en cascade suppose qu'un grand séisme est la conséquence de déclenchements d'événements de plus en plus grands. Petits et grands séismes partagent donc la même croissance jusqu'à ce que le premier s'arrête, alors que le second continue son développement. La taille finale du séisme est contrôlée par la dimension du dernier événement déclenché. Ce type de modèle implique donc que l'information sur le moment final ne peut être déduite dès la phase d'initiation.

Des observations contraires au modèle en cascade suggèrent cependant un certain degré de déterminisme dans les premiers instants du processus de rupture. Ishihara et al. (1992) étudient les fonctions source d'une séquence de séismes au large du Japon et observent que la pente de la croissance des STFs est correlée avec la taille finale du séisme, ce qui implique une différence de comportement précoce des séismes en fonction de leur magnitude. Les études appliquées au système de détection précoce des séismes ont également proposé qu'une information sur la magnitude était contenue dans les premières secondes du signal de l'onde P. Zollo et al. (2006) et Colombelli et al. (2014) analysent le déplacement des ondes P après un filtrage passe-bas pour plusieurs dizaines de séismes à des distances atteignant 500 km. Leurs observations indiquent que l'évolution temporelle de l'amplitude maximale du déplacement est correlée avec la magnitude des séismes. En augmentant progressivement la fenêtre temporelle pour déterminer le pic d'amplitude, les auteurs remarquent une augmentation rapide de l'amplitude maximale pour les petits événements, alors que celle-ci est plus lente pour les grands séismes. Leurs travaux rejoignent ceux de Allen and Kanamori (2003) et Olson and Allen (2005) qui analysent eux aussi les premières secondes du signal de l'onde P mais dans le domaine fréquentiel. Ils sélectionnent plusieurs dizaines de series temporelles de vitesse à moins de 100 km pour des séismes mondiaux et calculent la période dominante durant les quatre premières secondes du signal. La période dominante augmente avec la magnitude des séismes, et implique donc un potentiel comportement déterministique des séismes. Par conséquent, ces études reconsidèrent le modèle en cascade, en faisant intervenir des patchs sur la faille plus enclins à générer de grands séismes. Cette hypothèse fait intervenir des considérations dynamiques, et suggère que les ruptures qui s'initient en rompant des grands patchs, où l'énergie disponible pour la propagation de la rupture est plus grande, ont statistiquement plus de chance de générer de grands séismes.

Cependant, d'autres études confirment la validité du modèle en casade en s'appuyant sur l'observation de signaux bruts sur une large gamme de magnitude qui suggèrent un comportement universel des séismes lors de leur croissance (Meier et al., 2016; Okuda and Ide, 2018; Ide, 2019). En particulier, Okuda and Ide (2018) et Ide (2019) analysent la sismicité de la zone de subduction de Tohoku-Hokkaido et bénéficient de la densité du réseau pour comparer des paires de séismes de magnitudes différentes dont les hypocentres sont localisés au même endroit sur l'interface de subduction. À une même station, deux séismes initiés au même endroit peuvent donc être simplement comparés en superposant leurs formes d'onde sans aucun traitement. Pour plusieurs centaines de paires de séismes jusqu'à 0.2 s, le coefficient de corrélation moyen des stations où la paire de séismes a été détectée est très élevé, indiquant que les formes d'onde sont très similaires. Ces observations sont par conséquent expliquées par le modèle en cascade et interprétées conceptuellement par la Figure 1.8. Une structure hiérarchique se dessine sur la faille où des petits patchs sont inclus dans des patchs de plus grandes dimensions. La rupture s'initie systématiquement dans le plus petit patch (couleur gris clair), et se propage ensuite dans les patchs de dimensions supérieures (gris foncé et noir) en fonction de leur distribution. Dans ce cas, l'augmentation de l'énergie disponible pour la propagation de la rupture est la conséquence de la rupture successive des patchs, ce qui signifie qu'un grand séisme ne peut se déclencher qu'à partir d'une taille de patch caractéristique. Cependant, même si cette structure

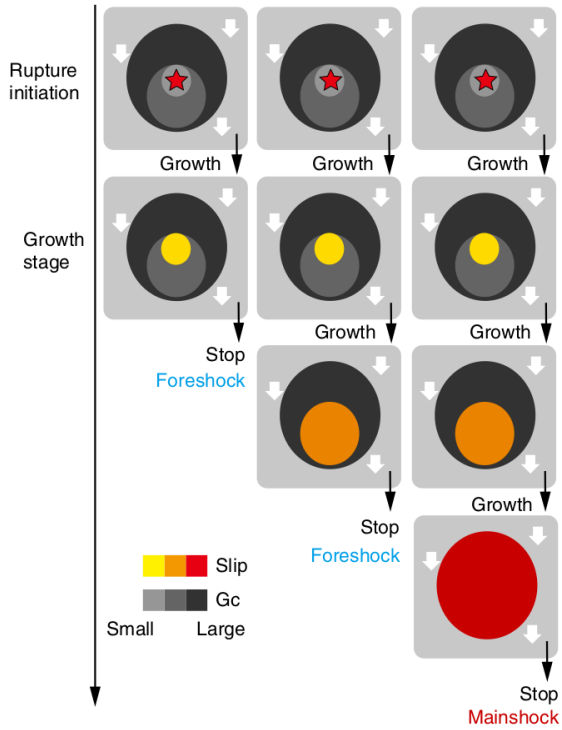

Figure 1.8 – Représentation conceptuelle du modèle en cascade du déclenchement des séismes. Des patchs de tailles différentes se distribuent sur la faille. La rupture s'initie sur un petit patch pour croître dans des patchs de tailles supérieures. Cette structure hierarchique implique que la taille finale du séisme est contrôlée par la dimension du dernier patch rompu. Graphique issu de Okuda and Ide (2018).

hiérarchique implique que la taille finale d'un séisme ne peut être déterminée que lorsque le plus grand patch a été rompu, la localisation des patchs paraît être une caractéristique qui ne dépend pas du temps. Le déclenchement d'un petit ou d'un grand séisme provient alors de l'évolution des conditions physiques sur la faille.

Tant du point de vue de l'observation que des modèles, la similarité des séismes ou la présence d'un signal déterministe reste donc une question ouverte. L'analyse de la croissance des fonctions source est par conséquent un nouvel angle pour participer à la meilleure compréhension du développement des séismes. Le catalogue SCARDEC a le potentiel d'explorer cette question, avec des analyses observationnelles complémentaires à celles évoquées en Section 1.3.2. Ces observations peuvent être directement comparées aux modèles cinématiques proposés en Section 1.3.3, afin d'estimer le comportement des paramètres cinématiques permettant un accord avec les données. Enfin, comme évoqué ci-dessus, une structure hiérarchique complexe associée à des conditions physiques hétérogènes sur les failles fait appel à des considérations dynamiques de la propagation de la rupture, qui doivent être prises en compte pour une complète description du développement des séismes.

Chapitre 2

How does seismic rupture accelerate? Observational insights from earthquake source time functions

Ce chapitre s'intéresse à l'analyse du développement des séismes avec comme observable les fonctions source optimales du catalogue SCARDEC. La variabilité du processus de rupture résulte en des formes complexes de STFs, incluant par conséquent des croissances très diverses. Le but principal de cette étude est d'observer l'augmentation transitoire du taux de moment vers le pic de la fonction source, qui correspond à la période où la majorité du moment sismique est relâchée. Le large intervalle de magnitude du catalogue présente l'avantage de statistiquement mettre en lumière les similitudes et différences des séismes modérés à forts de cette phase de développement. Les 2221 STFs de séismes superficiels et non décrochants sont analysées de manière à révéler un comportement dépendant ou non de la magnitude finale et de quantifier plus précisément l'évolution temporelle du taux de moment lors de cette phase. Les caractéristiques du développement de la rupture extraites par notre analyse permettent une comparaison avec les modèles cinématiques de propagation de la rupture ainsi que la création d'un catalogue de fonctions source simplifiées qui reproduit les propriétés globales et transitoires des séismes.

Le contenu de ce chapitre est un article et des matériels supplémentaires publiés dans le journal Journal of Geophysical Research: Solid Earth sous le titre *How does seismic rupture accelerate? Observational insights from earthquake Source Time Functions* en collaboration avec Pierre Dublanchet.

Abstract Observation of the seismic process for a large earthquake population is of key interest to detect potential magnitude-dependent behaviors, and more generally to quantify how seismic rupture develops. In contrast with studies focusing on the first radiated waves, we here propose to characterize the growing phase leading to the main seismic moment release episode(s), that we refer to as the development phase. Our analysis uses the 2221 teleseismic source time functions (STFs) of shallow dip-slip earthquakes provided by the global SCARDEC database, and consists in measuring the moment acceleration during the development phase at prescribed moment rates. This approach is therefore insensitive to hypocentral time uncertainties, and aims at quantifying how seismic ruptures accelerate, independently of when they accelerate. Our results first show that rupture acceleration does not exhibit any magnitude dependent signal emerging above the intrinsic measurements variability. We thus use the full STF catalog to characterize the moment rate $\dot{M}_d$ of the development phase, and show that, on average, $\dot{M}_d(t) \propto t^{n_d}$ with n_d equal to 2.7. This time evolution therefore does not follow the steady t^2 growth expected for classical circular crack models, which indicates that stress drop and/or rupture velocity transiently vary during the development phase. We finally illustrate with a synthetic STF catalog that, due to initial rupture variability, approaches based on hypocentral time are not expected to fully characterize the behavior of the development phase.

2.1 Introduction

The mechanisms governing the seismic rupture expansion and giving rise to earthquakes of very different magnitudes remain debated. From an observational point of view, past studies most often focused on the first seismic signals radiated by the earthquake rupture, with the goal to provide useful information for early warning. Several studies (Beroza and Ellsworth, 1996; Olson and Allen, 2005; Colombelli et al., 2014) argued for the existence of

a magnitude-dependent initial signal, connecting the early phases of the rupture process with its final magnitude. The existence of such a signal could be explained, for example, if an earthquake is more likely to become a large one if its initial phase occurs in rupture-prone areas. Large earthquakes would then start differently from small ones, at least in a statistically predictable way. Conversely, many rupture onsets have been observed without detecting any clues related to the final earthquake magnitude; seismic rupture is then interpreted as a "self-similar" process, meaning that large earthquakes are only upscaled versions of small magnitude events, without having their own characteristics (Aki, 1967). As a result of this concept, studies showed for instance that stress drop and rupture velocity are independent of the magnitude, or that the seismic moment is proportional to the cube of the earthquake duration (Kanamori and Anderson, 1975; Allmann and Shearer, 2009). The self-similar behavior can be reproduced by a cascade model, in which the rupture starts from a very small patch, which size is undetectable by seismological investigation. Then rupture grows in a self-similar way, implying that the final magnitude is controlled by the earthquake duration. Such behavior has been for example observed by Uchide and Ide (2010) in their analysis of earthquakes in the Parkfield area.

Observations of the earthquake process however reveal that real ruptures frequently depart from such simple models, and that the peak moment rate can be reached after a non-monotonical or delayed process. Studying how rupture behaves when entering into its most active phase (that we hereafter refer to as the "development phase") therefore requires an analysis of the whole process and not only its beginning. To do so, we propose to make use of the large catalog of moment rate functions (or Source Time Functions, STFs) provided by the SCARDEC database (Vallée and Douet, 2016). SCARDEC database has first been used to extract global source properties, such as source-averaged stress/strain drop or rupture velocity (Vallée, 2013; Courboulex et al., 2016; Chounet et al., 2017; Chounet and Vallée, 2018), and is now more and more exploited to characterize the transient parts of STFs (Meier et al., 2017; Melgar and Hayes, 2017, 2019). With a similar objective as the studies based on the early stages of the rupture, we will first explore if the moment acceleration in the development phase correlates with the magnitude of the event. We will then characterize the temporal moment evolution of this specific phase, in order to provide observational constraints on rupture propagation models. We finally further illustrate, with a realistic synthetic STF catalog, why the characteristics of the development phase are difficult to retrieve from the study of the early rupture stages.

2.2 Moment acceleration in the development phase

2.2.1 SCARDEC STF database and earthquake development phase

Exhaustive catalogs of STFs (describing the time evolution of the moment rate $\dot{M}$) can be built with two distinct methods which both use teleseismic data from the FDSN (Federation of Digital Seismograph Network). The first approach determines a finite fault model of the seismic source (in general for earthquakes with $M_w > 7$, (Ye et al., 2016; Hayes, 2017)) from which the absolute STF is computed. On the other hand, in the SCARDEC method (Vallée et al., 2011), seismic moment, focal mechanism, source depth and STFs are more directly obtained through a deconvolution process (see also Tanioka and Ruff

(1997)). At each station and for each phase (P or S), apparent source time functions (ASTFs) are extracted, whose shapes differ due to space-time source effects (Chounet et al., 2017). In order to take into account both this expected distorsion and possible outliers (due to nodal radiation, incorrect instrument response, etc.), SCARDEC database (Vallée and Douet, 2016) provides two representative STFs for each event. A mean STF is first obtained by correlating in time all P-wave ASTFs (less sensitive to space-time source effects than S-wave ASTFs), removing ASTFs far from the beam, and averaging the remaining ASTFs. The optimal STF is then chosen as the P-wave ASTF which is the closest to the mean STF. Such an optimal STF is unlikely to be among the most distorted ASTFs, and its shape is not affected by the smoothing present in the mean STF. The optimal STFs are therefore considered in this study. Deep ($> 70\,$km) and pure strike-slip events are removed from the database due to their specific behavior (Houston, 2001) and the difficulty to robustly extract their P-wave STFs, respectively. The catalog is finally composed of 2221 earthquake STFs (from 1992 to 2017), whose magnitudes range from M_w 5.5 to M_w 9.1 (2011 Tohoku earthquake) and durations from 2 s to 120 s.

We aim here at isolating the development phase, i.e. the time period where STFs grow toward their peak moment rate F_m (that they reach at time T_m). Taking into account that the moment rate always flattens before reaching F_m, we do not consider the highest STF values to be part of the development phase: in the following, we only select the parts of the STF which are before T_m, and whose values are below $0.7\,F_m$. At low moment rate values, we would ideally track the development phase from its very beginning. However, SCARDEC STFs are retrieved by deconvolving the full P-waveform (under physical constraints such as STF positivity), and the STF fidelity at values much lower than F_m is therefore expected to be relatively low. As a result, we do not analyze here the development phase for STF values lower than $0.07\,F_m$. The value of these two selected lower and upper limits are not critical and other choices (e.g. starting at $0.05\,F_m$ and stopping at $0.5\,F_m$) do not affect significantly the following results (see Figure 2.20 in Supplementary Materials).

In order to isolate the development phases in all cases, we consider the two following possible configurations of STFs. The simplest and most common case (representing 62% of the STF catalog) is illustrated by the STFs shown in Figure 2.1a) and 2.1b). Here, even when the STF does not grow monotonically toward its peak, there is a unique monotonic domain connecting the values between $0.07\,F_m$ and $0.7\,F_m$. This specific section of the STFs, shown in red in Figure 2.1, is selected as the development phase. STFs with complex shapes however do not have such a unique monotonic domain (Figure 2.1c)). In this case, we work on the time interval defined by two times T_0 and T_1: T_0 is the latest time preceding T_m when the STF is as low as $0.07\,F_m$ and T_1 is the latest time preceding T_m when the STF is not above $0.7\,F_m$. In the $[T_0 T_1]$ interval, there may be several local maxima F_p ($p = 1, P$), around which rupture is not considered to be in a development phase. The development phase is then selected as the combination of monotonic phases preceding each F_p, from the time when they exceed the largest value of all the preceding local maxima (or from T_0 if $p = 1$) to the time where they reach $0.7\,F_p$. As a consequence, if one of the local peak values before F_p is larger than $0.7\,F_p$, the monotonic phase preceding F_p is not considered. We finally select the monotonic phase up to T_1 (from the time where the

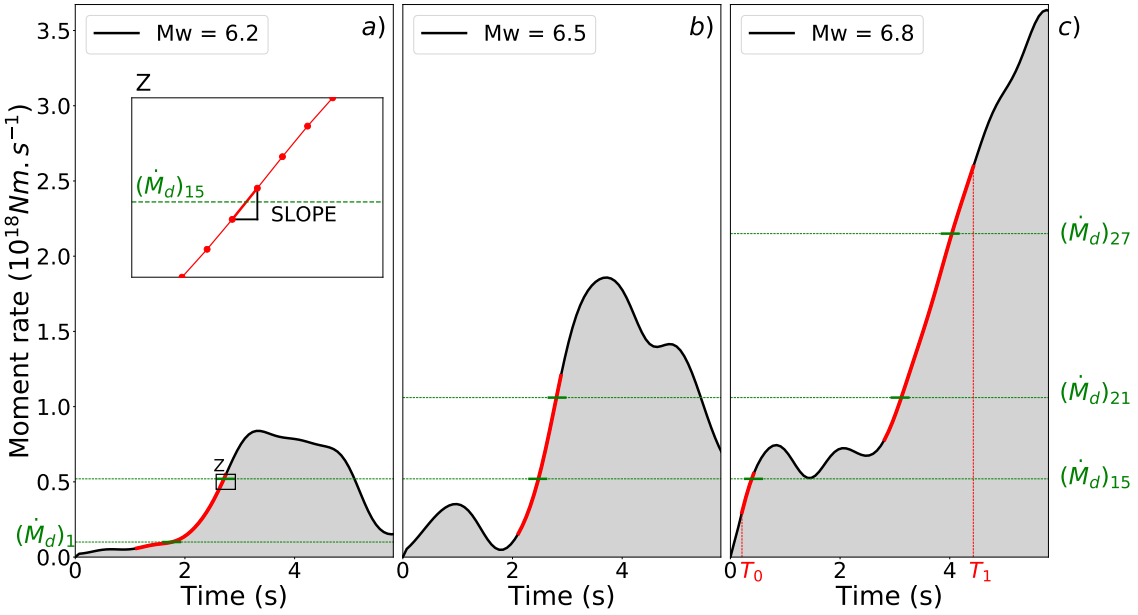

Figure 2.1 – Examples of extraction of the development phase (in red) for representative STF shapes. In a) and b), STFs have a monotonic section connecting the values between $0.07\,F_m$ and $0.7\,F_m$. c) is an example of STF with complex shape in which development phase is extracted in the $[T_0 T_1]$ time interval (see Section 2.2.1). These three illustrative events have different magnitudes and their development phases start at different times. Moment acceleration is computed at the time where the development phase crosses the prescribed moment rates $(\dot{M}_d)_i$, if this intersection exists. Four examples of $(\dot{M}_d)_i$ values (for $i = 1, 15, 21$ and 27) are shown in green. The sampling rate is equal to $0.07\,$s. Note that the approximate reference time shown in the bottom of each STF is not used in this approach.

STF reaches F_p, or from T_0 if $P = 0$). In these complex cases, the development phase is therefore the combination of at most $(P + 1)$ growing sections of the STFs.

According to the aforementioned definitions, the development phase may be delayed compared to hypocentral time, meaning that we do not intend to characterize the earliest signals emitted by the seismic rupture. This approach therefore differs from studies specifically analyzing the latter signals in order to explore the concept of earthquake determinism since the earthquake initiation (Meier et al., 2017; Melgar and Hayes, 2017, 2019).

2.2.2 Seismic moment acceleration within the development phase

Once the development phase is extracted for each STF, we aim at characterizing it without using hypocentral time information, in order to quantify how rupture develops independently of when rupture develops. Formally, we look for the moment evolution of the development phase M_d where $M_d(t) = M(t + T_d)$, T_d being the unknown time at which the development phase starts. A way to characterize M_d is to consider a discrete sampling of prescribed moment rates $(\dot{M}_d)_i$, and to compute the seismic moment acceleration (STF slope) each time that the development phase crosses $(\dot{M}_d)_i$. To do so, we consider 40 different values of $(\dot{M}_d)_i$ $(i = 1, 40)$, from 10^{17} to $10^{19}\,\mathrm{Nm.s^{-1}}$, in order to sample the development phase of most earthquakes. Outside of this range, moment rates are either mostly below $0.07\,F_m$ or above $0.7\,F_m$, and cross only a few development phases. As further documented later, the maximum considered moment rate ($10^{19}\,\mathrm{Nm.s^{-1}}$) is typically reached 6s after the beginning of the development phase for monotonically growing STFs.

In terms of magnitude, the smallest earthquakes of the SCARDEC database ($M_w = 5.5$) can be analyzed by this sampling, and only the largest earthquakes ($M_w > 8.4$) are systematically excluded. Figure 2.1 illustrates the method for three STFs and four moment rates $(\dot{M}_d)_i$ (green dashed lines). Low values of moment rate are mostly sampled by small events (as they will lie below $0.07\,F_m$ for large ones) and high values of moment rate are mostly sampled by large events (as they will lie above $0.7\,F_m$ for small ones). However, this general behavior does not prevent us from sampling a large range of magnitudes at a given moment rate. As shown in the example of Figure 2.1, the moment acceleration of the development phase at the $(\dot{M}_d)_{15}$ level can be computed from $M_w = 6.2$ to $M_w = 6.8$.

2.2.3 Variability and magnitude-independent behavior

Such slope measurements can be first used to detect a potential magnitude-dependent behavior, in which the slope measured when the development phase crosses prescribed moment rates would be for instance steeper for larger events. For the N_i development phases crossing $(\dot{M}_d)_i$, we compute the slope values $(\ddot{M}_d)_{ij} (j = 1, N_i)$ as a function of M_w, to observe whether or not a magnitude-dependent signal appears. Figure 2.2 shows an example of the 892 $(\ddot{M}_d)_{15j}$ values for $(\dot{M}_d)_{15} = 5.2 \times 10^{17}\,\mathrm{Nm.s^{-1}}$. The following analysis of $\ddot{M}_d$ values with respect to M_w has to be done with care, because a given $(\dot{M}_d)_i$ value does not sample equally well all magnitude ranges (Section 2.2.2), as also illustrated in Figure 2.2: the histogram shows the ratio of sampled STFs in each M_w bin, and this value decreases both towards low M_w (only impulsive STFs reach $(\dot{M}_d)_i$) and towards high M_w (only STFs with relatively low F_m have $(\dot{M}_d)_i$ in their development phase). As a consequence, $(\ddot{M}_d)_{ij}$ values are expected to be biased toward high values for small magnitude events, as confirmed by Figure 2.2. We thus focus on the M_w domain where most of the development phases cross the chosen $(\dot{M}_d)_i$ (for example between $M_w = 6.3$ and $M_w = 7.0$ in the case shown in Figure 2.2).

Figure 2.2 does not exhibit any clear dependency between $(\ddot{M}_d)_{15j}$ and M_w, and the same behavior is observed for all the other prescribed $(\dot{M}_d)_i$ (Figures 2.10 to 2.19 of the Supplementary Materials). This shows that if a magnitude-dependent signal exists, it is fully dominated by the intrinsic variability of the development phase. This means that when an earthquake develops and reaches a given moment rate $(\dot{M}_d)_i$, moment acceleration cannot be used as an indicator of the final magnitude (only a lower bound can of course be estimated based on the seismic moment already released). This observation may appear different from the recent results of Melgar and Hayes (2019), who extracted a magnitude-dependent signal from STF accelerations (using also the SCARDEC catalog). Their approach is however fundamentally different as they simply computed an averaged moment acceleration by dividing the moment rate from the rupture time, at several prescribed rupture times τ ($\tau = 2, 5, 10, 20\,\mathrm{s}$). Using this definition, they observe an increase of the moment acceleration with the final event magnitude, clearly appearing for τ equal to 10 s and 20 s. In such an analysis, there is however no guarantee that the earthquake at τ is still in its development phase, particularly when τ is a significant fraction of the global earthquake duration. As an example, 20 s is a significant fraction of the global duration of an $M_w = 8$ earthquake (whose average global duration is about 60 s, e.g. Vallée (2013)). It is therefore not uncommon, at 20 s, that $M_w = 8$ earthquakes STFs flatten as they

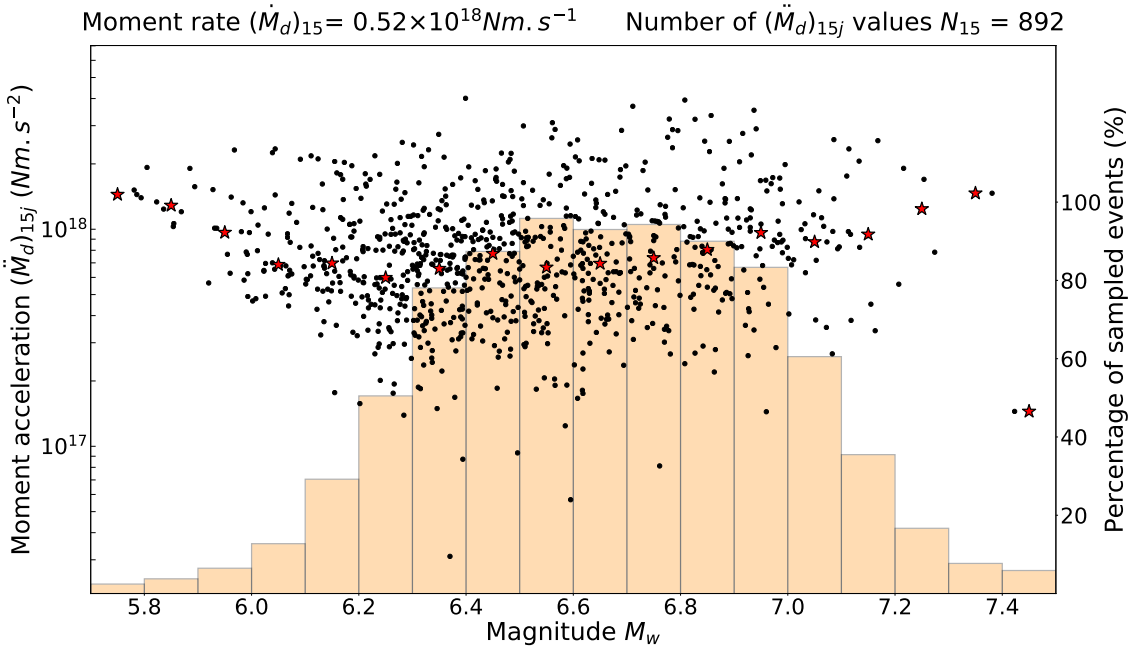

Figure 2.2 – Moment acceleration as a function of magnitude for the prescribed moment rate of 5.2×10^{17} Nm.s^{-1} ($(\dot{M}_d)_{15}$). The filled histogram represents the ratio (in %, see scale to the right) of sampled events in each M_w bin. Comparisons between moment acceleration and magnitude can be safely done when almost all the STFs of a given magnitude are sampled ($> 80\%$), here between $M_w = 6.3$ and $M_w = 7.0$. Red stars are median values for each magnitude bin. Similar figures for all the prescribed moment rates are provided in Figures 2.10 to 2.19.

approach their peak moment rate (and some of them may have already passed it). As a result, on average, acceleration can be understood to be statistically lower than for a $M_w = 9$ earthquake, for which the peak always occurs far after 20 s. Melgar and Hayes (2019) results likely reflect the magnitude-dependent shape of the earthquake STFs, at a macroscopic scale, while we are here specifically studying their fast growing parts.

2.3 Time evolution of the development phase

2.3.1 Observational evidence of a power law between $\ddot{M}$ and $\dot{M}$

The magnitude independency derived in the previous section justifies the combined use of $(\ddot{M}_d)_{ij}$ for all values of i, in order to determine a generic behavior of the rupture development. Figure 2.3 represents (in log-log scale) all the moment acceleration values as a function of the moment rate values (yellow dots). Direct observation in Figure 2.3 reveals that $\ddot{M}_d$ grows with $\dot{M}_d$, which first implies that the time evolution of the moment rate in the development phase cannot be linear. In order to quantify the general behavior, we try to fit our observations with a power law of the type $\ddot{M}_d = \beta \dot{M}_d^m$. Using the method detailed in Section 2.7.1 of the Supplementary Materials, a linear fit (in log-log scale) leads to values of $m = 0.63 \pm 0.015$ and $\log(\beta) = 6.7 \pm 0.28$ at the 90% confidence interval, with a correlation coefficient of 0.8 (Figure 2.3).

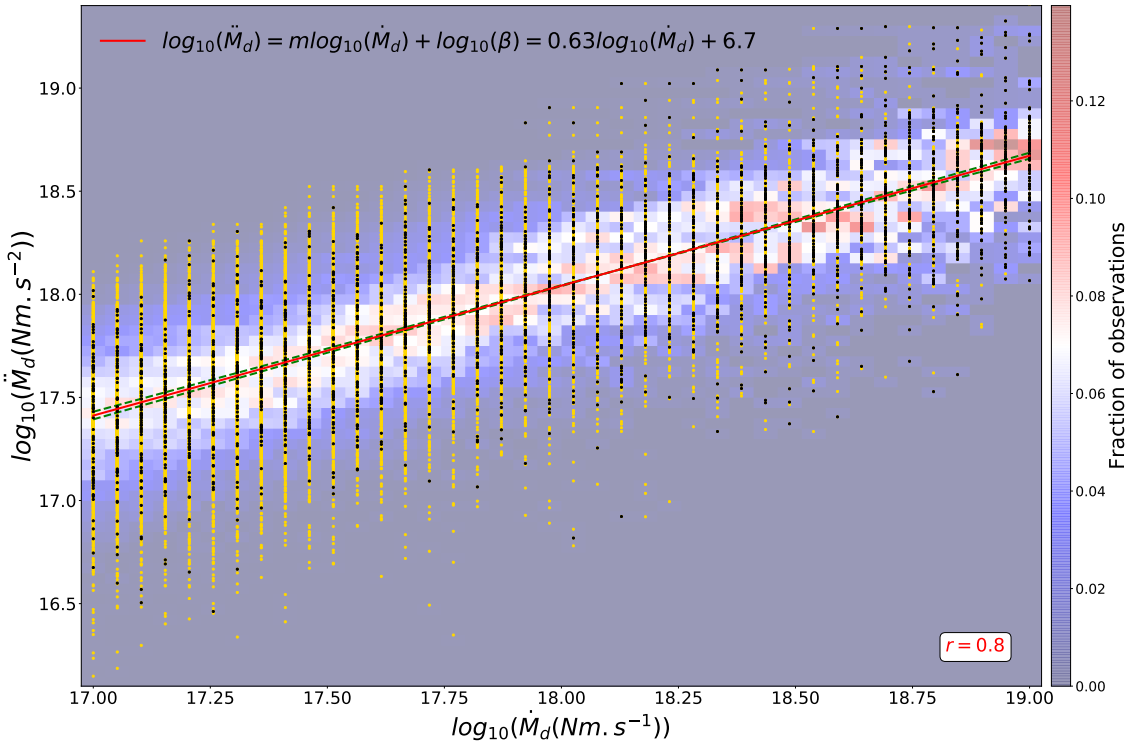

Figure 2.3 – Moment acceleration $\ddot{M}_d$ as a function of moment rate $\dot{M}_d$ (log-log scale). Each yellow dot corresponds to an individual $(\ddot{M}_d)_{ij}$ value, and black dots are 75 randomly selected values for each $(\dot{M}_d)_i$ used to compute the linear fit (see Section 2.7.1 of the Supplementary Materials). Red line is the best linear fit explaining the data, and its equation and correlation coefficient r are given in the figure. Green dashed lines are fits with extremal values of m and $\log(\beta)$ at the 90% confidence interval. Background color represents the number of $(\ddot{M}_d)_{ij}$ values normalized by N_i for each $(\dot{M}_d)_i$. This fraction of observations is computed between $\log(10^{15})$ Nm.s^{-2} and $\log(10^{20})$ Nm.s^{-2} with 100 bins.

2.3.2 Power-law time exponent of the development phase

Analytical models of rupture dynamics (Kostrov, 1964; Dahlen, 1974; Madariaga, 1976; Nielsen and Madariaga, 2003) have shown that self-similar circular growth with constant stress drop $\Delta\sigma$ and rupture velocity V_r leads to a moment rate function of the form $\dot{M}(t) = \alpha t^n$ with $n = 2$. In this model, the local slip u and slip rate $\dot{u}$ have the shape, in the general case of a time-varying rupture velocity $v_r(t)$:

$$u(r,t) = \frac{\Delta\sigma}{\mu}\sqrt{a^2(t) - r^2} \tag{2.1}$$

$$\dot{u}(r,t) = \frac{\Delta\sigma}{\mu} v_r(t) \frac{a(t)}{\sqrt{a(t)^2 - r^2}} \tag{2.2}$$

where μ is the rigidity and $a(t) = \int_0^t v_r(u)du$ is the radius of the rupture at time t. The moment time evolution therefore follows the law:

$$\begin{aligned} M(t) &= 2\pi\mu \int_0^{a(t)} u(r,t) r \, \mathrm{d}r \qquad (2.3)\\ &= \frac{2\pi}{3}\Delta\sigma \Big[(a^2(t) - r^2)^{3/2}\Big]_{a(t)}^{0} \\ &= \frac{2\pi}{3}\Delta\sigma a^3(t). \qquad (2.4) \end{aligned}$$

And if $v_r(t) = V_r$ is constant, $a(t) = V_r t$ and we have:

$$\begin{aligned} M(t) &= \frac{2\pi}{3}\Delta\sigma V_r^3 t^3 \\ \dot{M}(t) &= 2\pi\Delta\sigma V_r^3 t^2. \end{aligned} \tag{2.5}$$

This quadratic dependency with time is also found from the seismic moment M_0, by using that $\Delta\sigma = c\mu\frac{\Delta U}{L}$, $M_0 = \mu\Delta U S$ (where c is a constant, ΔU the average displacement, L the characteristic dimension of the fault and S its surface), and considering a seismic rupture growing in a bi-dimensional way with constant rupture velocity. At the time of the end of the rupture, we have $M_0 \propto \Delta\sigma V_r^3 T^3$ (with T being the final rupture duration), but due to self-similarity, this relation also holds for the moment function M at any earlier time t:

$$M(t) \;\propto\; \Delta\sigma V_r^3 t^3 \quad \text{leading to} \quad \dot{M}(t) \;\propto\; \Delta\sigma V_r^3 t^2. \tag{2.6}$$

The previously obtained $\ddot{M}_d$ values do not directly constrain the time evolution of the development phase, because we only know them as a function of $\dot{M}_d$ ($\ddot{M}_d = \beta\dot{M}_d^m$, with $\log(\beta)$ and m found equal to 6.7 ± 0.28 and 0.63 ± 0.015 at the 90% confidence interval, respectively). However, reorganizing this power law equation, and integrating over time leads to:

$$\int_0^t \frac{\ddot{M}_d(u)}{(\dot{M}_d(u))^m}\,\mathrm{d}u \;=\; \int_0^t \beta\,\mathrm{d}u \quad (\forall t > 0,\, \dot{M}_d(t) > 0), \tag{2.7}$$

with t being a time inside the development phase. The lower bound of integration in (2.7)

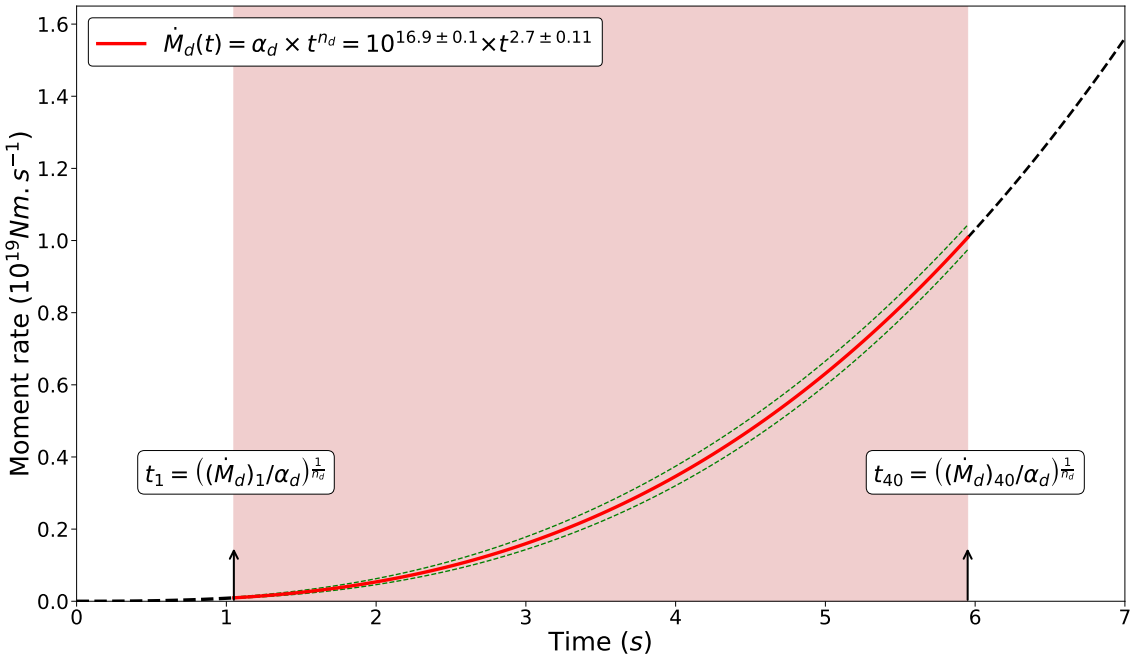

Figure 2.4 – Time evolution of the development phase extracted from the observed power law between $\ddot{M}_d$ and $\dot{M}_d$. t_1 and t_{40} are the times corresponding to the extremal moment rate values ($(\dot{M}_d)_1 = 10^{17}$Nm/s and $(\dot{M}_d)_{40} = 10^{19}$ Nm.s^{-1}) at which the moment accelerations are computed. This time window between t_1 and t_{40}, where the time exponent of the moment rate $n_d = 2.7$ directly comes from the observations, is highlighted by the red shaded area. Green dashed curves are the extremal curves inferred from α_d and n_d uncertainties.

assumes that the observed power law between $\ddot{M}$ and $\dot{M}$ holds from the beginning of the development phase, which appears reasonable because no deviation appears at low moment rates in Figure 2.3. As m is observationally strictly smaller than 1 (even the extreme m values shown in Figure 2.8(a) of the Supplementary Materials are strictly smaller than 1), equation 2.7 has the solution:

$$\frac{\left(\dot{M}_d(t)\right)^{1-m}}{1-m} \;=\; \beta t \tag{2.8}$$

where we use the physical constraint $\dot{M}_d(0) = 0$. The moment rate function can then be rewritten as a function of time:

$$\dot{M}_d(t) \;=\; (\beta(1-m))^{\frac{1}{1-m}} \times t^{\frac{1}{1-m}} \tag{2.9}$$

In the following, we now define $\alpha_d = (\beta(1-m))^{\frac{1}{1-m}}$ and $n_d = \frac{1}{1-m}$. Using the values of m and β, the numerical expression for the time evolution of the development phase is:

$$\dot{M}_d(t) \;=\; \alpha_d \times t^{n_d} \;=\; 10^{16.9 \pm 0.1} \times t^{2.7 \pm 0.11} \tag{2.10}$$

where uncertainties for n_d and α_d correspond to the 90% confidence intervals estimated in Figure 2.8(b) of the Supplementary Materials.

In Figure 2.4, we show this temporal evolution of $\dot{M}_d$ and indicate the time window between $\sim$1 s and $\sim$6 s (corresponding to $\dot{M}_d$ values between 10^{17} and 10^{19} Nm.s^{-1}), where the

shape of $\dot{M}_d$ is directly constrained by the observations. As n_d is robustly larger than 2, equation 2.10 indicates that the rupture process during the development phase grows with time with a higher exponent than what the classical self-similar equations 2.5 and 2.6 predict.

2.3.3 Implications for earthquake source physics

Our results highlight that when seismic rupture efficiently develops, it does not steadily follow the classical t^2 law predicted by classical self-similar equations. While this simple law is seismologically observed when considering the whole rupture duration T (i.e. $M_0 \propto T^3$ (Houston et al., 1998; Bilek et al., 2004; Vallée, 2013; Chounet and Vallée, 2018)), it is transiently not respected during the development phase. Such breaks in scaling laws have been recently found by other authors (Denolle and Shearer, 2016; Archuleta and Ji, 2016). As their spectral observations are not explained by a self-similar Brune (1970) source spectrum with a single corner frequency, they also suggest the existence of a second timescale related to a transient accelerating phase.

As the t^2 law directly comes from the shape of the slip function in equation 2.2 and from the constant stress drop and rupture velocity hypotheses, at least one of these assumptions should not be respected during the development phase. The radial model can for example be questioned based on numerical dynamic and kinematic studies (Das and Kostrov, 1983; Dunham et al., 2003; Beroza and Spudich, 1988; Zhang et al., 2012) showing that the main asperity may break inward after being encircled by the rupture front. But while this process is expected to generate a large transient moment acceleration, it is less clear how it can reproduce a power law similar to what we observe. If remaining in a radial model with constant rupture velocity, we can also easily derive that a slip function of the form $u(r,t) \propto t^{n_d-2}\sqrt{a^2(t)-r^2}$ would lead to our observed moment rate evolution of the development phase. Such a model implies that stress drop inside the main asperities grows with time (consistent with some studies showing a positive correlation between peak stress drop and magnitude (Mai et al., 2006; Causse et al., 2013)), but as a consequence, it is unlikely that the slip law can be physically written in this case under a simple form similar to equation 2.2.

An interesting analytical configuration, inspired by the model of Sato (1994), is the case of a crack model growing with non constant rupture velocity. We here remain in the general configuration of an unknown average rupture velocity function, that should be regarded as the marker of the surface expansion evolution of the rupture. We now refer to this average rupture velocity as v_{rd} to clearly recall that we are inside the development phase. By equating the theoretical moment function (2.4) and the observed one (2.10), we have:

$$M_d(t) = \frac{2\pi}{3}\Delta\sigma a^3(t) = \frac{\alpha_d}{n_d+1}t^{n_d+1} \tag{2.11}$$

which leads to:

$$a(t) = \int_0^t v_{rd}(u)du = \left(\frac{3\alpha_d}{2\pi\Delta\sigma(n_d+1)}\right)^{\frac{1}{3}} t^{\frac{n_d+1}{3}} \tag{2.12}$$

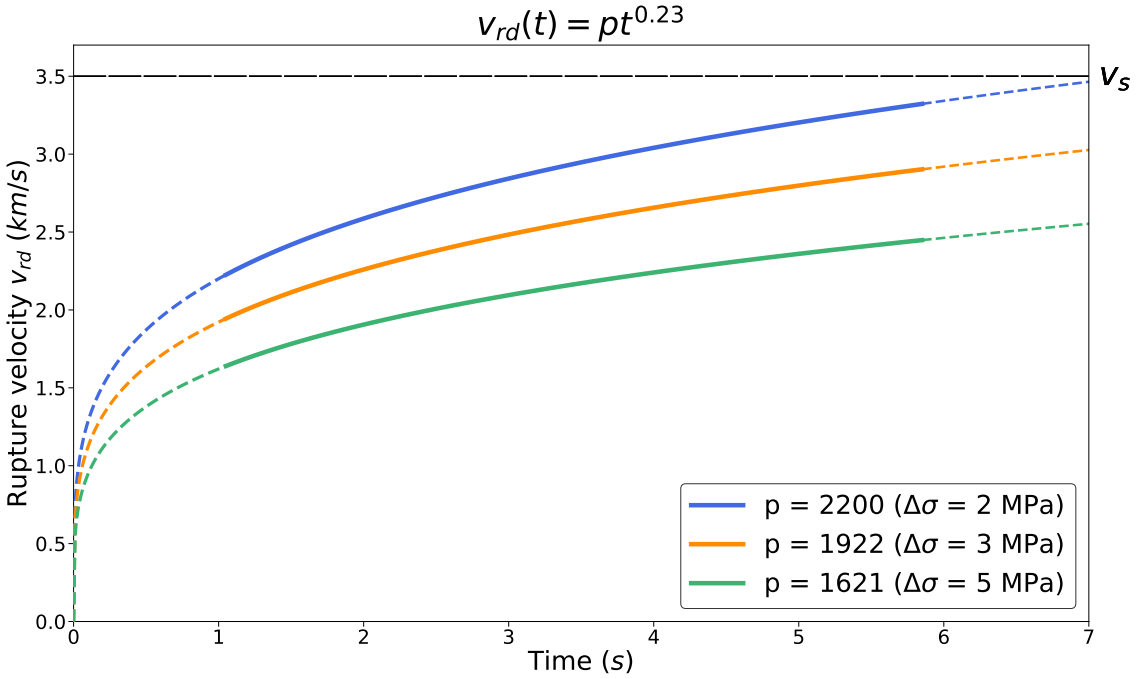

Figure 2.5 – Rupture velocity acceleration during the development phase, as constrained by a crack model with constant stress drop. Each curve shows the equation $v_{rd}(t) = pt^{\gamma}$ for γ fixed to the obtained value (0.23) and different values of p (controlled by $\Delta\sigma$). Outside the time window directly constrained by the observations (between ~ 1 s and ~ 6 s, see Figure 2.4), the curves are dashed. v_s is the shear wave velocity, here fixed at a classical $3.5\,\mathrm{km.s^{-1}}$ crustal value.

and finally to the determination of the rupture velocity evolution:

$$v_{rd}(t) = \left(\frac{\alpha_d (n_d + 1)^2}{18\pi\Delta\sigma} \right)^{\frac{1}{3}} t^{\frac{n_d - 2}{3}} \equiv pt^{\gamma} \tag{2.13}$$

This derivation therefore shows that the observed power law for the moment rate function can be fully explained by rupture velocity acceleration. Rupture velocity is shown to follow a power law function with an exponent $\gamma \simeq 0.23$ and a factor p inversely proportional to $\Delta\sigma^{1/3}$. The crack model considered here (equation 2.2) can be modified to include a process zone of size δ_r at the tip, preventing the slip rate to diverge at the edges of the slipping zone. In this case, equation 2.2 remains valid for $r \leq a(t) - \delta_r$, where slip rate is maximum (and finite). This leads to a rupture velocity correlated with peak slip rate, as the slip rate calculated at δr just behind the rupture front $\dot{u}(a(t) - \delta r, t)$ grows as $v_{rd}(t)\sqrt{a(t)/\delta r}$, or as $t^{\frac{3\gamma+1}{2}}$ if retaining only the time dependency. This derivation is consistent with dynamic models (Schmedes et al., 2010; Bizzarri, 2012) showing that during rupture propagation, there is a positive spatial correlation between rupture velocity and peak slip rate. In contrast, the classical crack model does not lead to this correlation because peak slip rate increases as $\sqrt{t}$ while rupture velocity remains constant.

We show in Figure 2.5 the time evolution of v_{rd} for three realistic values of $\Delta\sigma$. In the sampled part of the development phase (between ~ 1 s and ~ 6 s) and for the realistic values of $\Delta\sigma$ shown in Figure 2.5, $v_{rd}(t)$ gradually increases and is in a classical rupture velocity range of $1.5\,\mathrm{km.s^{-1}}$ to $3\,\mathrm{km.s^{-1}}$ (Geller, 1976; Doornbos, 1982; Somerville et al., 1999;

McGuire et al., 2002; Chounet et al., 2017). This behavior may however be questionable for two reasons. For rupture times approaching zero (not directly sampled in the develoment phases), the power law predicts slow rupture velocities, that have not been observed for microearthquakes (McGuire, 2004; Abercrombie et al., 2017). This requires that rupture accelerates even more abruptly in the initial instants following rupture initiation. Rupture velocity evolution also indicates that larger earthquakes, which have longer development phases, are expected to have higher local rupture velocities. However, in the magnitude range of the SCARDEC catalog, a scaling between rupture velocity and final magnitude has not been clearly observed in kinematic source analyses (Hayes, 2017; Ye et al., 2016).

The origins of the observed moment rate evolution may finally be searched in models where rupture velocity and/or stress drop have a random variability. Such models are not expected to individually follow a power law but they may collectively reproduce the average behavior of the development phase. This class of stochastic models could additionally remain self-similar, without requiring to introduce differences between small and large earthquakes.

2.4 Different behaviors between development phase and early rupture stage

The development phase does not necessarily occur at early times of the rupture process. As a consequence, we do not expect to find the same time dependencies as studies focusing on how rupture starts, with reference to the earthquake origin time (Melgar and Hayes, 2017; Meier et al., 2017). In particular, we expect the latter studies to find a less pronounced time dependency, in an average sense, due to inclusions of earthquakes with low initial moment release. In this section, we further illustrate how an average linear time dependency of the growing rupture process (Meier et al., 2017) can be approached from rupture variability rather than from intrinsic rupture properties.

To do so, we build a synthetic catalog of bimodal STFs, by summing two sub-events growing both as $\dot{M}(t) = \alpha(t - t_d)^n$ where α and n randomly vary around the observational values of α_d and n_d. $t_d = 0$ for the first subevent and t_d take random values between 0 and $T_0/2$ for the second subevent, where the STF total duration T_0 takes into account the observed variability around its magnitude-dependent scaling law (Courboulex et al., 2016). By also varying the relative durations (and hence moments) between the first and the second subevent, we generate a synthetic catalog with a large diversity, mimicking the main STF characteristics observed in the SCARDEC catalog: simple STFs with early development phases are obtained when the first sub-event dominates, while complex ruptures, with delayed development phases, are simulated when the second sub-event dominates. More details on the generation of this synthetic catalog are provided in Section 2.7.2 and Figure 2.9 of the Supplementary Materials, and Figure 2.6 shows examples of five synthetic $M_w = 7$ STFs, illustrating their large diversity.

Using the synthetic catalog, we compute the median values of the STFs at each time, as done by Meier et al. (2017) using the real STF catalogs of Ye et al. (2016), Hayes (2017) and Vallée and Douet (2016). Figure 2.7 shows the obtained median STFs for 6 magnitude

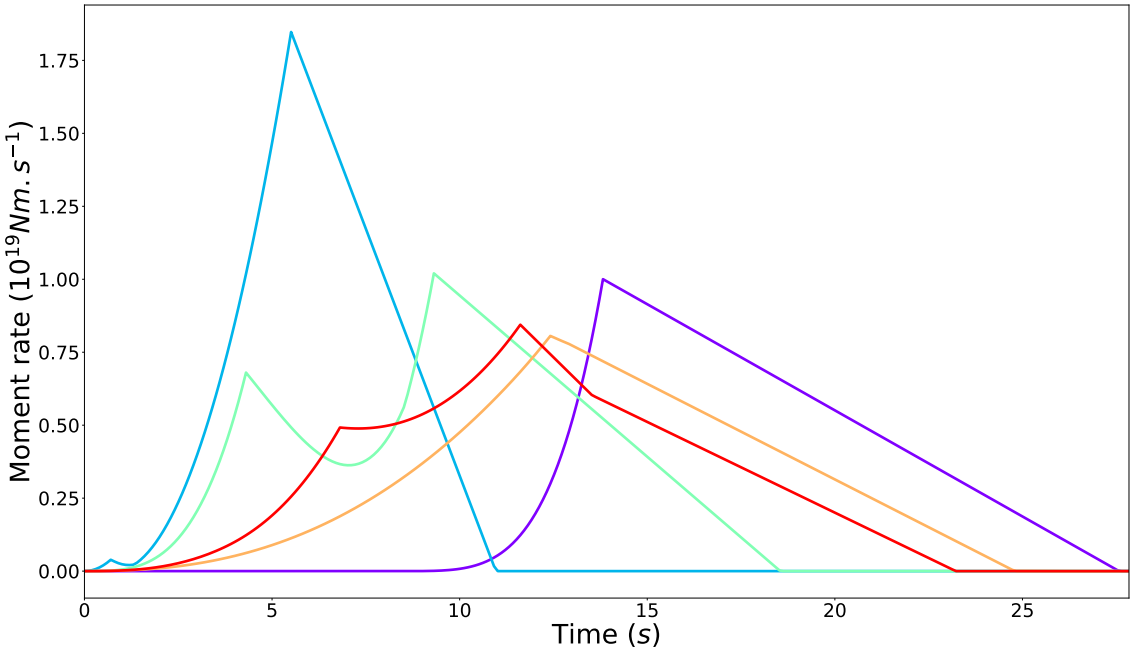

Figure 2.6 – Examples of 5 synthetic STFs of $M_w = 7$, illustrating the diversity of STF shapes in the synthetic catalog.

bins between $M_w = 7$ and $M_w = 8$. No early magnitude-dependent signal is observed, as the median STFs grow in a indistinguishable way before the smallest earthquakes approach their peak. The non-linear signal at the very beginning of each median STF is expected since all STFs have a first sub-event growing with an n exponent distribution centered on $n_d = 2.68$. This early non-linearity is also observed in the average source time functions of Melgar and Hayes (2017). Median STFs then have a flatter trend than individual subevents (equation 2.10), as a result of STF diversity.

This synthetic catalog therefore illustrates how the early stages of the STFs can have average characteristics which are difficult to translate in terms of physical rupture properties. The linear behavior observed by Meier et al. (2017) quantifies how rupture starts, on average, and is useful from a practical point of view to characterize a standard STF shape. However, as we here show that this behavior can mainly result from the combined effects of non-linear development phases and rupture diversity, its interpretation in terms of rupture dynamics must be done with care.

2.5 Conclusion

In this study, the development phase is defined as the growing phase directly preceding the peak moment rate. As such, it is not expected to behave the same way as the early stage of the seismic rupture. We here systematically extract the development phase of 2221 STFs from the SCARDEC database in order to quantify its time evolution. For this purpose, we compute the moment acceleration (STF slope) at several moment rates, within the development phase. We first show that no magnitude-dependent signal appears, favoring a process where small and large earthquakes only differ in the duration of their

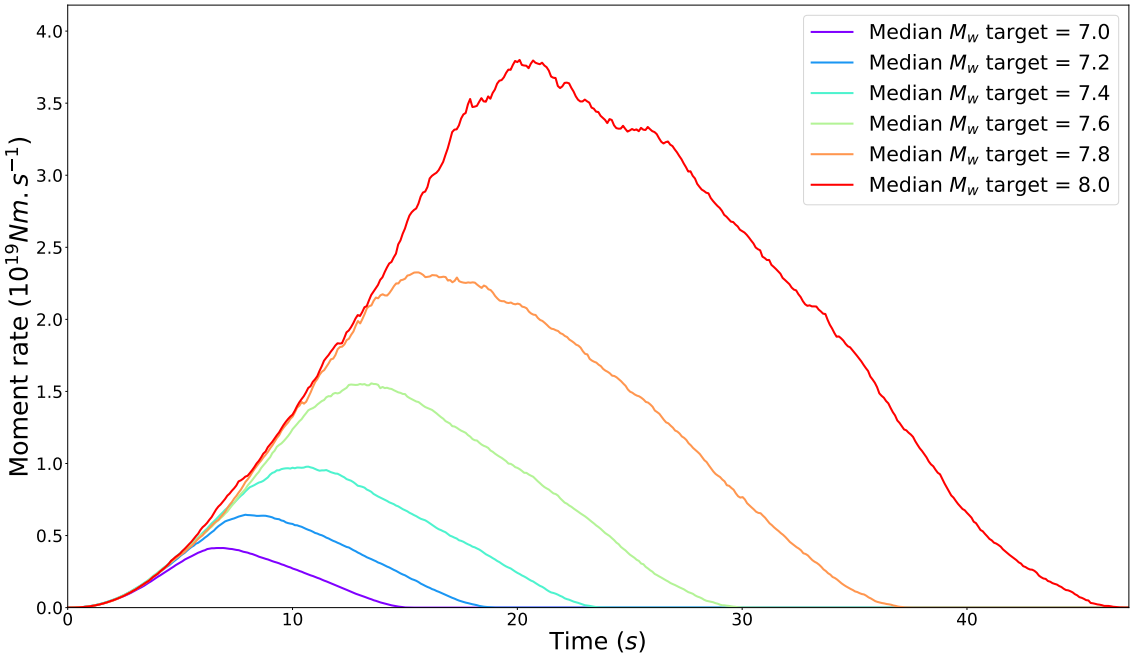

Figure 2.7 – Median synthetic STFs from $M_w = 7$ to $M_w = 8$, shown in 0.2 magnitude bins. Each median STF is computed from a large number of STFs whose diversity is illustrated in Figure 2.6.

development phase. Further analysis then highlights that rupture time evolution inside the development phase differs from the classical steady self-similar growth (where moment rate develops as t^2): the moment rate of the development phase $\dot{M}_d$ rather develops as $\dot{M}_d \propto t^{n_d}$ with $n_d \simeq 2.7 \pm 0.11$ at the 90% confidence level.

Such deviation with respect to the steady quadratic growth can be due to a combination of factors. Non-circular rupture geometry, or transient variations of stress drop and rupture velocity, may increase the time exponent of $\dot{M}_d$. We analytically developed one of the end-member cases, where the exponent excedence compared to the self-similar growth is purely due to monotonic rupture velocity variations. In this configuration, rupture velocity v_{rd} inside the development phase is itself shown to follow a power-law time function, with $v_{rd} \propto t^{0.2}$. Due to this low exponent, v_{rd} is expected to quickly reach classical rupture velocities ($> 1\,\mathrm{km.s^{-1}}$) and then to increase only moderately in the sampled part of the development phase (between $\sim 1\,\mathrm{s}$ and $\sim 6\,\mathrm{s}$) More generally, even if the observed time-dependency of the development phase may have several causes, it should give a new observational constraint to assess the realism of dynamic rupture scenarios.

2.6 Acknowledgments

We thank Pascal Bernard, Claudio Satriano, Alexandre Schubnel, Hideo Aochi for constructive remarks on this work. Fruitful discussions with Men-Andrin Meier improved our analysis of median STFs and the generation of the synthetic catalog. Constructive reviews provided by Gavin Hayes and an anonynous reviewer helped us to improve the original manuscript. We are grateful to the FDSN, for the public availability of the broadband seismograms of the global network, and to the IRIS Data Center and

IPGP data center for easy access to the data. SCARDEC database is available at http://scardec.projects.sismo.ipgp.fr. This study contributes to the IdEx Université de Paris ANR-18-18-IDEX-0001.

These supplementary materials first include Section 2.7.1 and the associated Figure 2.8(a), detailing the method used to estimate the confidence intervals of the parameters relating moment acceleration to moment rate. Confidence intervals for the parameters of the time evolution of the moment rate are then computed and shown in Figure 2.8(b). Section 2.7.2 and the associated Figure 2.9 explain how the synthetic catalog of bimodal STFs is generated, with the aim of reproducing the main shape of the SCARDEC STFs. The independency between the moment acceleration and final magnitude is shown for all the prescribed moment rates in Figures 2.10 to 2.19. Finally, the relation between moment acceleration and moment rate, for lower and upper limits of the development phase at $0.05\,F_m$ and $0.5\,F_m$, respectively, is shown in Figure 2.20.

2.7 Supplementary materials

2.7.1 Statistical analysis for m, β, n_d and α_d values

In this section we show how the confidence intervals for the fitting parameters m, β, n_d and α_d are obtained. For that, we consider the 40 prescribed moment rates (see main text for details). For each moment rate, we randomly select 75 different $(\ddot{M}_d)_{ij}$ values, so that we consider the same number of observations for small and large moment rates (as $N_{40} = 75$). Then a linear fit (in log-log scale) is performed for the 75×40 data points extracted, providing a first possible m and a first $b = \log \beta$. We iterate the procedure of moment acceleration selection and (m, b) estimation 10000 times so that we end up with 10000 (m, b) couples characterizing the 10000 subsets of 75×40 data points extracted from the initial data. We then compute the joint probability density function for m and b, and derive the corresponding confidence map shown in Figure 2.8(a). The confidence map for n_d and α_d shown in Figure 2.8(b) is obtained following the same procedure, after converting the m and b samples to n_d and $\log \alpha_d$ samples. Note that $\log \beta$ and $\log \alpha_d$ show a negative correlation with m and n_d, respectively. The confidence intervals provided in the main text have been estimated from the marginal densities, and should therefore be interpreted according to this trade-off.

2.7.2 Setting-up of the synthetic STFs catalog

We build our catalog of synthetic STFs by combining the macroscopic properties found by past studies with the observed time evolution of the development phase. Intrinsic complexity of the rupture propagation, which leads to the exact shape of each individual STF, prevents from the constitution of a fully realistic synthetic STF catalog. However, diversity in terms of STFs shape can be mainly characterized, for a given seismic moment M_0, by a source duration with a log-normal distribution and a variable number of local peaks. We first generate for each bin of M_w a log-normal distribution of source durations T_i, with a mean $T_0 = 4.5 \cdot 10^{-6}(M_0)^{1/3}$ (self-similar equation of GCMT Ekström et al. (2012)) and a standard deviation $\sigma = 0.37$ (Courboulex et al. (2016)). We then build for

each T_i bimodal STFs, with two sub-events growing as $\dot{M}_d(t) = \alpha_k t^{n_k}$. The first sub-event always starts at time 0 and its growing phase randomly stops between 0 and the half total duration $T_i/2$. Duration of the growing phase of the second sub-event is also randomly selected between 0 and $T_i/2$ but its start is adapted such as the growing phase ends at $T_i/2$. α_i and n_i values for each STF randomly vary around their observational values (8.8×10^{16} and 2.68 respectively). The first subevent has a linear decline with the same duration as its growth while the second subevent always declines linearly from $T_i/2$ to T_i. Figure 2.9 shows an example of how an STF is built with the constraints detailed above.

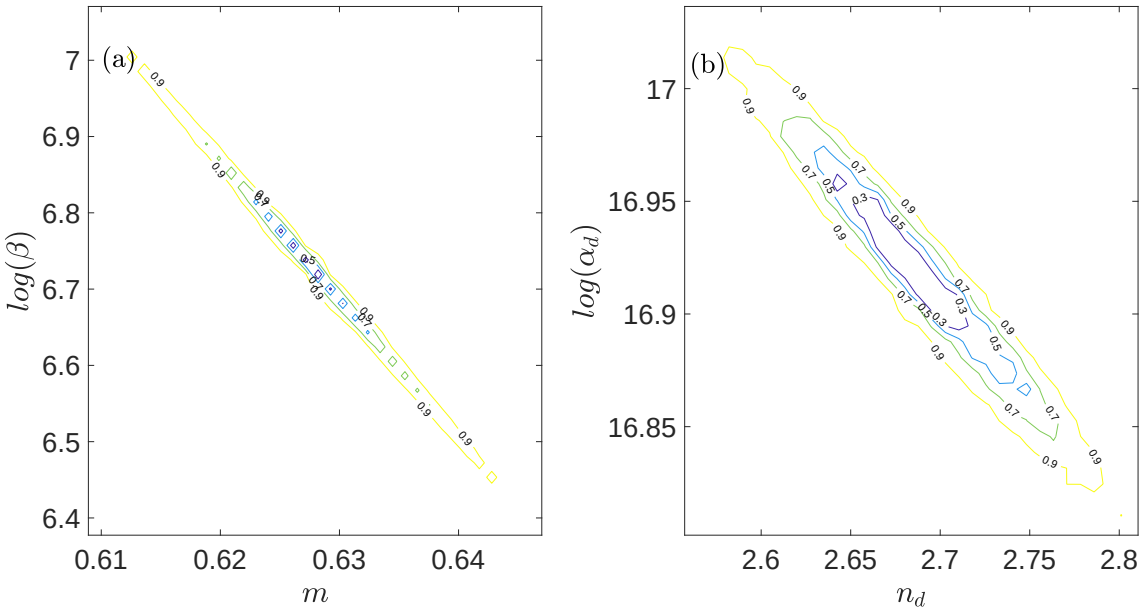

Figure 2.8 – Confidence maps for $(m, b = \log \beta)$ parameters (a), and $(n_d, \log \alpha_d)$ (b). The labels on the contours indicate the confidence level.

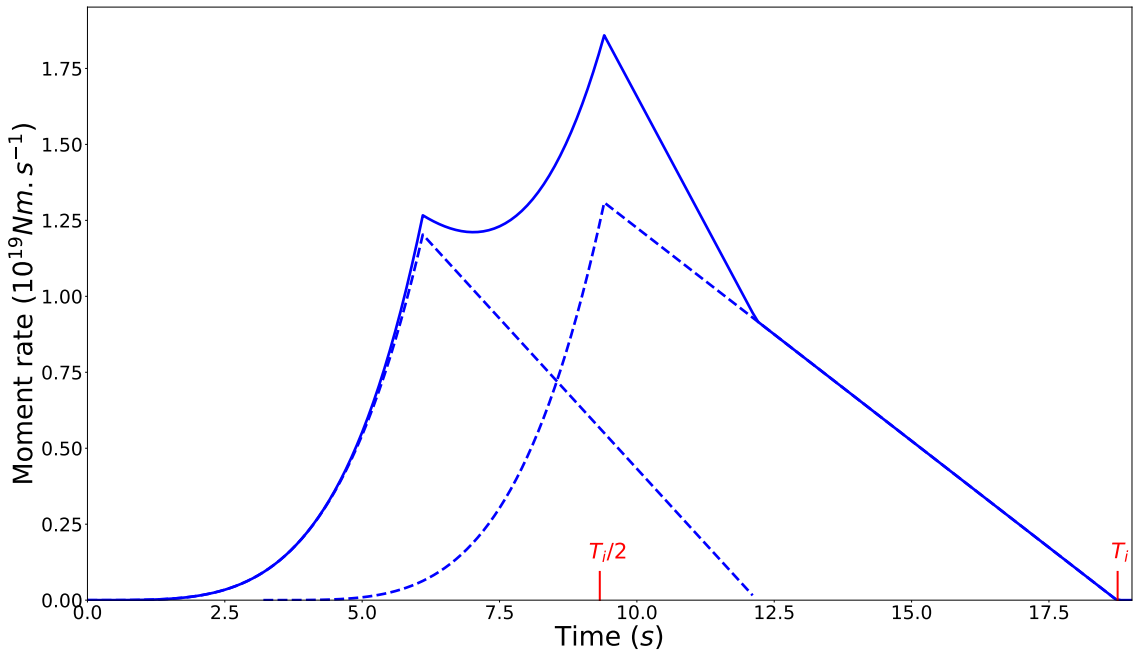

Figure 2.9 – Example of the construction of a synthetic STF. Dashed blue lines represent each of the two sub-events, and the bold blue line is the sum of the two sub-events, i.e. the final synthetic STF. Red ticks show the half-duration and total duration of the STF.

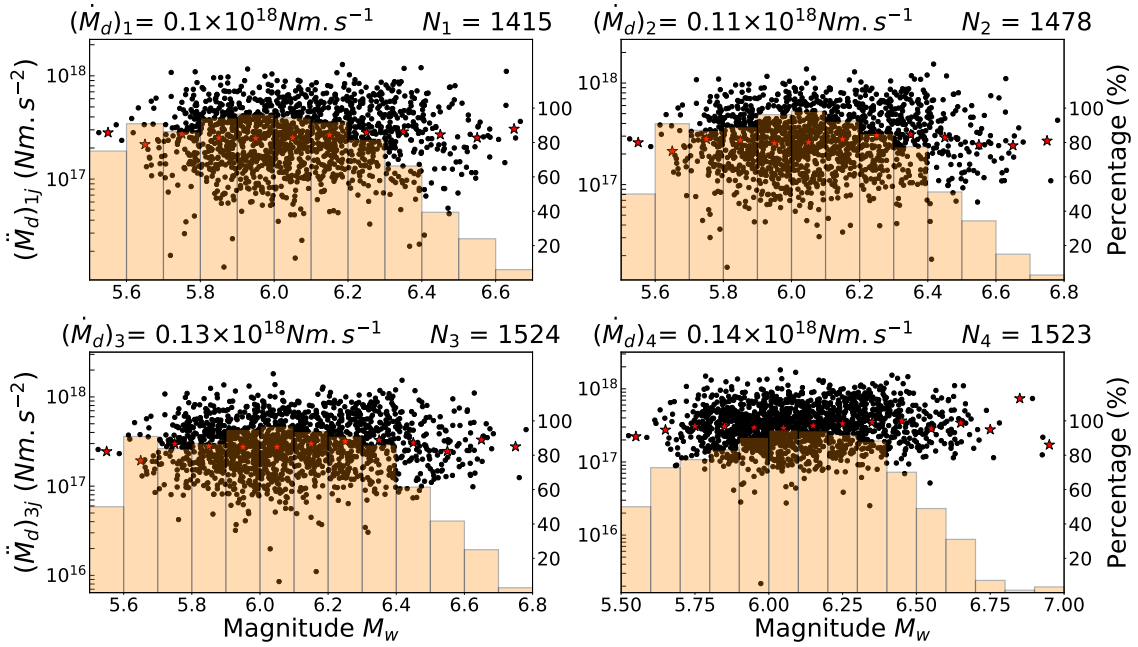

Figure 2.10 – Moment acceleration as a function of magnitude for the four prescribed moment rates ($(\dot{M}_d)_1$ to $(\dot{M}_d)_4$). The filled histogram represents the ratio (in %) of sampled events per range of M_w.

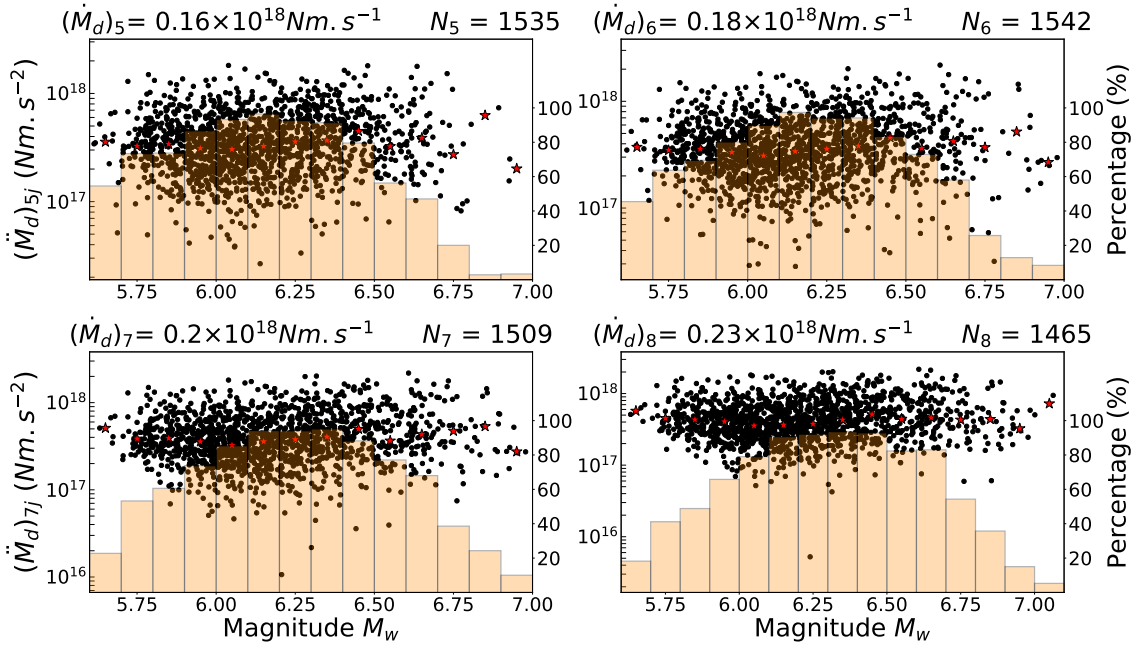

Figure 2.11 – Moment acceleration as a function of magnitude for four prescribed moment rates ($(\dot{M}_d)_5$ to $(\dot{M}_d)_8$). The filled histogram represents the ratio (in %) of sampled events per range of M_w.

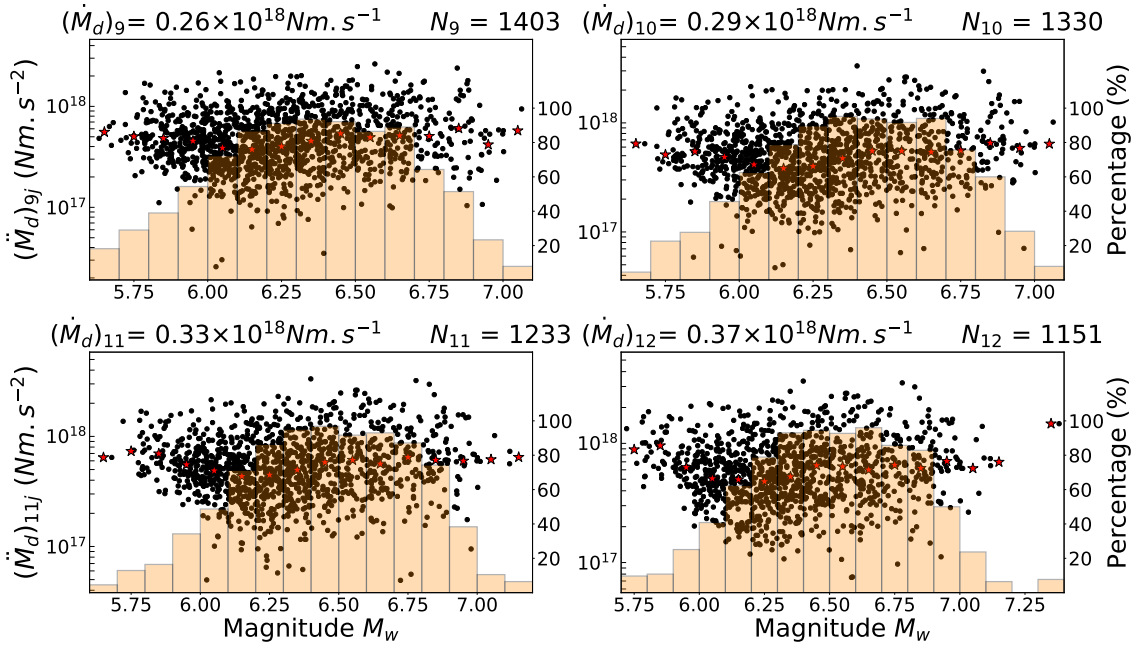

Figure 2.12 – Moment acceleration as a function of magnitude for the four prescribed moment rates ($(\dot{M}_d)_9$ to $(\dot{M}_d)_{12}$). The filled histogram represents the ratio (in $\%$) of sampled events per range of M_w.

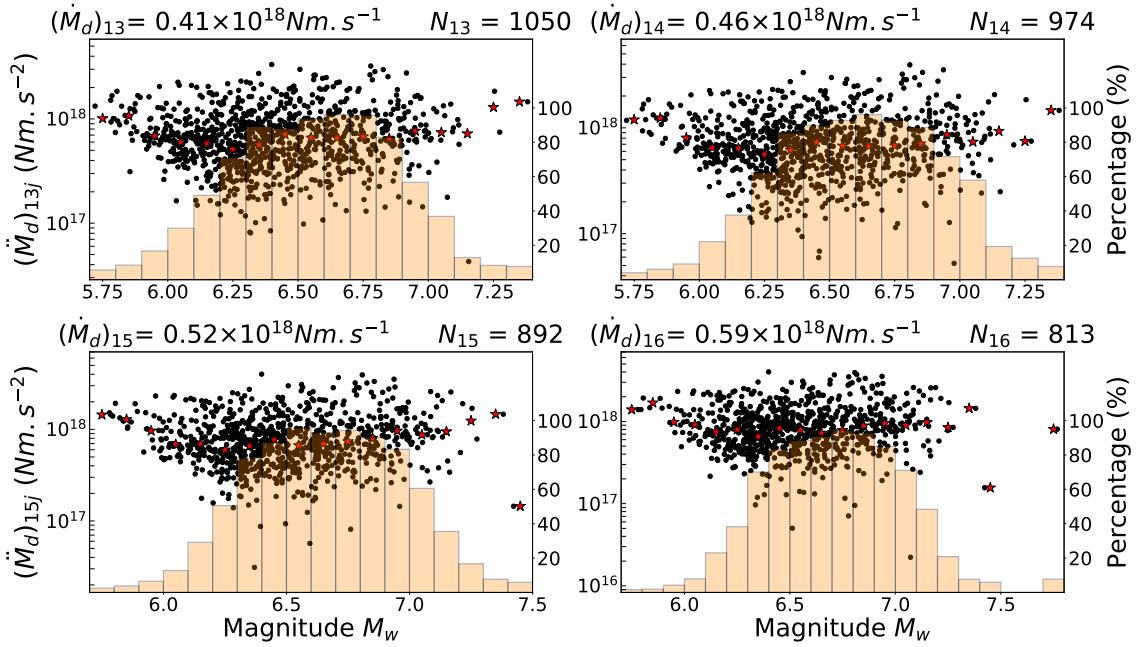

Figure 2.13 – Moment acceleration as a function of magnitude for the four prescribed moment rates ($(\dot{M}_d)_{13}$ to $(\dot{M}_d)_{16}$). The filled histogram represents the ratio (in $\%$) of sampled events per range of M_w.

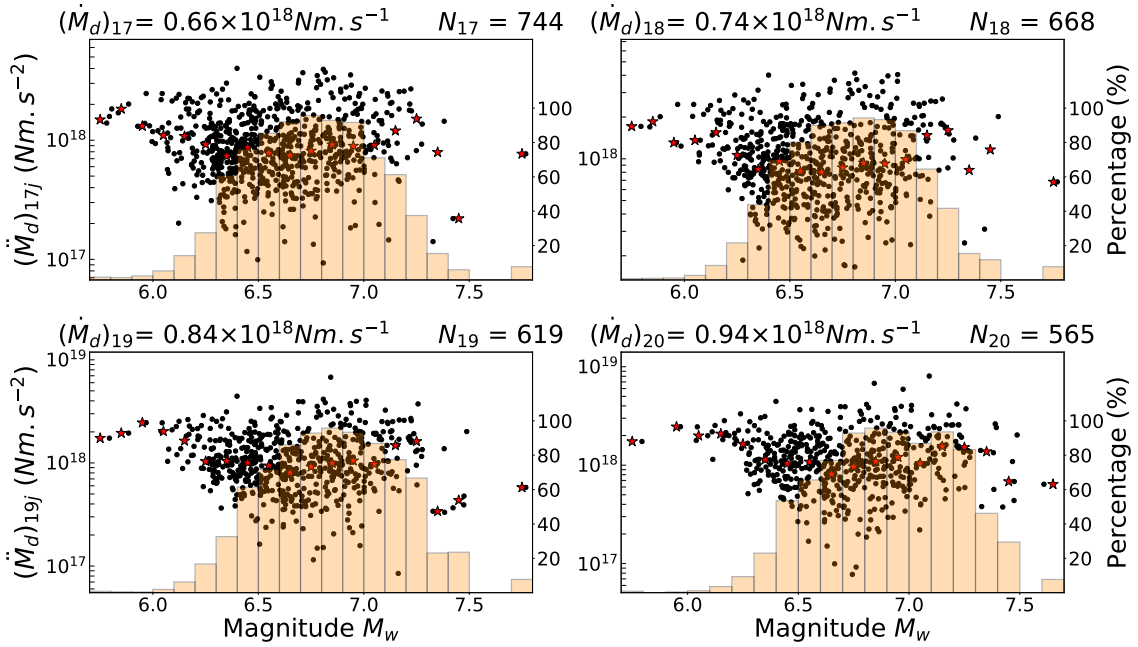

Figure 2.14 – Moment acceleration as a function of magnitude for the four prescribed moment rates ($(\dot{M}_d)_{17}$ to $(\dot{M}_d)_{20}$). The filled histogram represents the ratio (in $\%$) of sampled events per range of M_w.

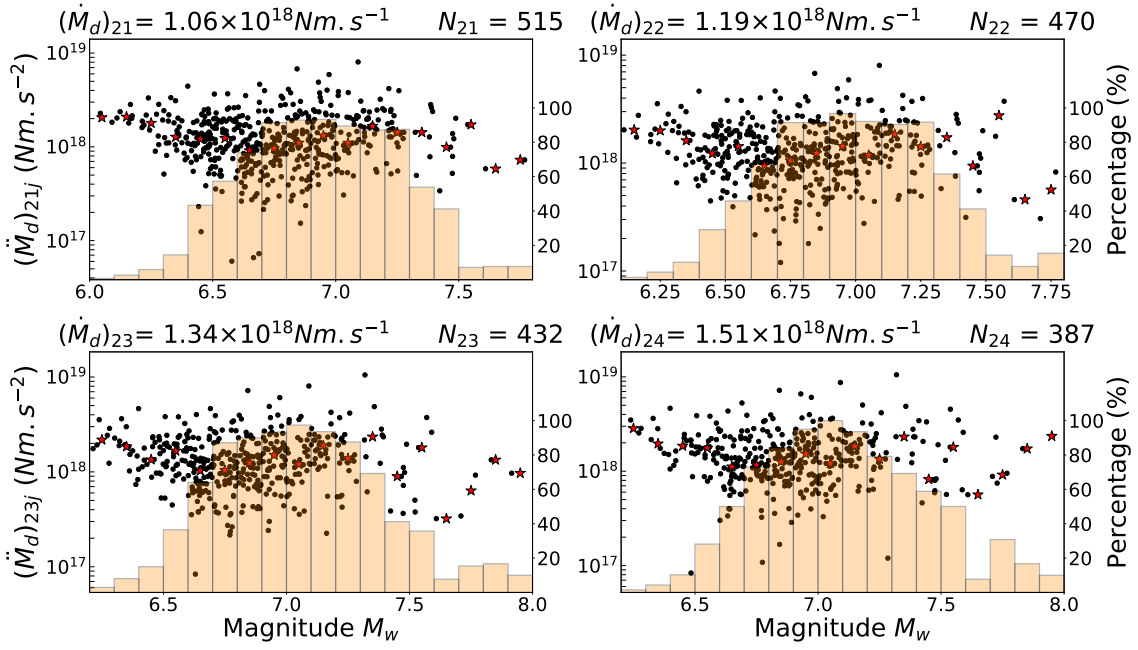

Figure 2.15 – Moment acceleration as a function of magnitude for the four prescribed moment rates ($(\dot{M}_d)_{21}$ to $(\dot{M}_d)_{24}$). The filled histogram represents the ratio (in $\%$) of sampled events per range of M_w.

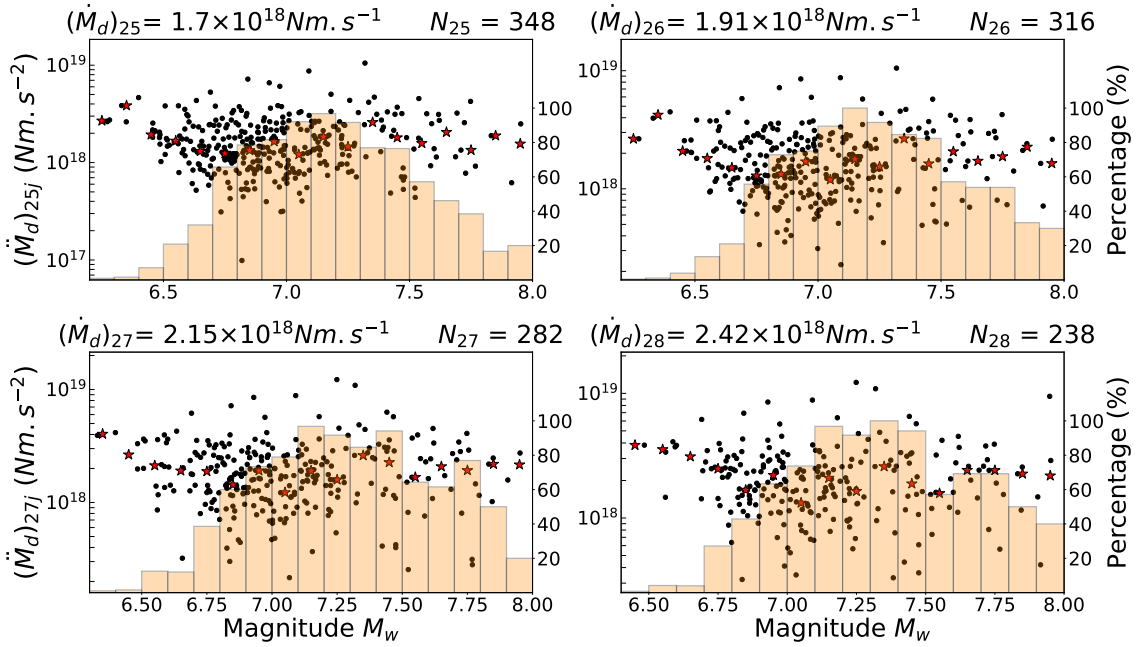

Figure 2.16 – Moment acceleration as a function of magnitude for the four prescribed moment rates ($(\dot{M}_d)_{25}$ to $(\dot{M}_d)_{28}$). The filled histogram represents the ratio (in $\%$) of sampled events per range of M_w.

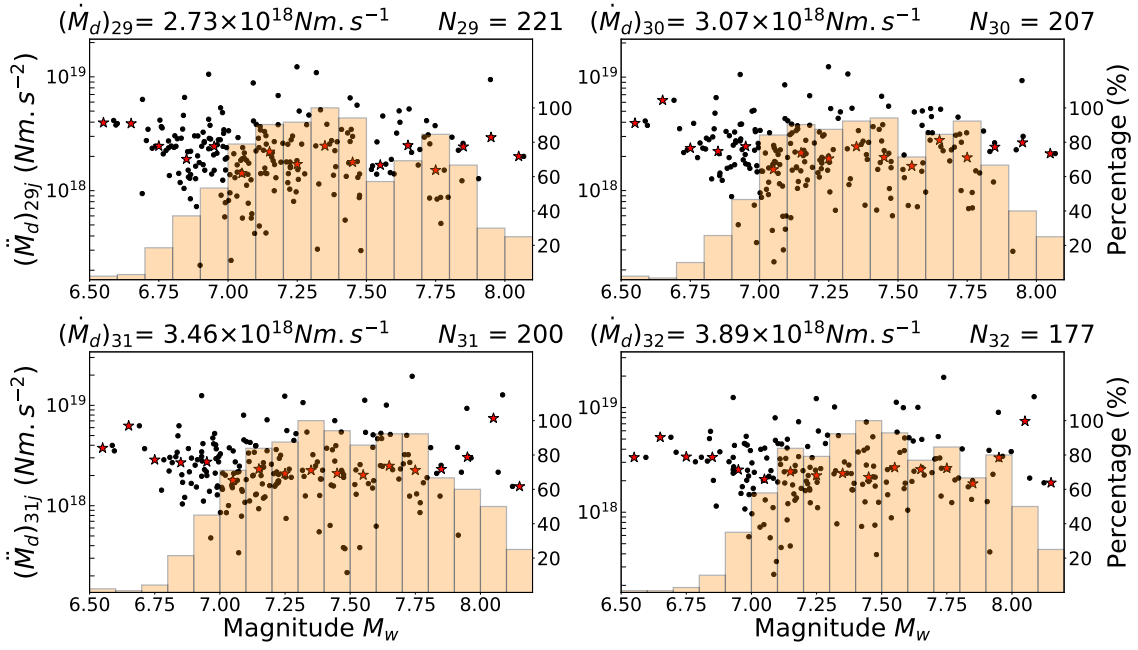

Figure 2.17 – Moment acceleration as a function of magnitude for the four prescribed moment rates ($(\dot{M}_d)_{29}$ to $(\dot{M}_d)_{32}$). The filled histogram represents the ratio (in $\%$) of sampled events per range of M_w.

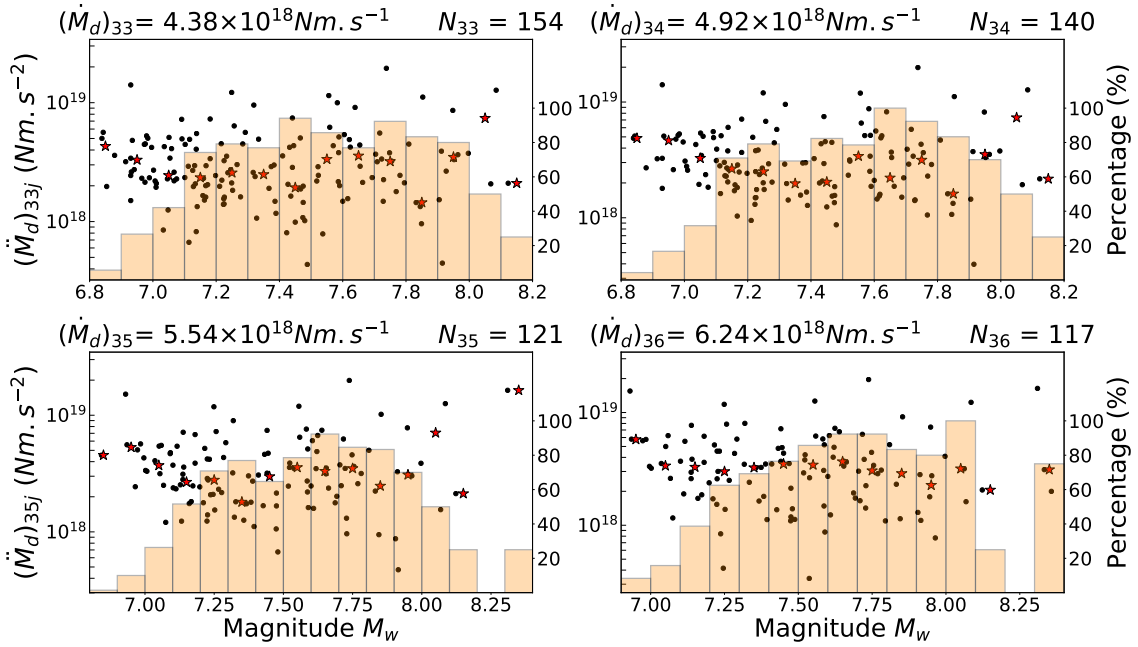

Figure 2.18 – Moment acceleration as a function of magnitude for the four prescribed moment rates ($(\dot{M}_d)_{33}$ to $(\dot{M}_d)_{36}$). The filled histogram represents the ratio (in $\%$) of sampled events per range of M_w.

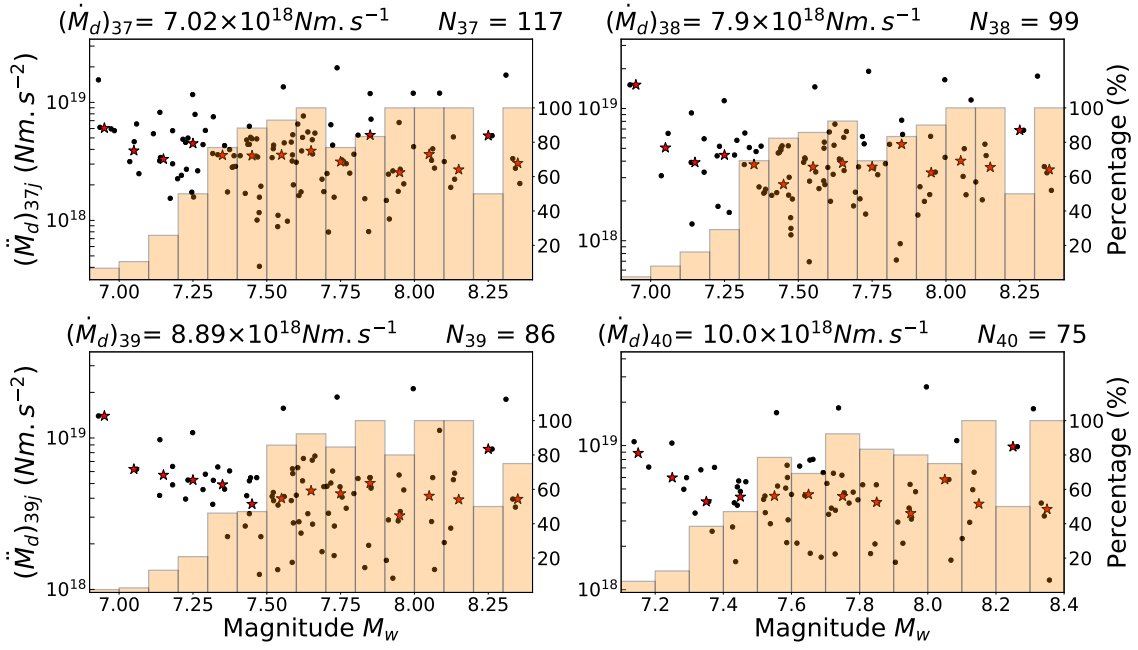

Figure 2.19 – Moment acceleration as a function of magnitude for the four prescribed moment rates ($(\dot{M}_d)_{37}$ to $(\dot{M}_d)_{40}$). The filled histogram represents the ratio (in $\%$) of sampled events per range of M_w.

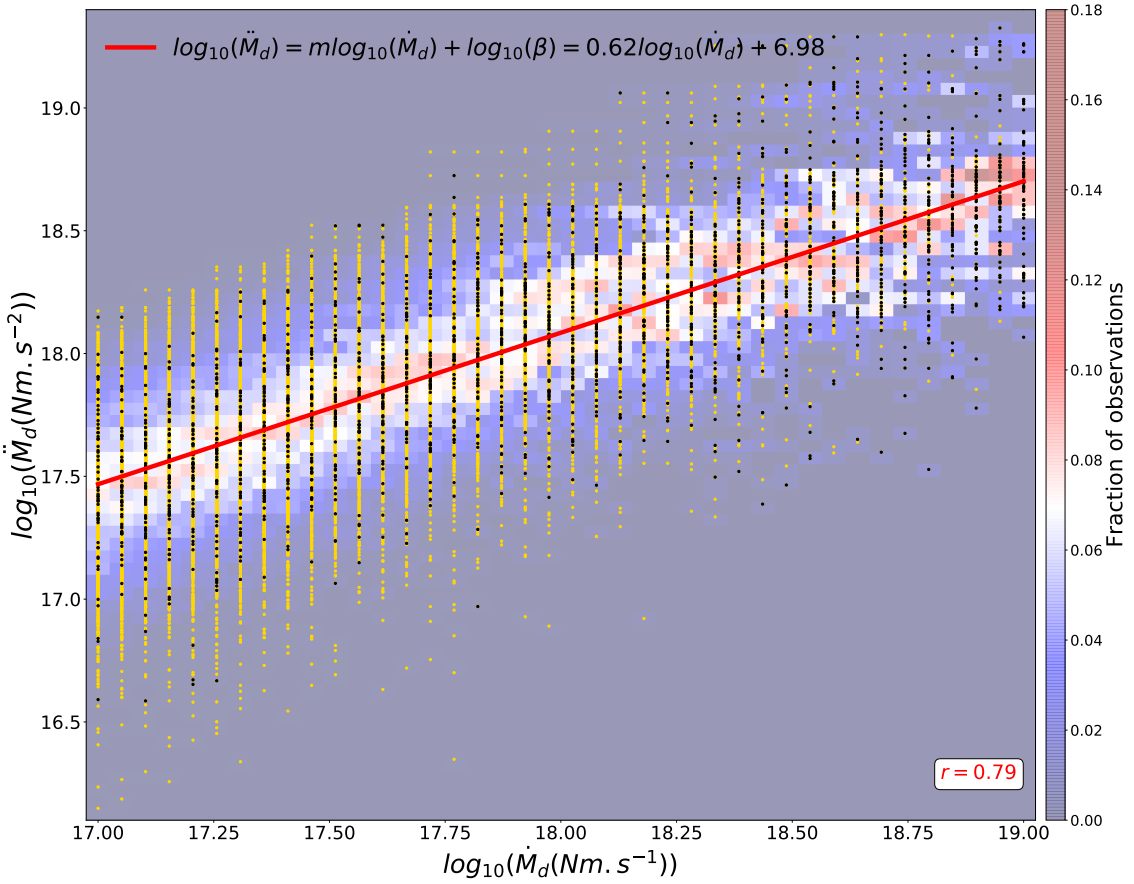

Figure 2.20 – Same Figure as Figure 2.3 but with a development phase extracted between 0.05 F_m and 0.5 F_m.

Chapitre 3

Analysis of rupture parameters during the development phase in kinematic source models

Ce chapitre propose une analyse du comportement des paramètres de source dans le cas d'une représentation cinématique des séismes. Dans un premier temps, le catalogue *SRCMOD*, une base de données de distribution du glissement de séismes obtenue par inversion cinématique sur une faille finie, est utilisée pour étudier la variation spatiale de la chute de contrainte statique. La phase de développement est considérée ici comme la zone sur la faille où le glissement principal s'effectue. Les résultats préliminaires suggèrent que la chute de contrainte moyenne sur ces zones ne dépend pas de la taille finale des séismes, ce qui indique que le comportement d'autres paramètres cinématiques est à l'origine de nos observations. Dans cet esprit, nous présentons alors le cas d'un crack analytique où une forte variation radiale de la vitesse de rupture est ajoutée. Dans ce modèle, où la chute de contrainte statique est constante, les observations du catalogue SCARDEC faites dans le Chapitre 2 sont reproduites. Même si ce modèle simple présente des limitations, il met en évidence que la corrélation entre la vitesse de rupture et de glissement donne naissance à des comportements transitoires équivalents aux observations, tout en respectant les lois globales auto-similaires. Enfin, le modèle de source RIK, dans lequel un séisme est considéré comme un ensemble de sous-événements dont la taille et le glissement associés suivent une loi fractale, est adapté pour étudier le cas d'une représentation plus réaliste des séismes. Il en ressort que le temps de montée joue un rôle important sur la valeur de l'accélération du moment pendant la phase de développement. La corrélation entre la vitesse de rupture et de glissement semble également être une caractéristique nécessaire à la génération de fortes accélérations de moment. Cependant, le modèle RIK présente certaines limitations car à l'inverse du modèle de crack, l'histoire passée de la rupture ne contrôle pas la propagation de la rupture. Ces interprétations suggèrent l'ajout d'un aspect dynamique dans les modèles de développement de la rupture.

3.1 Stress drop analysis with SRC kinematic inversions catalog

The temporal evolution of the moment rate, which deviates from the classical steady t^2 growth in the development phase requires to investigate in more detail similarities between observations and kinematic models of seismic source. As previously explained, the classical view of rupture propagation with a constant stress drop and rupture velocity may not be valid when earthquakes are developing. In addition to the analytical formulation of a monotonic increase of the rupture velocity, a second end-member case that can be directly tested is a variation of stress drop related to the duration of the development phase. As this duration is increasing with the final size of earthquakes, we investigate the evolution of the stress drop as a function of magnitude. While global stress drop values have been often estimated directly from STFs database or analysis with point-source models, this latter parameter is not straightforward to extract for transient parts of STFs (as the development phase). In order to overcome this limitation, we opt for a stress drop analysis using the *SRCMOD* kinematic inversions catalog, a database containing more than 300 finite-fault earthquake source models (Mai and Thingbaijam, 2014). Such models are obtained by inversion techniques using geodetic and/or seismological data and provide slip scenarios on fault. Such a catalog has the disadvantage to have a small number of events in comparison with the SCARDEC catalog but has the benefit of providing a complementary description of earthquakes. Spatial and sometimes temporal slip distribution retrieved by

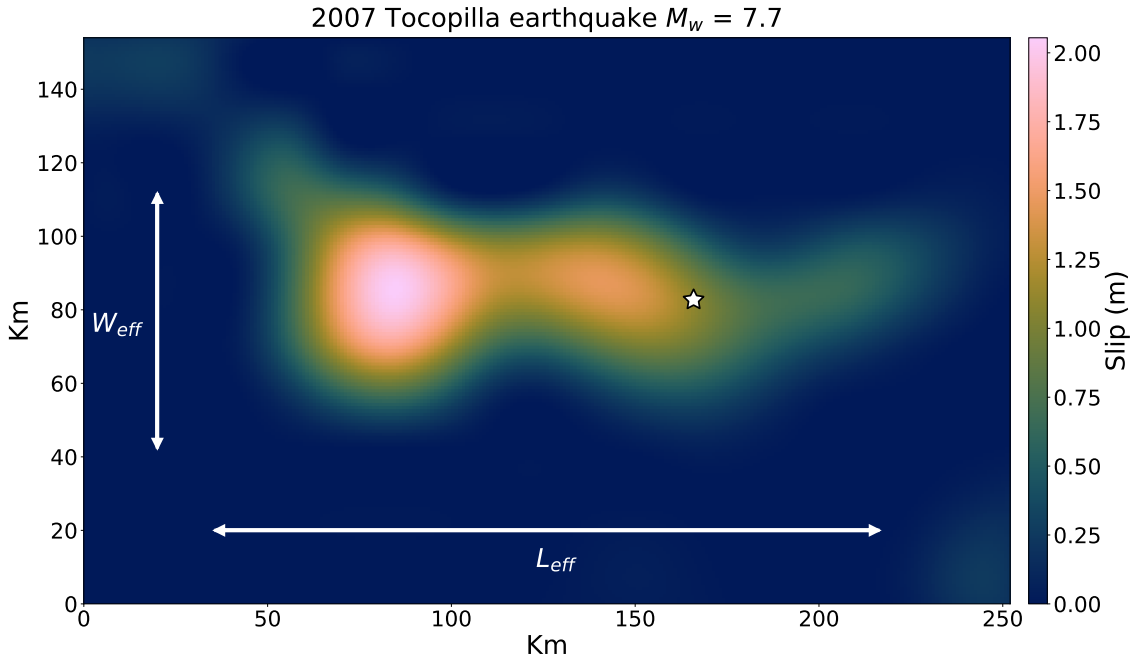

Figure 3.1 – Slip distribution obtained by Béjar-Pizarro et al. (2010) for the 2007 Tocopilla earthquake M_w 7.7 using InSAR and GPS data. White star is the hypocenter location. W_{eff} and L_{eff} are the effective width and length of the fault respectively computed using the definition of Mai and Beroza (2000).

these inversions allows to determine a map of stress drop instead of a single mean value in the case of point-source approximation.

The purpose of this approach is therefore to compute the map of static stress drop associated with coseismic slip. To do so, all the models from the *SRCMOD* database are potentially useful, however, we select only joint inversions whose slip distribution has been determined with a least two different types of data. This selection favors robust source models, in which slip maps are well constrained. Figure 3.1 represents one of these models, the 2007 Tocopilla M_w 7.7 earthquake studied by Béjar-Pizarro et al. (2010) who image slip distribution using InSAR and GPS data. As clearly shown in Figure 3.1 and for the other models, dimensions of faults are often overestimated in order to be sure to include the entire rupture process. We consequently use the effective width W_{eff} and length L_{eff} to have an appropriate estimation of the source dimensions. We reproduce exactly the same methodology as in the study of Mai and Beroza (2000), who use the concept of auto-correlation width. An effective average slip ΔU_{eff} is also computed based on the effective dimensions of the fault and the seismic moment found by the inversion.

The 76 slip maps inferred from joint inversions are then used to compute stress drop maps. We apply the formula of Sato (1972) which derives an expression of the static stress drop at each point (x, y) of a finite fault such as

$$\Delta\sigma(x,y) = \frac{\mu}{8\pi^2}\int_{-\infty}^{+\infty}\int_{-\infty}^{+\infty}\frac{2\gamma\xi^2+\eta^2}{\sqrt{\xi^2+\eta^2}}\Delta u^*(\xi,\eta)e^{-i(\xi x+\eta y)}\mathrm{d}\xi\mathrm{d}\eta, \tag{3.1}$$

where $\Delta u^*(\xi,\eta)$ is the spatial Fourier transform of the coseismic slip $\Delta u(x,y)$ with ξ and

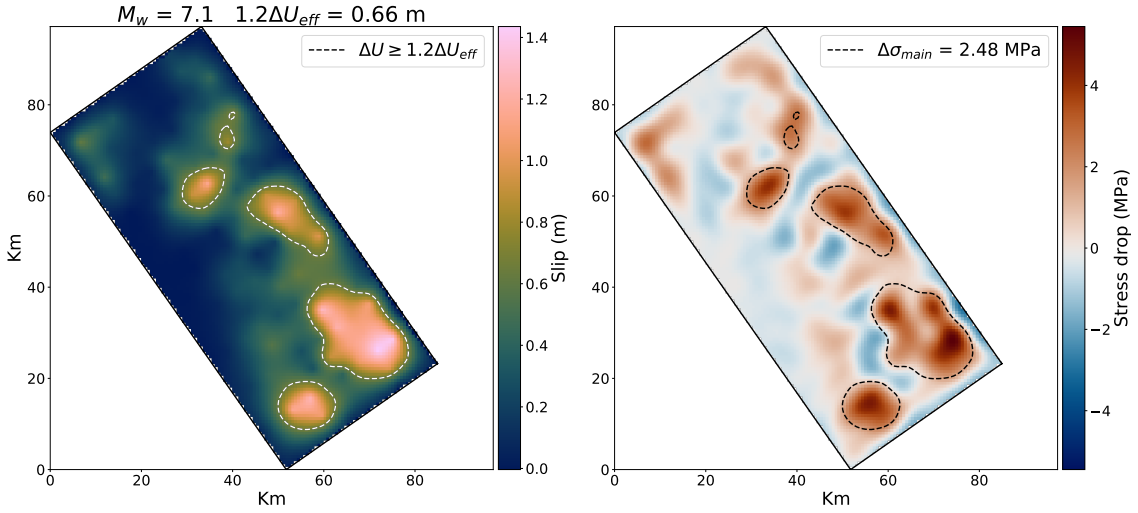

Figure 3.2 – On the left, slip distribution obtained by Hartzell and Mendoza (1991) for the 1978 Tabas earthquake M_w 7.1 using Strong Motion and Teleseismic data. On the right, stress drop distribution inferred from the coseismic slip. Dashed line represents the area where the slip is greater than $1.2\Delta U_{eff}$. $\Delta\sigma_{main}$ is the average stress drop inside this area.

η the spectral coordinates, μ and λ the Lamé coefficients and $\gamma = \frac{\lambda+\mu}{\lambda+2\mu}$. In order to prevent bias due to the slip discretization of each fault, we interpolate slip values so that all the slip maps have the same 150×150 discretization points. Stress drop maps of three different slip models are shown in Figures 3.2, 3.3, 3.4. Positive values of stress drop are well correlated with area of high slip values and negative stress drop patches are associated with low slipping zones in the vicinity of high slip areas.

Stress drop distribution on the entire fault presents an overall view of the rupture process, however a spatial selection is required to approximately locate where the development phase occurs. Following the work of Causse et al. (2013), we select areas that slip more than 1.2 % of ΔU_{eff}, which are represented by dashed lines in Figures 3.2, 3.3, 3.4. Such areas containing most of the slip are likely to contribute to the development phase, in the sense that they are responsible for the main seismic moment episode(s) on the fault. We finally average the stress drop inside these areas that we call $\Delta\sigma_{main}$ and we test its variability with respect to the seismic moment of events. According to our observations in Chapter 2, we expect an increase of $\Delta\sigma_{main}$ if considering that rupture velocity increase is not fully responsible for the non self-similar behavior of the development phase. We represent in Figure 3.5 $\Delta\sigma_{main}$ as a function of the seismic moment of earthquakes. As some earthquakes have been widely studied (Tohoku, Denali, Maule, etc.), resulting in several slip models and consequently stress drop maps for one event, $\Delta\sigma_{main}$ in this configuration is the mean of $\Delta\sigma_{main}$ of each stress drop map.

Figure 3.5 exhibits no particular correlation between $\Delta\sigma_{main}$ and M_0, but rather a high variability of $\Delta\sigma_{main}$, with values varying of more than one order of magnitude. These results indicate that from the smallest M_w 5.5 to the biggest Tohoku M_w 9.1 earthquake, there is statistically the same $\Delta\sigma_{main}$. This scale independence, as in case of the global static stress drop, would imply that the ratio between the maximum slip over the length of the main patches remains constant for a large magnitude range. Such observations

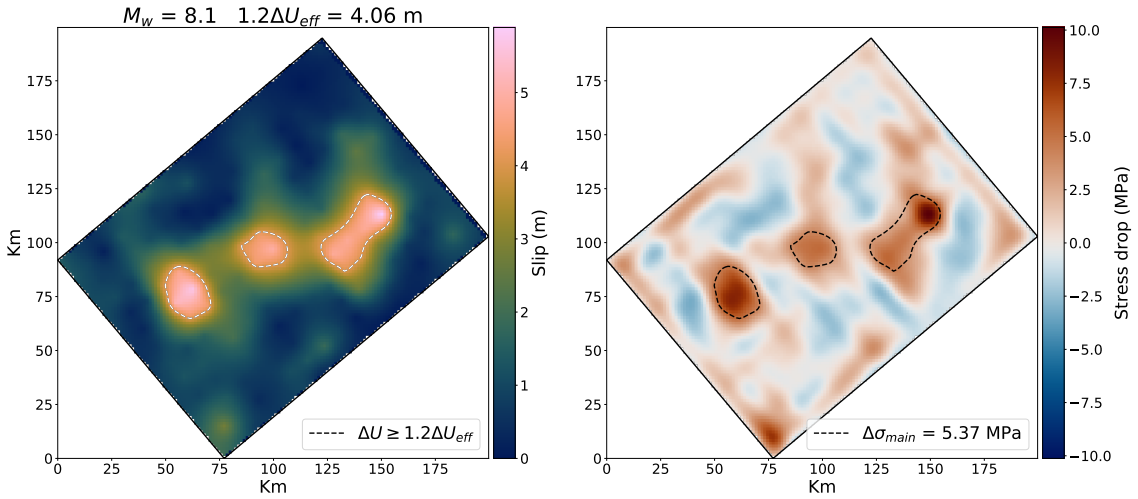

Figure 3.3 – On the left, slip distribution obtained by Yagi (2004) for the 2003 Tokachi earthquake M_w 8.1 using Strong Motion and Teleseismic data. On the right, stress drop distribution inferred from the coseismic slip. Dashed line represents the area where the slip is greater than $1.2\Delta U_{eff}$. $\Delta\sigma_{main}$ is the average stress drop inside this area.

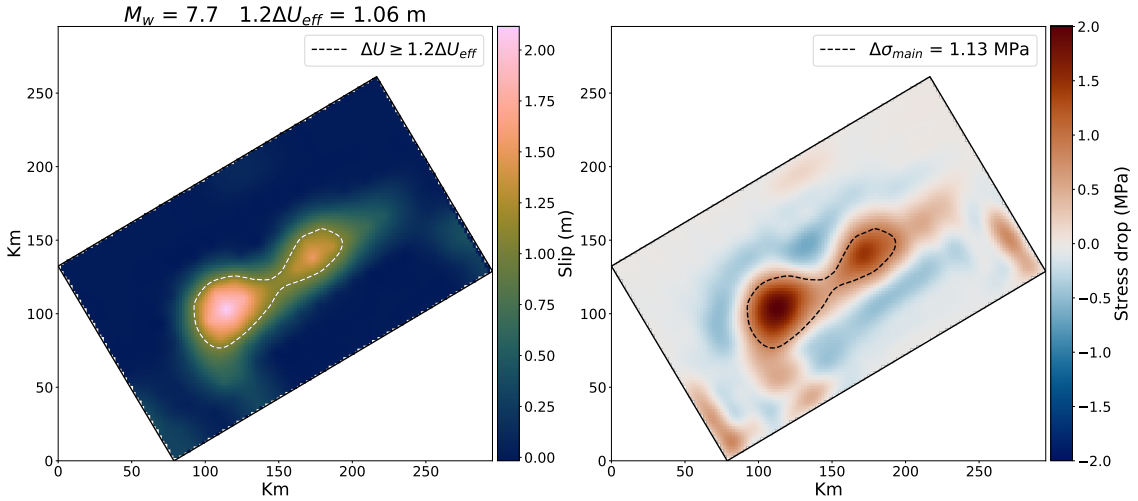

Figure 3.4 – On the left, slip distribution obtained by Béjar-Pizarro et al. (2010) for the 2003 Tocopilla earthquake M_w 7.7 using InSAR and GPS data. On the right, stress drop distribution inferred from the coseismic slip. Dashed line represents the area where the slip is greater than $1.2\Delta U_{eff}$. $\Delta\sigma_{main}$ is the average stress drop inside this area.

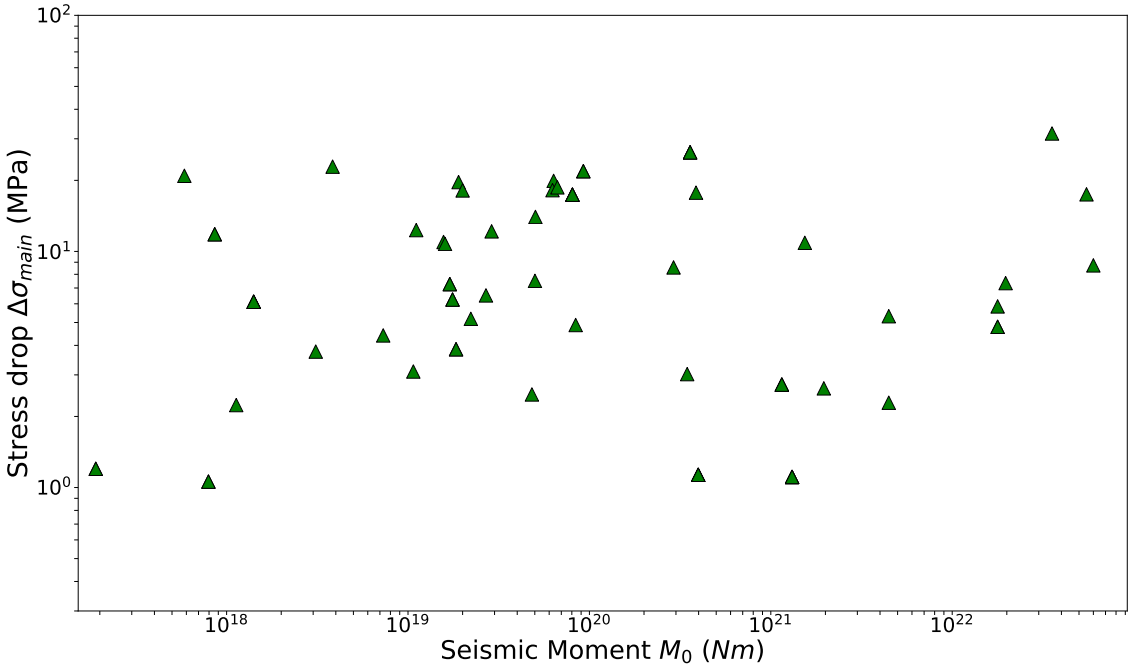

Figure 3.5 – $\Delta\sigma_{main}$, defined as the average stress drop in areas where slip is greater than 20 % of U_{eff}, is represented against the seismic moment. For earthquakes which have several slip models, and consequently several stress drop maps, final $\Delta\sigma_{main}$ is the mean of the $\Delta\sigma_{main}$ of each stress drop map.

imply that large earthquakes which are characterized by large slip patches and longer development phase do not produce higher local stress drop. A monotonic increase of the stress drop leading to a time exponent greater than 2 for the moment rate during the development is therefore very unlikely.

Our analysis however could benefit from a more accurate description of the development phase, if temporal criterion were used in addition to the current spatial constrain to isolate $\Delta\sigma_{main}$. As the development phase is extracted in time domain in the SCARDEC database, slip models with also a time history would be more suitable. Few of such slip models are present in our selection (a large number of them are inferred from geodetic data and do not constrain the time evolution of the rupture). Ideally, a large catalog as the one of Ye et al. (2016), but with a broader magnitude range and regional data to have more details on the rupture, would be extremely useful to make a more robust comparison with the development phase properties found in the SCARDEC catalog.

3.2 Source characteristics of a circular crack model with rupture velocity variability

3.2.1 Analytical slip solution and generation of a random temporal evolution of the rupture velocity

Seismological evidence does not support the simple view of a model with a monotonic increase of stress drop and/or rupture velocity when earthquakes of various sizes develop, and therefore favors the self-similarity as a robust average source property. As rapidly

introduced in Section 2.3.3, random variability of these parameters has instead some advantages that allow to add more realism into kinematic rupture models. Indeed, the observation of a constant average rupture velocity for all sizes of earthquakes does not exclude a high variability all along the rupture process, with for example local supershear (Bouchon and Vallée, 2003; Dunham and Archuleta, 2004) or very low (Meng et al., 2012; Kiser and Ishii, 2011) rupture velocities. This variability, which does not affect the global self-similarity, has also the potential to modify some transient moment rate evolution such as the development phase. Resulting STFs can be composed of several growing parts, instead of a monotonic growth from the initiation to the maximum moment rate. It can consequently reproduce a complexity often retrieved in SCARDEC STFs (see Section 2.2.1).

We introduce the analytical solution of the slip for the circular crack as follow:

$$u(r,t) = \frac{\Delta\sigma}{\mu}\sqrt{a^2(t) - r^2} \tag{3.2}$$

with the different parameters already defined in the previous sections. A rupture velocity variability can be included in the evolution of the crack radius at each time $a(t)$ with the following definition

$$a(t) = \int_0^t v_r(u)\,\mathrm{d}u. \tag{3.3}$$

In order to remain in a configuration where equation 3.2 is the solution of the slip, equation 3.3 requires that v_r depends only on time, or equivalently, on the radial extension. The solution of the slip in a case of an additional azimuthal variability is not as simple as the scalar form of equation 3.2 and is not introduced yet. We consider a stochastic one-dimensional brownian noise for the time evolution of the rupture velocity, modeled by a Wiener process, which we write as an iterative scheme:

$$\begin{cases} v_r(t+dt) = v_r(t) + \mathcal{N}(0, \Delta^2 dt) \\ v_r(0) = v_0. \end{cases} \tag{3.4}$$

$\mathcal{N}(0, \Delta^2 dt)$ is a normally distributed random variable with 0 mean and variance equal to the product between Δ, a free parameter controlling the amplitude of the variable, and the time interval dt. v_0 is an initial condition, here the rupture velocity at $t = 0$. At time $t+dt$, rupture velocity is a random value selected from a normal distribution with a mean equal to the rupture velocity at time t. At any time, rupture velocity is therefore influenced by its preceding value but is randomly higher or lower. Such an iterative approach is thought to be a good approximation at first order of the real rupture velocity evolution. Indeed, in a context of barriers and asperities models, complexities on fault create more or less favorable conditions for rupture propagation, implying changes in the rupture velocity values, but they likely cannot have a radical change in such short times.

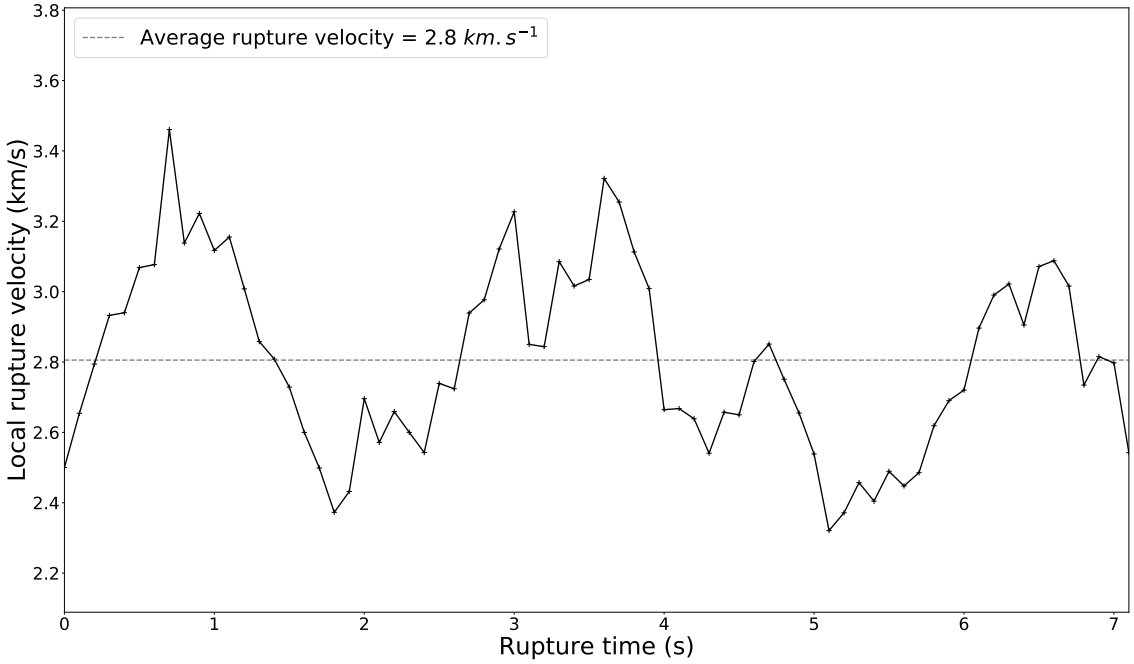

Figure 3.6 – Radial rupture velocity generated with equation 3.4. Crack rupture starts with an initial rupture velocity $v_0 = 2.5\,\mathrm{km.s^{-1}}$ and randomly evolves during the rupture process. The parameter Δ controlling the amplitude of the random values is here equal to $450\,\mathrm{m.s^{-3/2}}$. The average rupture velocity $\overline{v_r}$ is represented by the gray dotted line and is equal in this case to $2.8\,\mathrm{km.s^{-1}}$.

The initial value is $v_0 = 2.5\,\mathrm{km.s^{-1}}$ and the time interval $dt = 0.1\,\mathrm{s}$. We then apply the iterative scheme detailed above for a given value of Δ and generate random rupture velocity values as a function of rupture time, as illustrated in Figure 3.6. The rupture velocity value transiently increases and decreases around an average value $\overline{v_r}$. If the rupture time is long enough, $\overline{v_r}$ is close to v_0. As this rupture velocity profile is a function with no analytical primitives, the radius of the crack at each time is numerically computed with equation 3.3. In contrast with the propagation of a circular crack at constant rupture velocity, the increase of $a(t)$ is no longer linear but randomly varies as a consequence of equation 3.6. Such heterogeneous propagation is shown Figure 3.7 with the black dotted lines representing the position of the rupture front every 1 s. The radial distance between these lines for example exhibits the fast propagation between 3 s and 4 s induced by high transient rupture velocity values seen in Figure 3.6.

3.2.2 Kinematics of the modified crack model

In order to evaluate the slip evolution of this modified circular crack, the numerical computation of $a(t)$ is included into equation 3.2 which allows to compute the slip at every point on the fault and at every time. As depicted in Figure 3.7, we set a hypocenter in the middle of a $40 \times 40\,\mathrm{km}$ fault, and a rupture propagates following the evolution of $a(t)$ until reaching the fault bounds, i.e. at $T_m = 7.2\,\mathrm{s}$ after the rupture initiation. At this final stage, the radius of the crack is equivalent to the half-length of the fault. The final slip is exhibited in Figure 3.7 with stress drop $\Delta\sigma = 2\,\mathrm{MPa}$ and rigidity $\mu = 40\,\mathrm{GPa}$, and the maximum slip is around 1 m. With the slip distribution at each time of the rupture, we determine numerically the seismic moment $M(t)$ with the equation,

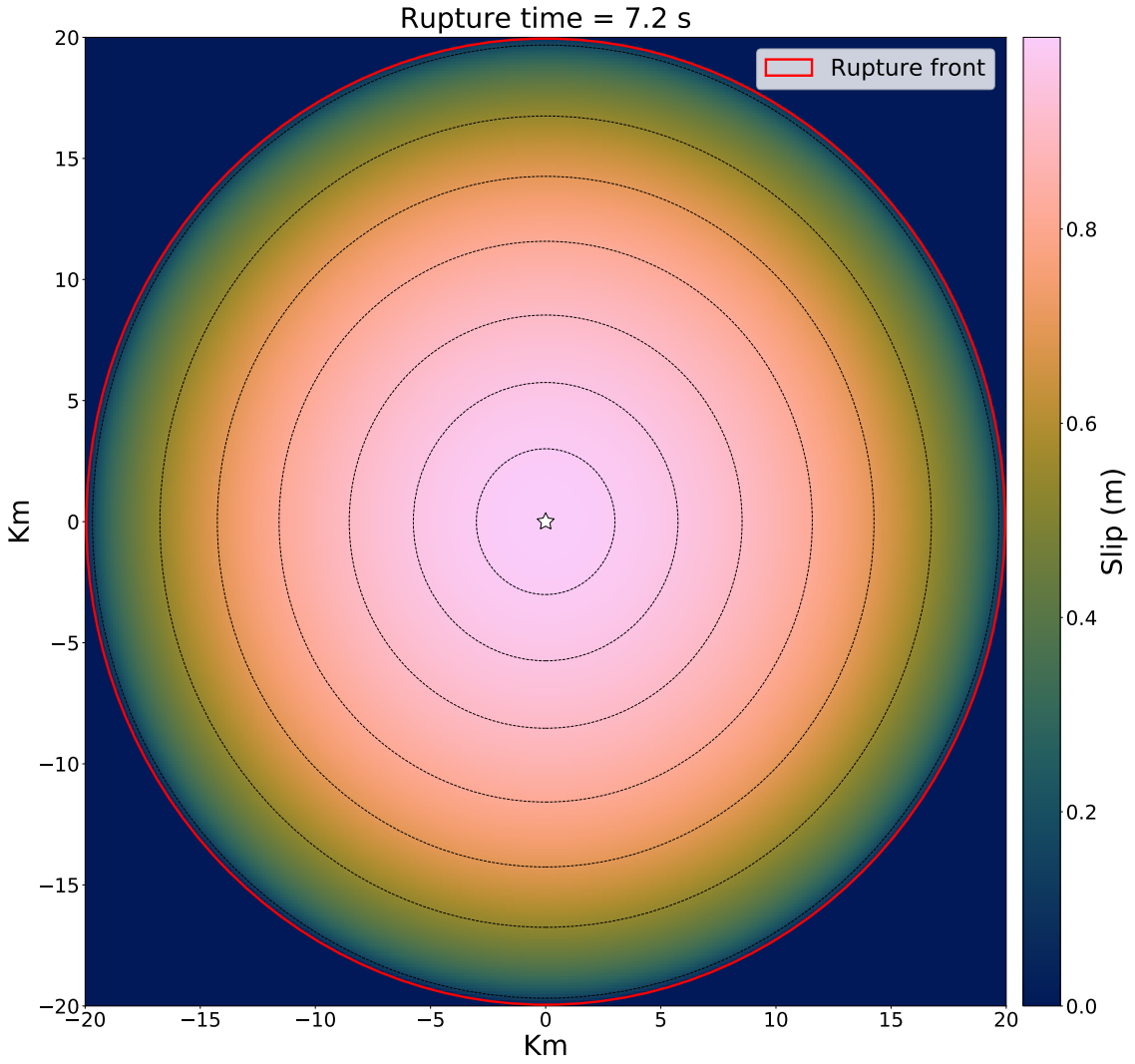

Figure 3.7 – Final slip of a crack-like rupture with random rupture velocity, using equation 3.2 with a stress drop $\Delta\sigma = 2\,\text{MPa}$ and rigidity $\mu = 40\,\text{GPa}$. Fault dimensions are $40 \times 40\,\text{km}$, and the rupture front in red propagates until reaching the fault bounds, i.e. $T_m = 7.2\,\text{s}$ after the rupture initiation. Black dotted lines are the position of the rupture front every second, and highlight the variable rupture velocity.

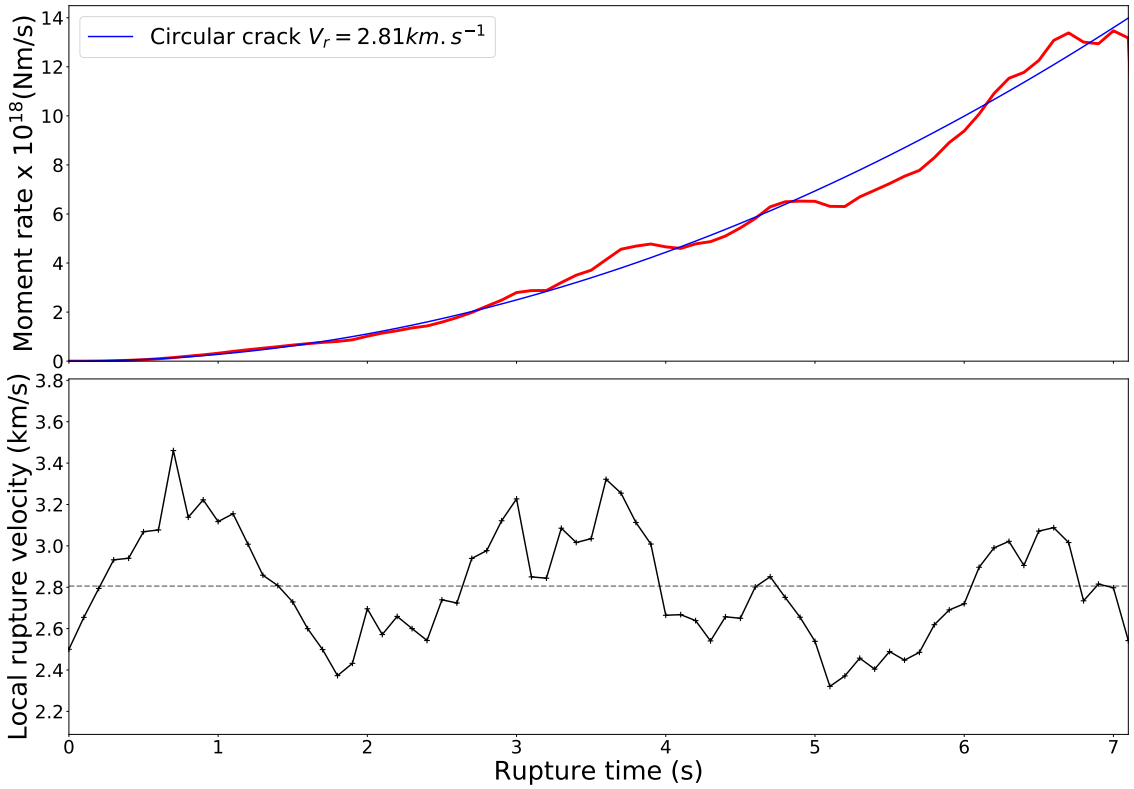

Figure 3.8 – Top: in red the evolution of the moment rate function during the propagation of a crack with random rupture velocity until the edges of the fault. The blue line is the evolution of the moment rate for a constant rupture velocity value equal to the average velocity value $\overline{v_r}$ of the random model. Botttom: same graph as the Figure 3.6 to observe the effect of the rupture velocity on the evolution of the moment rate.

$$M(t) \;=\; \mu \int_S u(r,t)\,\mathrm{d}S. \tag{3.5}$$

When including equation 3.2 into 3.5, we observe that μ disappears and has no effect on the value of $M(t)$. Such formulation implies that only Δ, $\Delta\sigma$ and v_0 are the critical parameters affecting the following results. We finally differentiate to obtain the temporal evolution of the moment rate $\dot{M}(t)$:

$$\dot{M}(t) \;=\; \frac{M(t+dt) - M(t)}{dt}. \tag{3.6}$$

The generated source time function shown in Figure 3.8 therefore grows until T_m when the rupture is stopped by the fault bounds, providing only the growing phase of the crack. The area under the STF represents the seismic moment released and is equal to $M(T_m) \;=\; 3.4 \times 10^{19}\,\mathrm{Nm}$. Figure 3.8 shows at the top and the bottom the evolution of the moment rate and the rupture velocity with time, respectively. The observation of these two graphs as a function of the rupture time clearly highlights the effect of an increase/decrease of the rupture velocity on the shape of the STF. Taking as reference a classical crack growing at a constant rupture velocity with value equal to $\overline{v_r}$, we observe a distinct STF for our current model. Among the different phases observed in the red

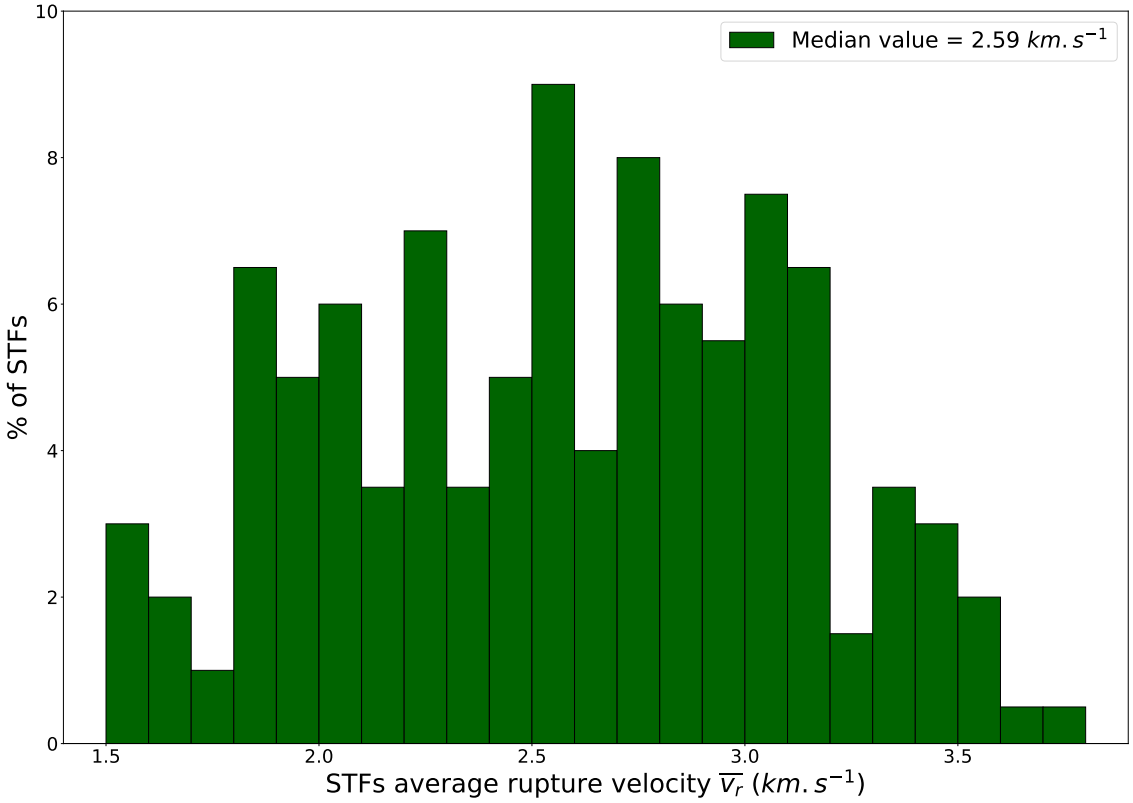

Figure 3.9 – Average rupture velocity distribution for a catalog of 200 synthetic STFs. The Δ value is here equal to $450\,\mathrm{m.s}^{-3/2}$ and explains the large range of $\overline{v_r}$ values. Since all STFs have as initial rupture velocity value $v_0 = 2.5\,\mathrm{km.s}^{-1}$, the median of this distribution tends also to v_0.

curve in Figure 3.8, we can distinguish three main behaviors. First, as the value of $\dot{M}(t)$ is notably controlled by the surface of the ring created between the position of rupture front between t and $t - dt$, a drastic decrease of the rupture velocity in the next time step involves a very low surface expansion leading to a lower value for $\dot{M}(t + dt)$. A second configuration is a slight decrease of the rupture velocity which still causes enough surface expansion to produce a small increase of the moment rate. The last behavior having a direct connection with the development phase of an earthquake is a transient increase of the rupture velocity. A significant example is the phase in the time window between 5.5 s and 6.5 s in Figure 3.8, where the normally distributed random variable $\mathcal{N}(0, \Delta^2 dt)$ is mostly positive such as rupture velocity evolves from around $2.3\,\mathrm{km.s}^{-1}$ to $3.1\,\mathrm{km.s}^{-1}$ one second later. This causes a rapid increase of the moment rate, which is more and more drastic late in the rupture process as a larger broken surface is involved.

3.2.3 Effect of rupture velocity variability on synthetic Source Time Functions

Variation of rupture velocity shows a significative effect and can produce STFs with development phases composed of several monotonic phases. In order to investigate if this modified crack model is able to reproduce our observations in Chapter 2, the procedure detailed above is applied to create a catalog of synthetic STFs. We generate catalogs of 200 synthetic STFs for each given couple of (Δ, $\Delta\sigma$) that we select in realistic ranges. For each catalog, Δ controls the random realization of rupture velocities while $\Delta\sigma$ is constant.

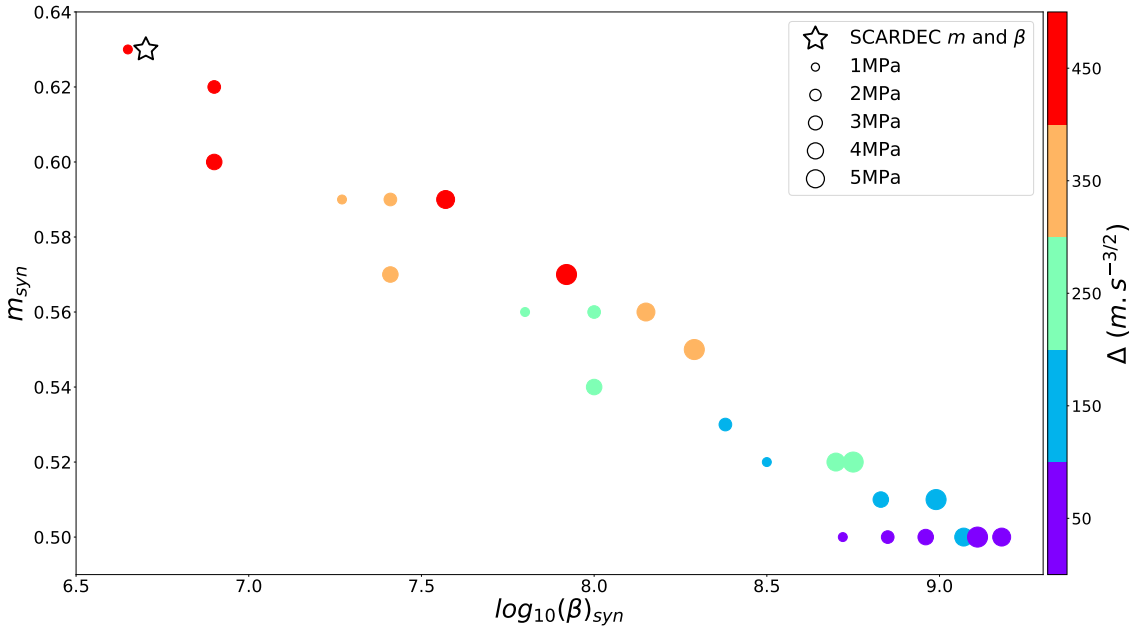

Figure 3.10 – m_{syn} and $\log(\beta)_{syn}$ coefficients extracted from the power laws relating moment acceleration and moment rate. The size of the points scales with $\Delta\sigma$, and the discrete colorbar indicates the Δ values. The star refers to the SCARDEC coefficients found in Chapter 2.

Each STF has an initial rupture velocity v_0, however the normal random process which follows implies that $\overline{v_r}$ is different for each event. As an example, Figure 3.9 represents the distribution of $\overline{v_r}$ for one of the catalogs with $\Delta = 450\,\mathrm{m.s^{-3/2}}$, with values ranging from around $1.5\,\mathrm{km.s^{-1}}$ to $3.8\,\mathrm{km.s^{-1}}$. Such approach therefore leads to a distribution with a classical median value roughly equal to v_0 and a dispersion in agreement with rupture velocities extracted from seismological observations (Somerville et al., 1999; McGuire et al., 2002; Chounet et al., 2017). The distinct rupture velocity value for each event combined with a regular fault dimension leads to a rupture front reaching the edges at different times, creating STF growth with different durations but a similar seismic moment.

Overall, 25 synthetic catalogs are created in order to explore various (Δ, $\Delta\sigma$) configurations. To do so, we define a sequence of 5 Δ values from 50 to $450\,\mathrm{m.s^{-3/2}}$ for a given value of $\Delta\sigma$ and we compute 200 synthetic STFs for each case. Such procedure is applied for 5 different $\Delta\sigma$ ranging from 1 MPa to 5 MPa. Once each catalog is created, we extract development phases with the method detailed in Section 2.2.1, apart from the lower limit at $0.07F_m$ which is now not taken into account. Moment acceleration values are then computed according to the procedure in Section 2.2.2. These values are finally plotted against moment rate values and a fit is achieved following the power law $\ddot{M}_d = \beta_{syn}\dot{M}_d^{m_{syn}}$ so that 25 (m_{syn}, $\log(\beta)_{syn}$) couples are directly comparable with m and $\log(\beta)$ found from SCARDEC observations. Figure 3.10 represents the (m_{syn},$\log(\beta)_{syn}$) couples with the size of points proportionnal to $\Delta\sigma$ and the color associated to Δ. The star location referring to the SCARDEC coefficients m and $\log(\beta)$ is clearly not compatible with most of the cases. For example, the 5 catalogs with the lowest $\Delta = 50\,\mathrm{m.s^{-3/2}}$ value (in purple Figure 3.10) share an identical $m_{syn} = 0.5$, far from $m = 0.63$. As a reminder, $m = 0.5$ refers to self-similarity as $\dot{M}_d(t) = \alpha t^{n_d}$ and $n_d = \frac{1}{1-m} = 2$. Figure 3.11 shows one of

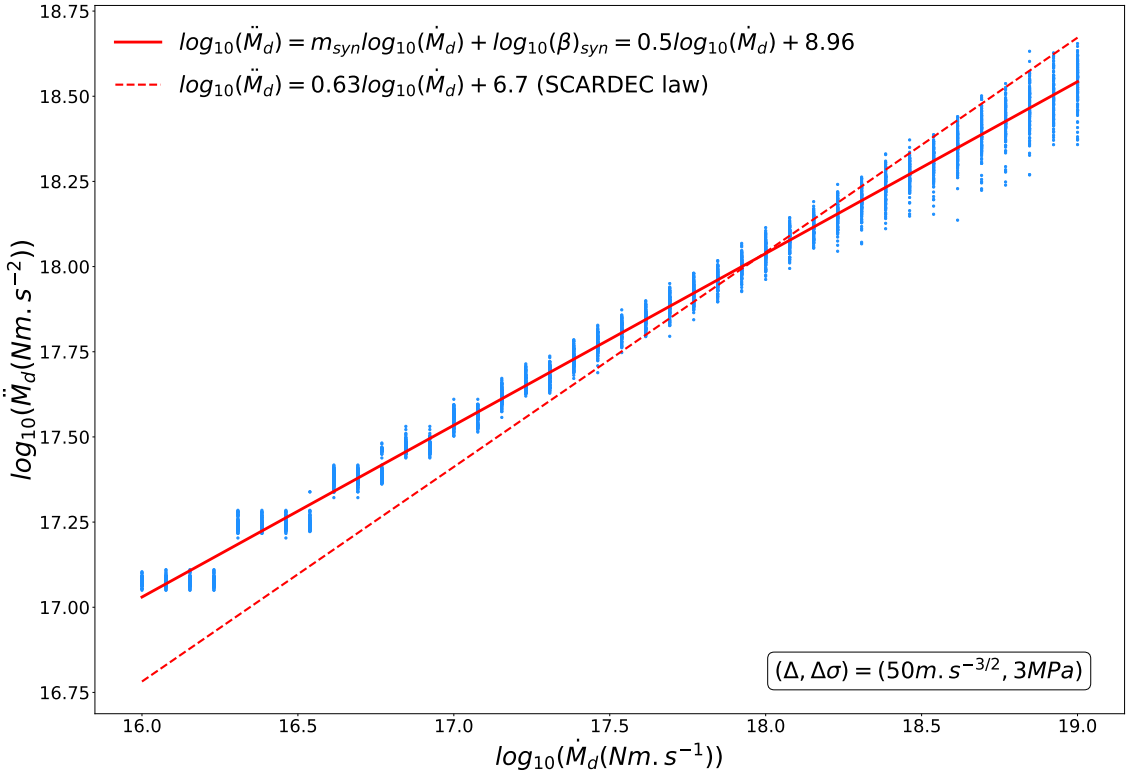

Figure 3.11 – Moment acceleration $\ddot{M}_d$ as a function of moment rate $\dot{M}_d$ (log-log scale). Each blue dot corresponds to an individual $(\ddot{M}_d)_{ij}$ value used to compute the linear fit. Red line is the best linear fit explaining the synthetic data. Red dotted line is the linear fit for the SCARDEC observations. The value of the $(\Delta, \Delta\sigma)$ couple is indicated in the bottom right corner.

these examples with the catalog with ($\Delta = 50\,\mathrm{m.s}^{-3/2}$, $\Delta\sigma = 3\,\mathrm{MPa}$). According to this observation, such a very low rupture velocity variability is not sufficient to move the STFs shape away from the self similar behavior. Synthetic STFs roughly follow equation 2.6, which is also confirmed by the distinct increase of $\log(\beta)_{syn}$ with $\Delta\sigma$ in Figure 3.10. Indeed, when comparing equations 2.6 and 2.9, we observe that $\Delta\sigma$ correlates with β for a given m and rupture velocity V_r.

The effect of the rupture velocity variability on m_{syn} becomes apparent when Δ progressively increases. As shown in Figure 3.10, orange and red points have systematically a higher m_{syn} value. This effect is even more pronounced when high Δ are combined with low $\Delta\sigma$. As depicted in Figure 3.10, points with large size (i.e. large $\Delta\sigma$) are systematically associated with too large $\log(\beta)_{syn}$. Such trend is understood to originate from the correlation between $\Delta\sigma$ and $\log(\beta)_{syn}$. For STFs with large $\Delta\sigma$, they strongly develop, hence are characterized by moment accelerations too high to fit the SCARDEC observations. In summary, Figure 3.10 essentially reflects that the combination of high rupture velocity variability and low stress drop leads to approach the m and $\log(\beta)$ values found in the SCARDEC analysis.

3.2.4 Discussion and conclusion

On the basis of this analysis, the optimal couple reproducing well our observations is (Δ_{opt}, $\Delta\sigma_{opt}$) with $\Delta_{opt} = 450\,\mathrm{m.s}^{-3/2}$ and $\Delta\sigma_{opt}$ =1-3 MPa. Though the first optimal parameter is well constrained, a value of $\Delta\sigma_{opt}$ between 1 MPa and 3 MPa gives consistent results. Figure 3.12 shows this optimal configuration where $m_{syn} \simeq m$ and $\log(\beta)_{syn} \simeq \log(\beta)$. Such accordance with the observations is particularly interesting for moment acceleration at high moment rate values, that can be reproduced only with a very high rupture variability. Finally, despite self-similar macroscopic properties as (1) constant stress drop, (2) analytical slip formulation of a circular crack, (3) rupture velocity distributed around an average value, this simple model is able to explain the average behavior of the development phase which is itself not self-similar. These results therefore imply that rupture velocity variability is a critical kinematic parameter. If we refer to Figure 3.8 and to our method for extracting moment acceleration, at least three reasons lead us to believe that the behavior of the development phase essentially results from transient increase appearing in the random evolution of the rupture velocity.

First, development phase is by definition composed of at least one monotonic growing section, but does not contain decreasing sections. These latter sections, due to transient drastic decrease of rupture velocity, are therefore not taken into account when computing moment accelerations. Secondly, development phases seen individually show also a complex moment rate evolution, with slow and fast increases. Since our method computes moment accelerations at given moment rates, a fast moment rate increase (associated to a rupture velocity increase in this model) is more likely to intersect a lot a given moment rates, in contrast with slow moment rate increase which is statistically much less sampled. These two latter arguments clearly show that according to our definition of the development phase and to the method we implemented, it favors the computation of the moment accelerations in rupture velocity increase phases, particularly if this increase is substantial. The third reason that makes the rupture velocity variation a strong candidate for explaining our observations is the correlation between rupture velocity and slip velocity explicited in equation 2.2. As a result of this relation, the rupture velocity variability also leads to modify the slip velocity form of the crack. An increase of the rupture velocity means a larger ruptured surface together with a higher slip velocity value at each point, especially just behind the rupture front, generating steeper moment accelerations compared to a crack with constant rupture velocity.

In summary, we show here that even a simple model of a modified crack with macroscopic self-similar properties is able to generate an evolution of the moment rate which is itself not self-similar during the development phase. Strong rupture velocity variability, that we express as $\Delta_{opt} = 450\,\mathrm{m.s}^{-3/2}$, combined with a value of $\Delta\sigma_{opt}$ = 1-3 MPa is sufficient to reproduce our observations. It also reproduces at first order the spectrum of rupture velocities found with the SCARDEC catalog (Chounet et al., 2017). Of course, such very simplified model presents some limitations, the first of them being an unphysical simultaneous velocity changes at each point on the rupture front. As we expect that rupture velocity changes are only in specific directions, Δ_{opt} can roughly give a lower bound value of the intra-variability of earthquakes rupture velocity. The circular slip

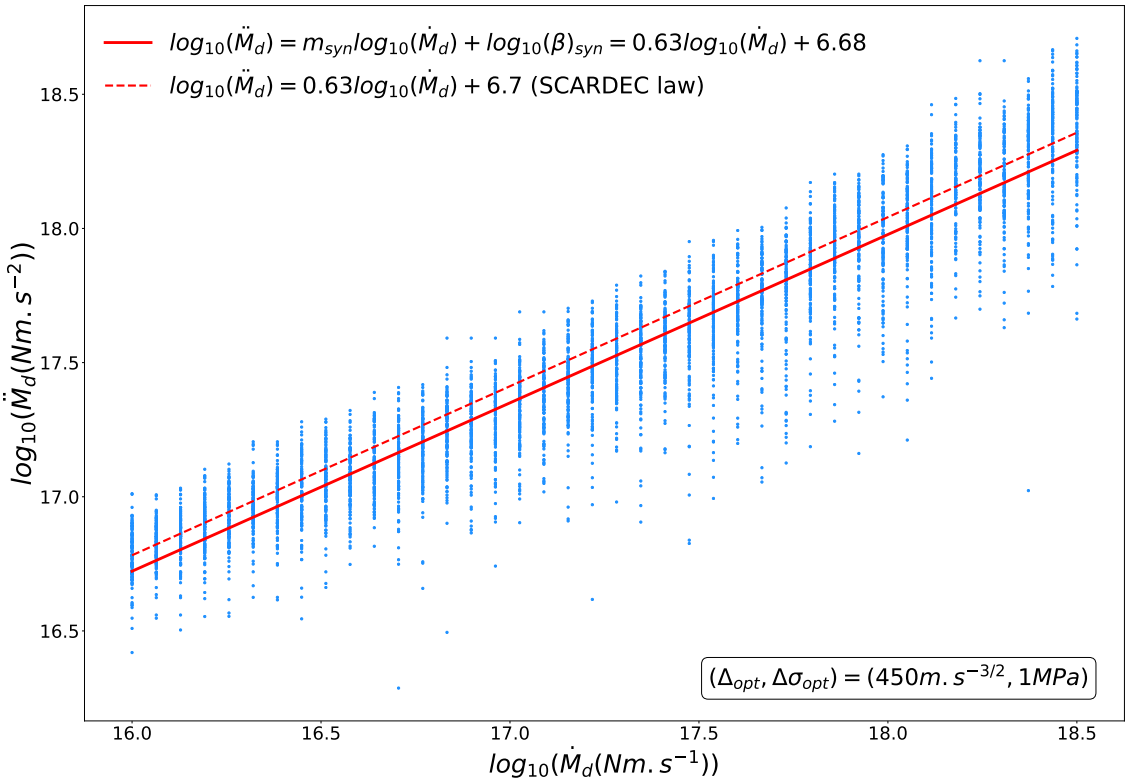

Figure 3.12 – Moment acceleration $\ddot{M}_d$ as a function of moment rate $\dot{M}_d$ (log-log scale) for the optimal parameters (Δ_{opt}, $\Delta\sigma_{opt}$). Each blue dot corresponds to an individual $(\ddot{M}_d)_{ij}$ value used to compute the linear fit. Red line is the best linear fit explaining the synthetic data. Red dotted line is the linear fit for the SCARDEC observations. This Δ_{opt}, $\Delta\sigma_{opt}$ couple for a circular crack model with variable rupture velocity agrees very well with the observations.

distribution is also not compatible with analysis of spatial complexity from finite-fault source inversions (Mai and Beroza, 2002), and heterogeneous model taking into account the complex rupture propagation is developed in Section 3.3.

3.3 Rupture properties of a kinematic fractal k^{-2} source model

3.3.1 Ruiz Integral Kinematic (RIK) model setup

Numerous kinematic source models have been developed in order to retrieve the main features of the seismic displacement spectrum. In particular, the challenging issue is to reproduce both the low and high frequency contents, with the latter showing a spectrum fallof proportionnal to w^{-2} above the corner frequency w_c. The so-called composite models successfully model such characteristics based on the description of an earthquake as a cascade of small events with different sizes (Frankel, 1991; Zeng et al., 1994; Bernard et al., 1996; Gallovič and Brokešová, 2007). As detailed by Andrews (1980), the w^{-2} spectral decay at high frequency can be generated by final slip spectrum with k^{-2} decay at high wavenumbers. This specific signature of the final slip spectrum constrains the relation connecting the number of sub-events with their size so that the number-size distribution of sub-events is fractal, with the fractal dimension $D = 2$ (see Appendix of Ruiz et al. (2011) for the complete development).

We take advantage of the *Ruiz Integral Kinematic (RIK)* model developed by Ruiz et al. (2011) to investigate the role of the kinematic parameters during the development phase. The analysis has been enabled by the open source code made by Gallovič (2016) and available in the webpage https://github.com/fgallovic/RIKsrf. Due to the foregoing reasons, the *RIK* model generates a fractal number-size distribution of circular sub-events with random locations on a fault plane, producing slip heterogeneity including overlaps between sub-events of various sizes. Each sub-event has a radius $R_n = W/n$ with W the width of the fault and n an integer value. In order to respect a fractal distribution, the number of sub-events at step n is equal to $2n-1$. The total number of sub-events, N, is defined as follows:

$$N = \sum_{n=n_{min}}^{n_{max}} (2n-1), \tag{3.7}$$

in which n_{min} and n_{max} are the largest and smallest sub-events numbers respectively. Each sub-event has a slip function Δu following the analytical slip solution of a circular crack:

$$\Delta u(r) = C\sqrt{R_n^2 - r^2} \tag{3.8}$$

with r the distance from the center of the sub-event. C is a constant value that is adapted to reach the target seismic moment. Figure 3.13 shows an example of random circular sub-events distribution with slip following the crack solution for a target value of $M_0 = 4.8\times10^{20}$ Nm. The representation with the z-axis depicts the heterogeneous slip values due to the overlaps of sub-events and the crack-like slip formulation, while the projection in the z direction emphasizes the size-number fractal distribution of the sub-events. Equation 3.8 fundamentally differs from equation 3.2 as it only gives a time-independent slip (final slip). As a consequence, equation 3.8 is not used to infer the slip velocity function. Instead, a simple boxcar function is assigned for each sub-event with a rise-time $\tau(R_n)$ linearly increasing with R_n such as:

$$\tau(R_n) = \begin{cases} \dfrac{aL_0}{V_r}, & \text{if } 2R_n > L_0 \\ \dfrac{a(2R_n)}{V_r}, & \text{if } 2R_n < L_0 \end{cases} \tag{3.9}$$

where a is a constant to define, L_0 the maximum pulse width and v_r the rupture velocity. L_0 is the macroscopic maximum pulse width, that we define larger than $2R_{n_{min}}$ to ensure that $\tau(R_n)$ grows with sizes of the sub-events.

The *RIK* model also aims at reproducing rupture directivity at all scales. In terms of rupture initiation, points on a fault inside a sub-event with a size larger than L_0 starts to slip upon the arrival of the macroscopic rupture front. However, since in our case $R_n < L_0$, a nucleation point inside the sub-event is randomly selected, and an internal rupture front propagates when the random point is reached by the macroscopic rupture front.

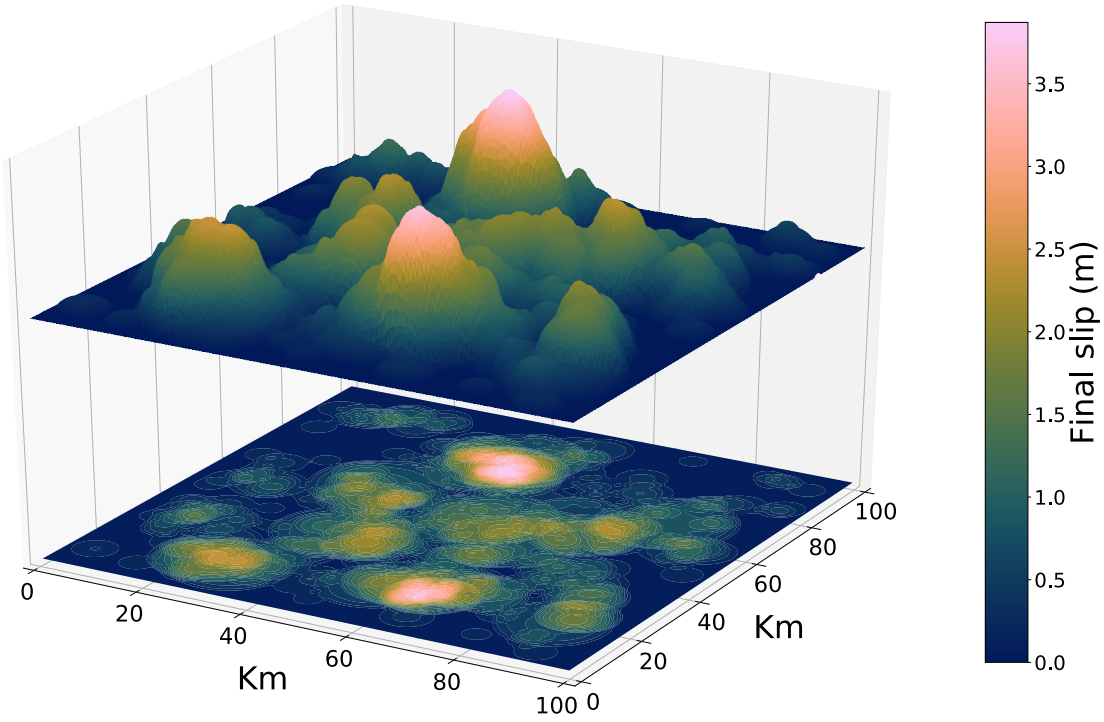

Figure 3.13 – Example of random circular sub-events distribution following a fractal size-number distribution with a fractal dimension $D = 2$ for a target value of $M_0 = 4.8 \times 10^{20}$ Nm. The spatial evolution of the slip following the crack solution along with sub-event overlaps produce heterogeneous slip values.

3.3.2 Fault parametrization and global source properties

The *RIK* model has the great advantage of reproducing a realistic rupture process with a direct access to kinematic source properties. As an example, the slip velocity history at each grid point of the fault, combined with the rupture front position at every time enables us to directly compute the source time function. However, the model has to be correctly parametrized in order to retrieve consistent global source properties, before analyzing in detail the STF characteristics. In the next paragraph, input parameters required by the *RIK* model will be enhanced in **bold**.

The parametrization starts by defining the size of the fault where earthquakes are generated. Since the goal of this analysis is to repeat the method we applied in Chapter 2, a relatively large fault surface is necessary to produce an earthquake with a STF reaching high moment rates values, i.e. more than 10^{19} Nm.s^{-1} for the peak moment rate. Based on this consideration, we first use the study of Mai and Thingbaijam (2014) in which an empirical relation relating M_0 and effective source dimensions is found with finite fault models from the *SRCMOD* database. For $M_0 = 10^{21}$ Nm, we roughly expect a fault surface of 10000 km^2, that we hereafter arrange to have a fault dimension of $\mathbf{S = 100 \times 100\,km}$. In a second step, the value of M_0 is refined because it has to accurately follow the self-similar equation extracted from the SCARDEC catalog by Chounet and Vallée (2018):

$$T = M_0^{0.31} \times 10^{-4.84}, \tag{3.10}$$

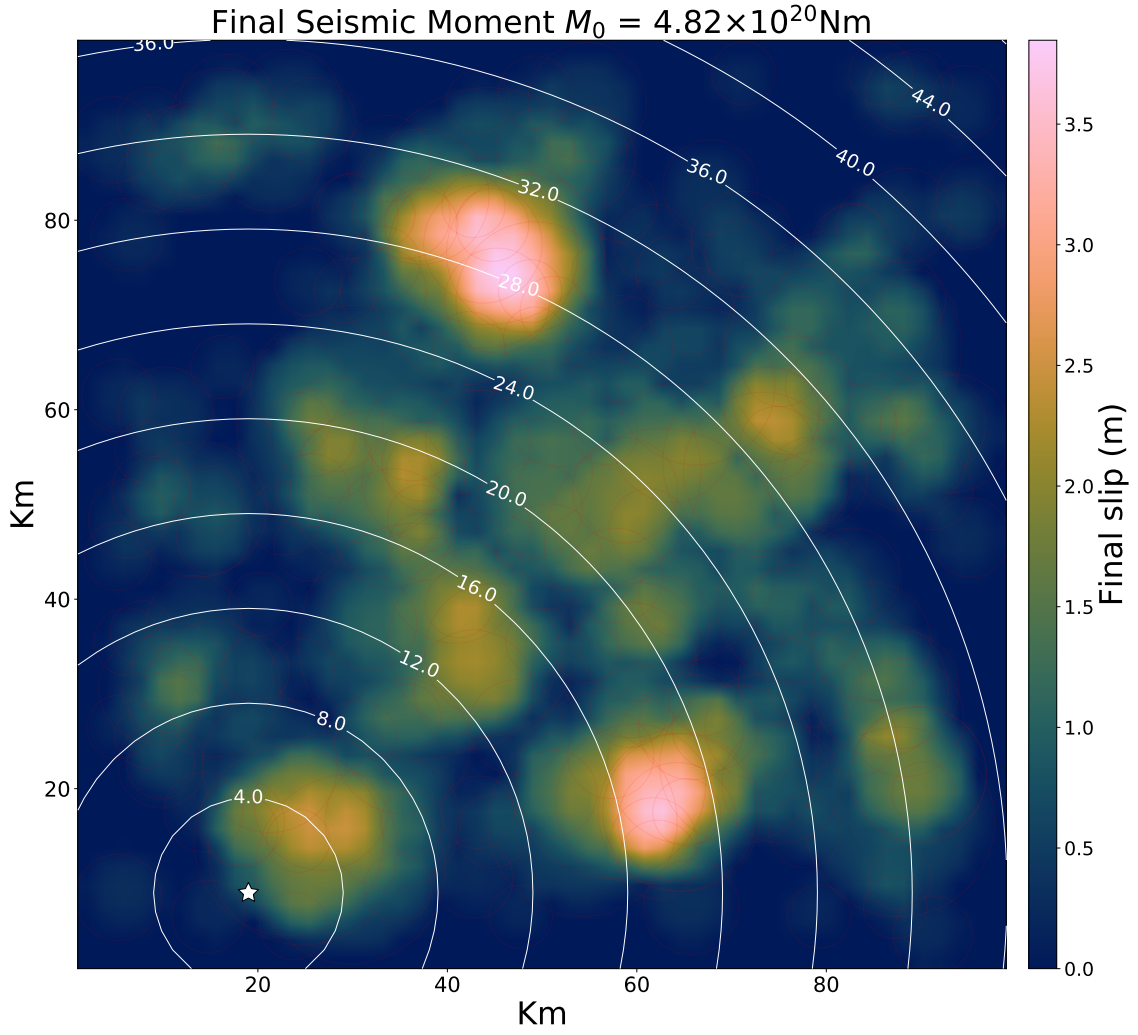

Figure 3.14 – Slip distribution of an earthquake with $M_0 = 4.82 \times 10^{20}$ Nm. The hypocenter location (white star) is randomly selected among the grid points. Red circles represent all the sub-events and highlight the numerous overlaps. White circles locate the macroscopic rupture front (propagating at $2.5\,\mathrm{km.s^{-1}}$) every $4\,\mathrm{s}$.

with T the rupture duration. To do so, we generate earthquakes of seismic moment of 1Nm with random hypocenter locations over the fault plane. Kinematic ruptures propagating at a constant rupture velocity $\mathbf{v_r = 2.5\,km.s^{-1}}$ are computed and their durations are estimated with the STFs in the same manner as Chounet and Vallée (2018) in order to obtain a mean rupture duration T, then allowing to infer the target $\mathbf{M_0 = 4.82 \times 10^{20}\,Nm}$ with equation 3.10. Such approach is followed for two reasons: (1) as M_0 is reached by adapting the constant value C in equation 3.2, there is a simple linear proportionnality between M_0 and Δu. (2) for a given value of a, rise-time values are fixed for sub-events, meaning that slip velocity is also linearly proportionnal to Δu. The few largest sub-events have radius of $\mathbf{R_{n_{min}} = 12.5\,km}$ while smallest sub-events are many with a radius of $\mathbf{R_{n_{max}} = 3.33\,km}$. We avoid larger sub-events to generate complex rupture propagation implying STFs with several monotonic phases, as well as smaller ones to prevent small scales features not represented in the SCARDEC STFs. The slip pulse width is setup to $\mathbf{L_0 = 25\,km}$, i.e. the diameter of the largest patch. The coefficient $\mathbf{a}$ controlling the duration of $\tau(R_n)$ is adjusted in the following.

We show an example of an earthquake in Figure 3.14 with the source parameters previously described. Maximum slip is slightly below 4 m and fits with the scaling law of Mai and Thingbaijam (2014). Red circles are the sub-events edges and often overlap each other. This superposition leads to sum different slip velocity functions, i.e. boxcar functions with durations $\tau(R_n)$, and create realistic cumulative slip velocity functions as shown in Figure 3.15 for a given value of $a = 0.4$. For sake of clarity, the temporal evolution of cumulative slip velocity functions is represented on a grid with point interval of 10 km, while the regular grid which is used to compute the rupture process has point interval of 2 km. The shape of these functions is surprisingly in very good agreement with the analytical crack model solution (Yoffe, 1951), as well as with other kinematic (Tinti et al., 2005) and experimental studies (Ohnaka and Yamashita, 1989). They reach their maximum value at the arrival of the rupture front, which is a singular point in the analytical formulation, before rapidly decreasing during $\tau(R_n)$.

As shown in Figure 3.14 at macroscopic scale, this event is mainly unilateral since the hypocenter is located at the bottom left of the fault. It also seems to have a very smooth rupture propagation due to the constant rupture velocity v_r. However, the large pulse width $L_0 = 2R_{n_{min}}$ causes a systematic random triggering from a nucleation point inside each sub-event. Therefore, the rupture process is controlled by the internal rupture front, which implies that the rupture expanding at v_r is more or less bilateral depending on the stochastic location of the nucleation point. This heterogeneous rupture front propagation is clear in Figure 3.16 where snapshots of the slip velocity values are represented at two different times. The triggering of the slip velocity is beyond the macroscopic rupture front, and the stochastic nucleation point location for each sub-event results in a more complex rupture propagation.

A suitable parametrization in terms of fault dimension, final seismic moment and source duration enables us to reproduce global source properties and consistent kinematic rupture scenario. In particular, the realistic shape of cumulative slip velocity functions combined with a heterogeneous rupture propagation provides an opportunity to produce robust synthetic STFs.

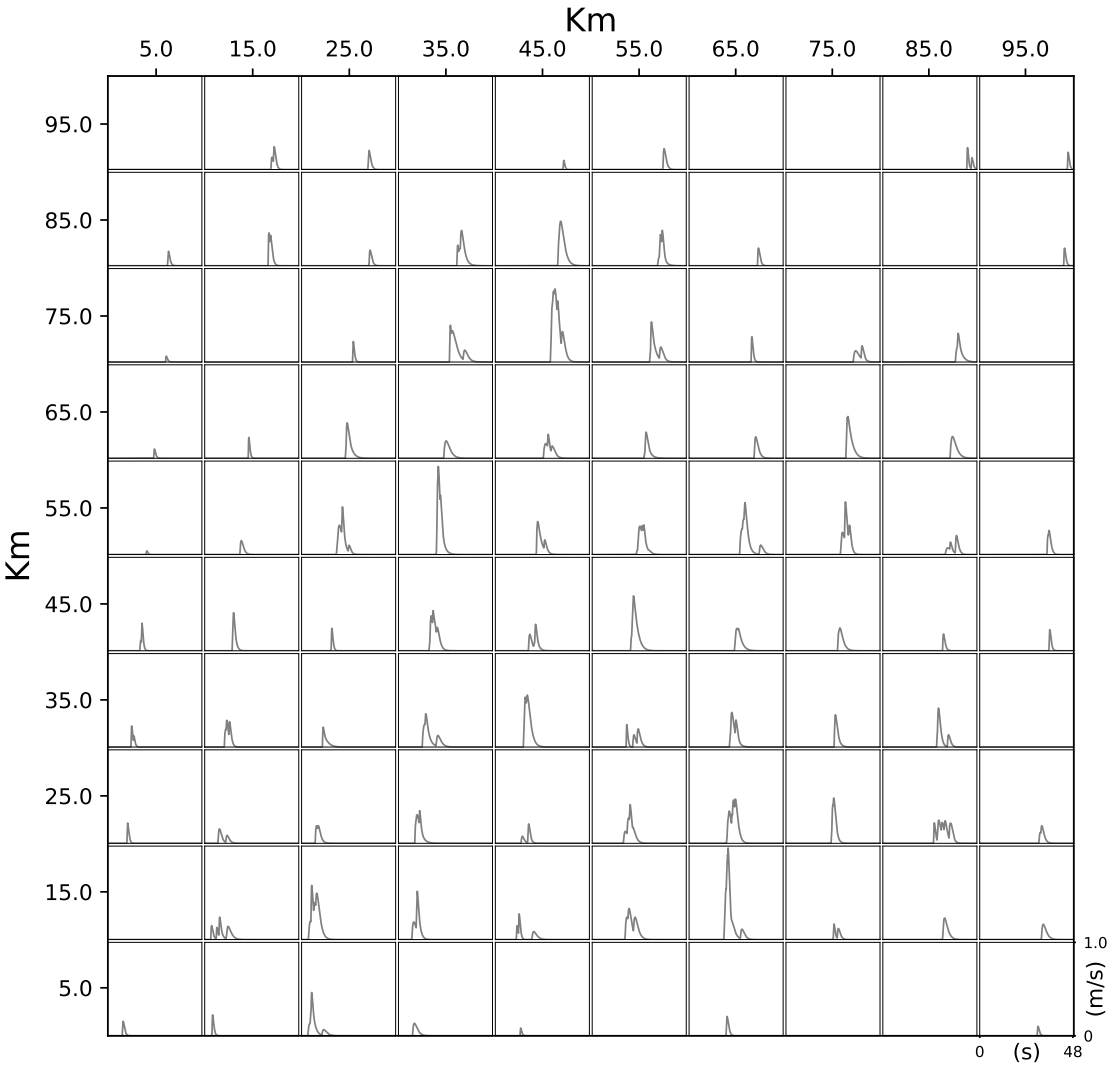

Figure 3.15 – Temporal evolution of cumulative slip velocity functions on a grid with point interval of $10\,\text{km}$ with $a = 0.4$. Most of these functions are characterized by a maximum value at the arrival of the rupture front before a rapid decrease during $\tau(R_n)$. They show a high similarity with the analytical slip velocity formulation of Yoffe (1951).

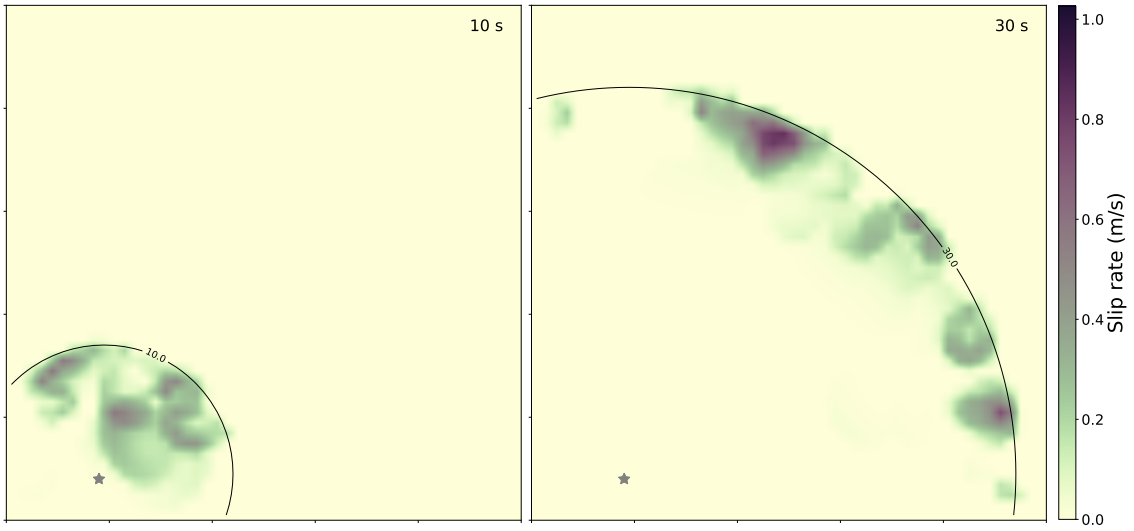

Figure 3.16 – Snapshots of the slip velocity together with the position of the macroscopic rupture front (black line) in two time steps (10 s and 30 s) for $a = 0.4$. The grey star is the location of the hypocenter. The stochastic rupture triggering from a nucleation point inside each sub-event creates an internal rupture front which is not coherent with the macroscopic rupture front.

3.3.3 Rise-time evolution and its effect on synthetic Source Time Functions

As the rise-time $\tau(R_n)$ is influenced by the a value, the *RIK* model has the ability to approach the two main rupture modes: crack-like and pulse-like ruptures. According to equation 3.9, a is the slope of the linear law relating τ to R_n, and hence has an effect on its the absolute value. It means that for the same fractal size-number distribution of sub-events, a low a value results in a low duration τ of the boxcar function for each R_n. For example, Figure 3.16 clearly exhibits a self-healing process since positive slip velocity values extend on a small fraction of the area behind the rupture front, as a consequence of the low value of $a = 0.4$. The rupture mode has significant impact on the shape of the slip velocity functions which in turn affect the ground motion (Galetzka et al., 2015). We therefore expect to see different STFs if the a value is modified. Figure 3.17 represents 5 STFs generated by simulations with the slip distribution and rupture propagation of Figure 3.14, and a different a value in each case. The earthquakes start at the same hypocenter on the same fault, implying that the STF durations are longer when a value increases (i.e. $\tau(R_n)$ increases), as confirmed by the longest STF in blue for $a = 1$. Apart from its effect the on rupture duration, a has also a critical impact on the moment rate evolution, and hence on the moment acceleration. For instance, monotonic growing phases of the five STFs in Figure 3.17 are "fan-shaped" such as at a given time the moment rate value is inversely dependent on a. Such trend is caused by the faster release of slip for low a values. Indeed, for each sub-event, the same amount of slip has to be released regardless of the a value, meaning that the boxcar functions have to be more impulsive and shorter for low a values. The cumulative slip velocity functions are consequently also more impulsive and shorter on a narrow zone behind the rupture front, resulting in rapid increase of the moment rate and steep moment accelerations for the purple and red STFs in Figure 3.17.

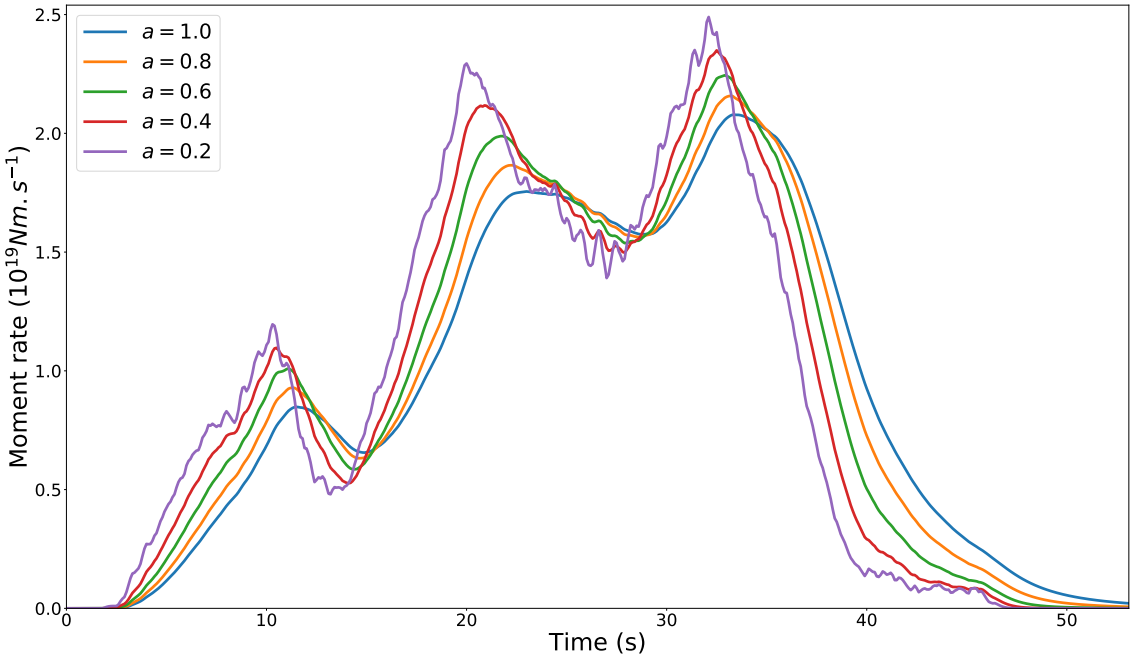

Figure 3.17 – STFs computed with the RIK model from the slip distribution and rupture propagation shown in Figure 3.14. Each STF is generated with different rise-time $\tau(R_n)$ values controlled by the parameter a. Following equation 3.9, $\tau(R_n)$ is proportionnal to a, implying a longer STF duration when a increases.

In order to quantify the effect of rise-time evolution on moment acceleration values as a function of moment rates during the development phase, we generate a catalog of 200 synthetic STFs for each a value prescribed in Figure 3.17, with the input parameters enhanced in bold in Section 3.3.2. The diversity of the rupture process is reproduced by randomly selecting a hypocentral location on the grid point of the fault for each event. For a square grid with constant point interval, ruptures start statistically often far from the fault center which favors the predominance of unilateral ruptures at macroscopic scale, consistent with observational results (McGuire et al., 2002). For each catalog, we verify that global source properties are reproduced, in particular the self-similar relations connecting the source duration T and the maximum moment rate F_m with the seismic moment M_0. Figure 3.18 confirms the self-similar behavior of these two global parameters for one of the catalogs ($a = 0.4$). According to equations 3.10 for T and the one in Chounet and Vallée (2018) for F_m, SCARDEC observations provide median values of 37.3 s and 2.28×10^{19} Nm.s^{-1} respectively, which are equivalent to the ones obtained by our synthetic catalog in Figure 3.18. The four other catalogs show equivalent self-similar behaviors.

After the creation of a catalog, we extract development phases with the same method detailed in Section 2.2.1, apart from the lower limit at $0.07F_m$ which is not taken into account. Moment acceleration values are then computed according to the procedure in Section 2.2.2. These values are finally plotted against moment rate values and a fit is achieved following the power law $\ddot{M}_d = \beta \dot{M}_d^m$ so that 5 (m, $\log(\beta)$) couples are created. We represent the five fits in Figure 3.19, together with the law found from SCARDEC catalog. For sake of clarity, we do not show the moment acceleration values used to compute each fit. As expected, for a given moment rate value, the average moment acceleration is systematically anticorrelated with the a value. However, only the synthetic catalog with

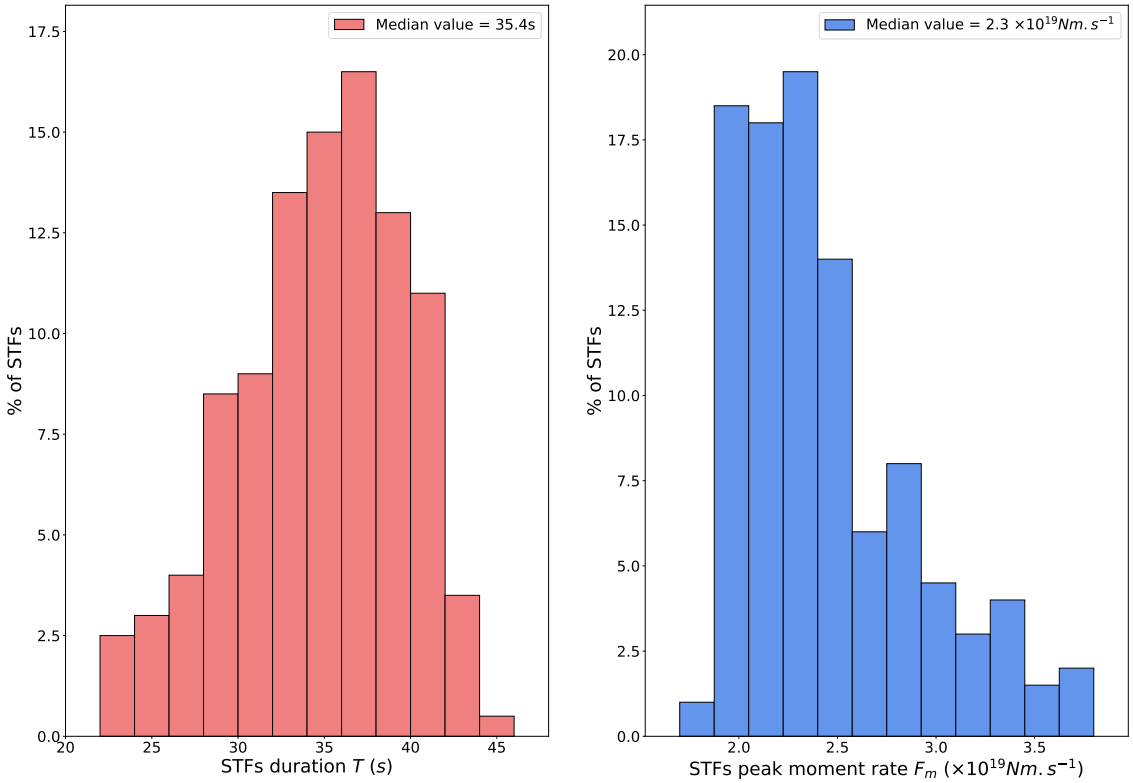

Figure 3.18 – Histogram of STFs duration T and peak moment rate F_m for 200 synthetic STFs with $a = 0.4$ for a seismic moment $M_0 = 4.82 \times 10^{20}$ Nm. The two source parameters correctly follow the self-similar dependence as a function of M_0 of the SCARDEC catalog (Chounet and Vallée, 2018), since the median values are very closed to the ones obtained with the SCARDEC STFs.

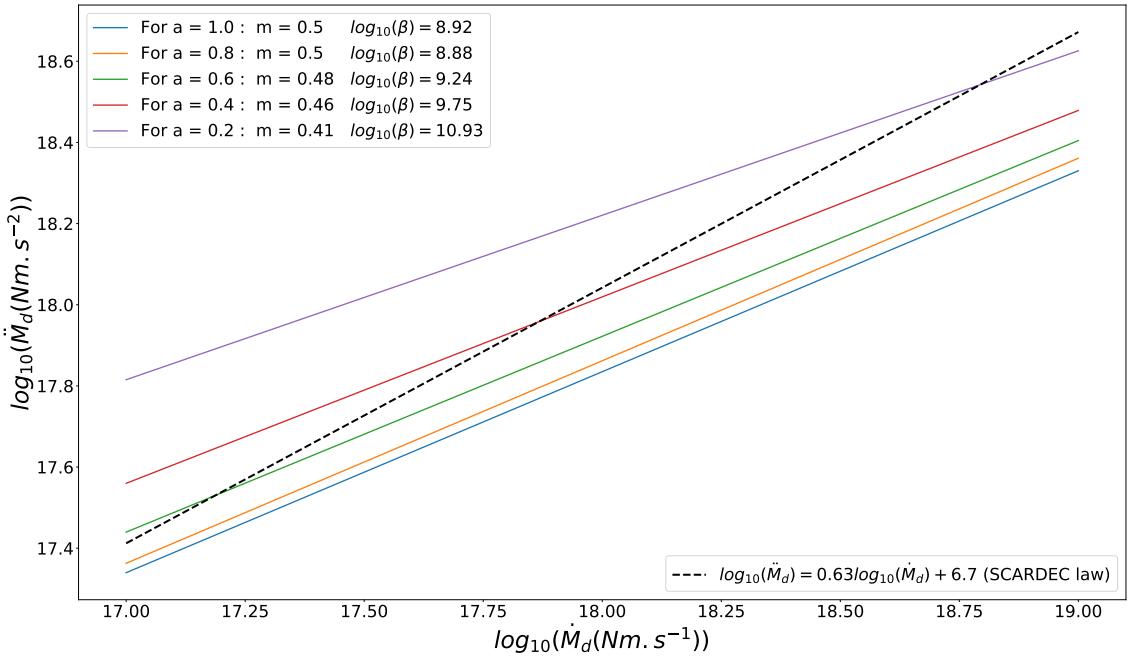

Figure 3.19 – Moment acceleration $\ddot{M}_d$ as a function of moment rate $\dot{M}_d$ (log-log scale) for the 5 five synthetic STFs catalogs with different rise-time $\tau(R_n)$ evolutions. Each line is the best linear fit explaining the synthetic data. Color of lines refers to different a values as in Figure 3.17. For sake of clarity, moment acceleration values used to compute each fit are not shown. Black dotted line is the linear fit for the SCARDEC observations.

$a = 0.2$ reaches the average moment acceleration of the SCARDEC catalog for the highest moment rate values whereas for the lowest moment rates, only the synthetic catalogs with high a values obtain average moment acceleration comparable with SCARDEC observations. As a consequence, all catalogs have m values lower than the observed one (black dotted line in Figure 3.19). These results show that, with a constant rupture velocity, despite physical cumulative slip velocity shapes (Figure 3.15), the RIK model generates development phases with time exponent close to, or even below (for low a values), the self-similar value of 0.5. Small a values generate high acceleration very early in the rupture process, resulting in a lower exponent.

3.3.4 Correlation between slip velocity and rupture velocity

In the former section, a constant rupture velocity throughout the rupture process is assumed. However, dynamic simulation argues for a correlation between slip velocity and rupture velocity (Schmedes et al., 2010; Bizzarri, 2012), as well as the kinematic crack model in Section 3.2 where such correlation generates consistent synthetic STFs. We introduce in the RIK model a parametrization which correlates the local rupture velocity with the maximum slip velocity distribution on the fault. Since grid points inside each sub-event has the same rise-time and a slip velocity function with a boxcar shape, the maximum slip velocity is correlated with the final slip.

We use the slip distribution map to assign a local rupture velocity value at each grid point. To do so, we generate random uniform local rupture velocities from a median value $\overline{v_r}$ and a standard deviation σ_{v_r}. In a second step, we sort the random values such as largest

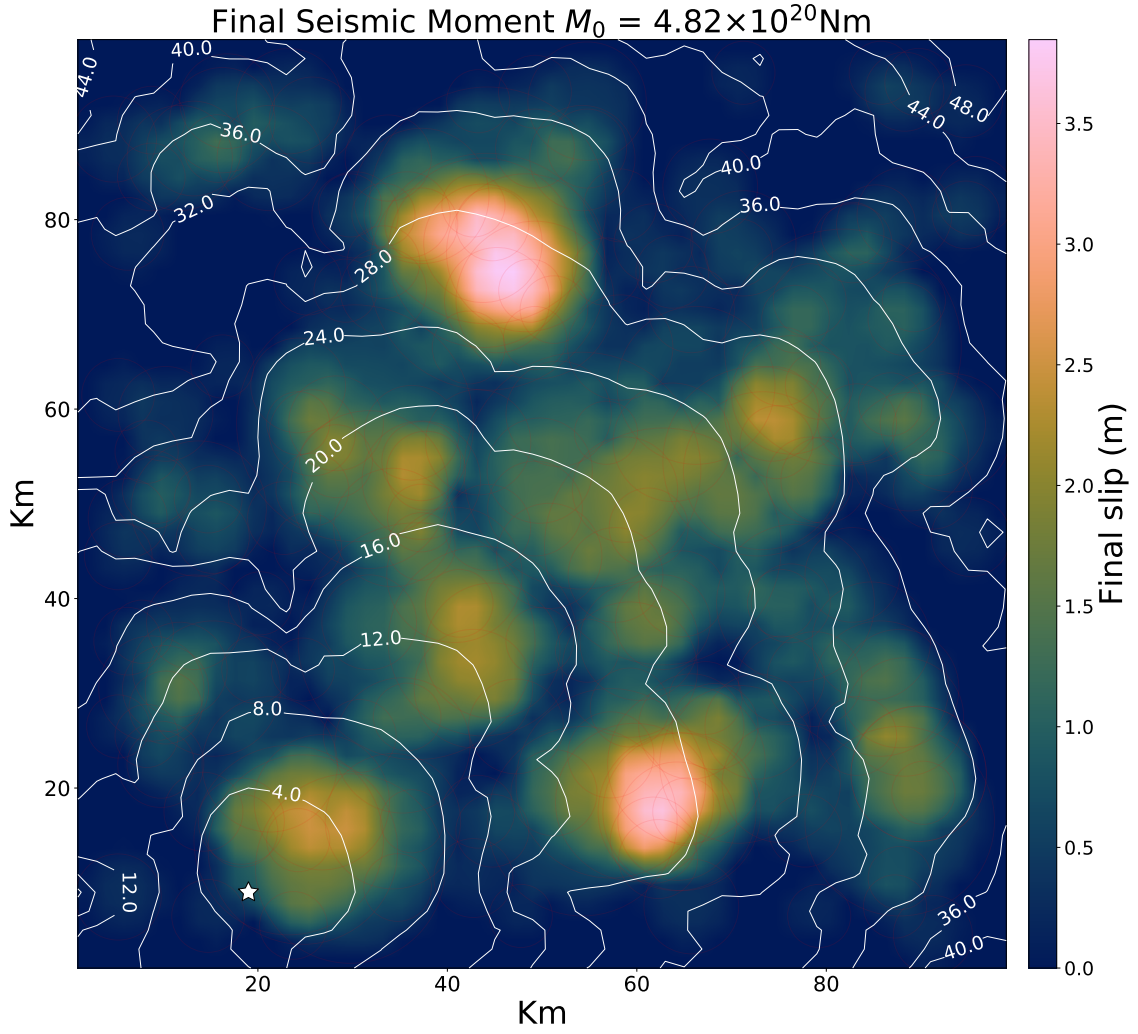

Figure 3.20 – Slip distribution of an earthquake $M_0 = 4.82 \times 10^{20}$ Nm. The hypocenter location (white star) is the same as in Figure 3.14. Red circles represent all the sub-events and highlight the numerous overlaps. Heterogeneous propagation of the macroscopic rupture front is due to correlation between slip velocity (hence slip in the RIK model) and rupture velocity. Rupture front position is located by the white line every 4 s.

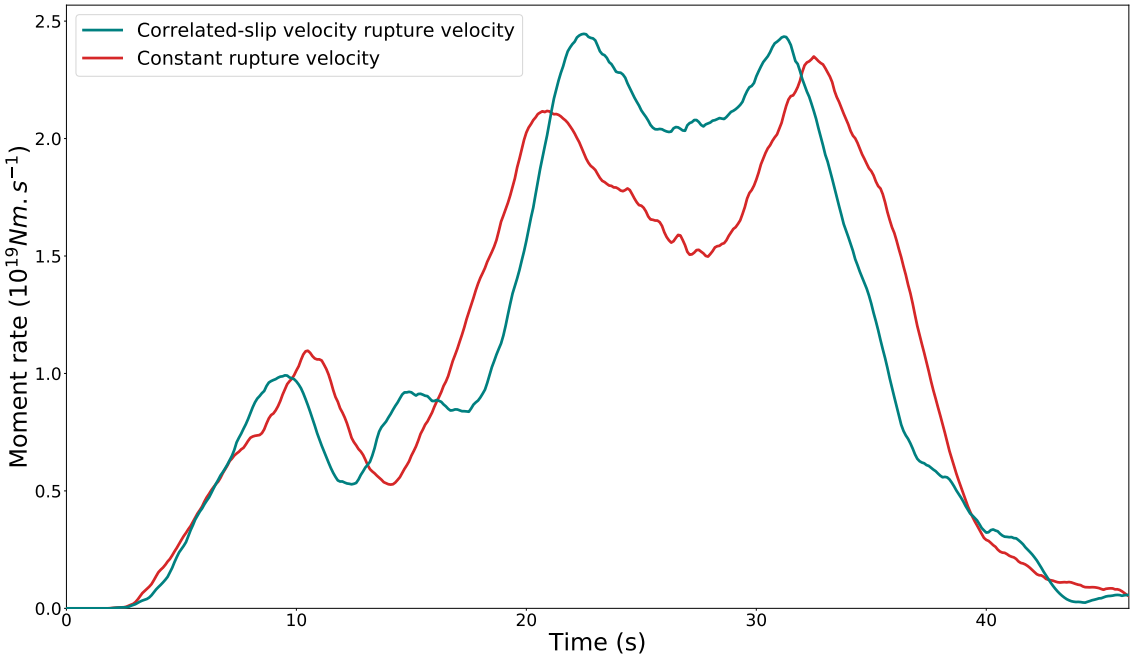

Figure 3.21 – STFs computed with the RIK model. STF in red is computed from the slip distribution and the rupture propagation shown in Figure 3.14 and is also represented in Figure 3.17. STF in teal is computed from the same slip distribution but with the rupture propagation shown in Figure 3.20 which is influenced by a slip velocity-correlated rupture velocity. In both cases, equation 3.9 is used with $a = 0.4$.

local rupture velocities coincide with largest slip. This selection is performed only with positive slip values, in order to avoid assigning most of the low local rupture velocities on grid points with no slip. The slip velocity-correlated rupture velocity distribution is finally used to compute rupture times with the approach of Podvin and Lecomte (1991). Figure 3.20 shows an example of a random slip velocity-correlated rupture velocity field leading to heterogeneous propagation of the rupture front starting from the same hypocenter and generating the same slip distribution as in Figure 3.14. Comparison between these two Figures exhibits that for Figure 3.20, rupture preferentially breaks areas with numerous overlaps of sub-events, i.e. zones of large slip and slip velocity. For instance, the bottom left rupture propagation during the first 4 s is clearly controlled by the position of large sub-event.

This correlation between slip velocity and rupture velocity is used to create 200 synthetic STFs which all share the slip distribution in Figures 3.14 and 3.20, but have a random hypocenter location. However, heterogeneous local rupture velocities considerably affect the total duration of the rupture process. In order to remain in a self-similar configuration, we adapt by trial-and-error the median rupture velocity $\overline{v_r}$ and σ_{v_r} to obtain a catalog containing STFs whose median duration respects equation 3.10. $\overline{v_r} = 1.9\,\mathrm{km.s^{-1}}$ and $\sigma_{v_r} = 0.95\,\mathrm{km.s^{-1}}$ are found to be the optimal values. Higher σ_{v_r} leads to minimum local values too slow to represent a classical rupture velocity regime. For the rise-time evolution as a function of the size of sub-events, we use equation 3.9 with $a = 0.4$. In the constant rupture velocity configuration, this value indeed contributes to produce intermediate values of moment acceleration as a function of moment rate, when referred to SCARDEC observations (see Figure 3.19). As an example, STF corresponding to the

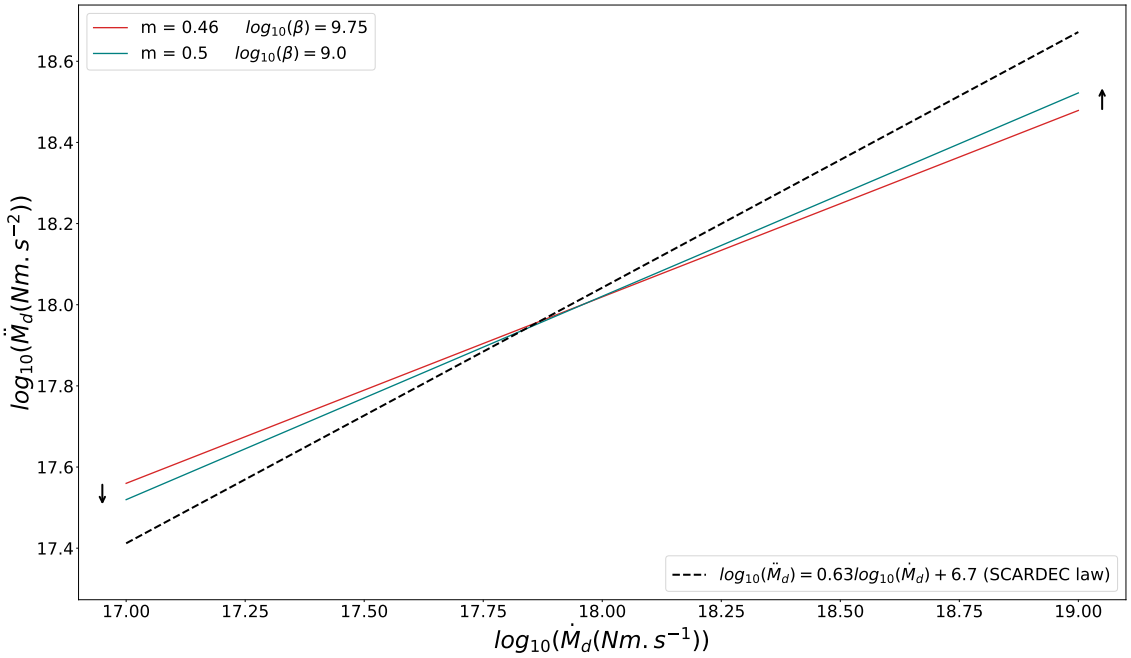

Figure 3.22 – Moment acceleration $\ddot{M}_d$ as a function of moment rate $\dot{M}_d$ (log-log scale) for two synthetic catalogs with the same rise-time $\tau(R_n)$ ($a = 0.4$). Each line is the best linear fit explaining the synthetic data. Red and teal lines correspond to catalogs with a constant and slip velocity-correlated rupture velocities respectively. For sake of clarity, moment acceleration values used to compute each fit are not shown. Black dotted line is the linear fit for the SCARDEC observations. The two arrows show the specific effect of slip and rupture velocities correlation for low and high moment acceleration values, respectively.

rupture process in Figure 3.20 is shown in teal in Figure 3.21. It is represented together with the STF obtained with the same slip distribution and a value, but a constant rupture velocity (also represented in red Figure 3.17). The global shape of the two STFs is similar since the slip distribution is the same in both cases. However each phase leading to a local maximum has a different growth. For instance, if considering the STF with a constant rupture velocity (in red) as a reference, the growth before the first local peak at around 10 s is modified for the STF in teal. The beginning part is flattened as a consequence of the local low rupture velocity while the moment rate evolution becomes steeper as it reaches the maxima due to local high rupture velocity. In terms of moment acceleration values as a function of moment rate values, it therefore seems promising to get closer to the SCARDEC observations.

After extracting the development phases from the synthetic catalog, we again represent the fit quantifying the increase of the moment acceleration as a function of the moment rate. This fit is represented in teal in Figure 3.22 together with the fit for a constant rupture velocity. As expected, the two linear fits do not share the same m and $\log(\beta)$ coefficients, meaning that the effect of the slip velocity-correlated rupture velocity shown in Figure 3.21 is globally present in the synthetic catalog. In particular, the two arrows in Figure 3.22 highlight systematic lower moment acceleration values at low moment rates and larger moment acceleration at high moment rates, leading to increase the m and decrease $\log(\beta)$ values. However, even if present, this trend is not large enough to obtain a m value close to the SCARDEC observations (black dotted line).

Previous results reveal that correlation between slip velocity and rupture velocity is most likely one of the factors contributing to reproduce the SCARDEC observations. A simultaneous transient increase of these two kinematic parameters combines large surface expansion of the rupture and high slip velocity values just behind the rupture front, and is particularly efficient to produce high moment acceleration values. However, although the crack model with variable rupture velocity in Section 3.2 allowed to fully explain the observational data, this is not the case for the RIK model. These differences arising between the two models are partly due to the different impact of a variable rupture velocity. In comparison with the crack model where an increase of the rupture velocity has an impact over the whole rupture front, the fractal property of the RIK model implies that rupture velocity acceleration is spatially localized only to high slip areas. As a consequence, surface expansion is enhanced on a small fraction of the rupture front and the resulting moment rate is less dramatically affected.

A more fundamental reason is that the crack model is controlled by the past history of the rupture (see $a(t)$ in equation 3.2). As a consequence of this dynamic property, late times are, by model construction, always more active than early ones. Slip velocity behind the rupture front (including a process zone) is continuously increasing with the surface rupture expansion over time, meaning that fast moment acceleration is systematically at late times. This is not the case in the RIK model where slip velocity is not correlated with rupture time. For instance, early times can include fast moment acceleration (when a large patch is close to the nucleation point). This kind of limitation is inherently related to the kinematic nature of the RIK model, for which a given fault point always has the same rupture history independently of what occurred earlier in the rupture. In order to overcome this limitation, we focus the Chapter 4 on dynamic models. Besides being more physical than kinematic ones, they appear required to reproduce the SCARDEC observations.

Chapitre 4

Study of the development phase from homogeneous and heterogeneous dynamic ruptures

Ce chapitre traite de l'approche dynamique de la rupture pour pleinement décrire les processus jouant un rôle lors de la phase de développement des séismes. Dans un premier temps, nous exposons quelques principes fondamentaux de la mécanique de la fracture ainsi que leur lien avec la loi de frottement "slip-weakening" utilisée pour représenter les séismes comme un phénomène frictionnel. À partir du modèle dynamique de Aochi and Ide (2004) où le paramètre de friction D_c croît linéairement avec la distance à l'hypocentre, nous adaptons son évolution ainsi que la valeur de la contrainte initiale τ_0 pour retrouver les propriétés globales des STFs. Nous montrons dans un cas continu et discontinu que les observations faites dans le Chapitre 2 peuvent être reproduites à condition de briser les lois globales auto-similaires. Avec l'approche de Ide and Aochi (2005), nous ajoutons dans un deuxième temps des hétérogénéités sur le plan de faille via une loi fractale reliant le nombre de patches, leur taille et leur valeur de D_c afin de reproduire un modèle de rupture en cascade. L'observation de la phase de développement pour plusieurs distributions aléatoires de D_c indique une propagation complexe de la rupture, dominée par une direction préférentielle contrôlée par la localisation des patches avec de faibles valeurs de D_c. Afin de générer des scénarios de rupture réalistes, une distribution aléatoire pour τ_0 est ajoutée, et accentue la complexité de la rupture. Finalement, nous observons que l'hétérogénéité de ces deux paramètres dynamiques est à l'origine de la corrélation entre la vitesse de rupture et la vitesse de glissement qui permet de reproduire les observations SCARDEC durant la phase de développement.

Les résultats de ce chapitre sont issus de travaux effectués en étroite collaboration avec Hideo Aochi.

4.1 Dynamic view of an earthquake rupture and multi-scaling numerical model

4.1.1 Stress and energy budget of an earthquake

We introduced in Chapters 1, 2 and 3 kinematic models for which the slip Δu is described in space and time on a fault, in order to have a complete description of the rupture process. As shown in equation 1.9, the circular kinematic crack model requires some assumptions such as constant static stress drop $\Delta\sigma$ and rupture velocity V_r, and displays non-physical singularities of the slip velocity $\dot{u}$ at the rupture front. A more realistic description of an earthquake then requires a dynamic view of the process. The Δu slip formulation is now not imposed but retrieved as a result of the stress conditions and the strength of the material. Rupture initiates if the stress exceeds the material strength, then it propagates until the mechanical conditions prevent further propagation. The energy budget of an earthquake provides a first indication of the static stress field evolution. The static way to investigate the problem is to consider the stresses before and after the fracture (σ_0 and σ_1, respectively). The total strain energy release W is the sum of three energies:

$$W = E_H + E_G + E_R, \tag{4.1}$$

with E_G the fracture energy, E_H the thermal energy and E_R the radiated energy (Kanamori, 2004). E_H is the friction energy, mostly dissipated by heat, while E_G is the energy me-

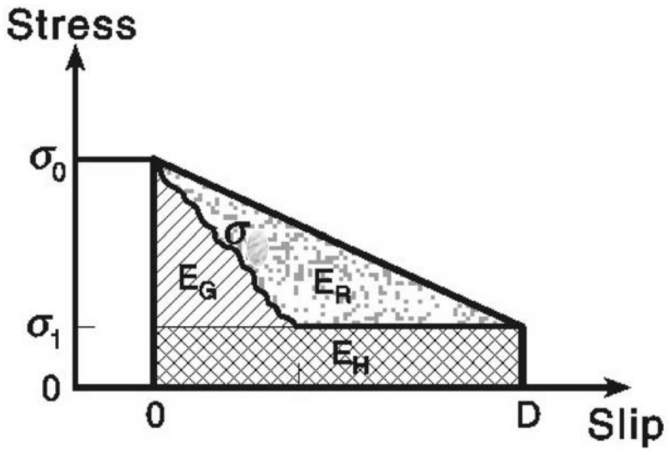

Figure 4.1 – Representation of the energy budget for static stress field dropping from σ_1 to σ_0 as a function slip D. The total strain energy consists of fracture energy E_G, thermal energy E_H and radiated energy E_R. Figure is shown for unit area of the fault plane. Graph is from Kanamori (2004).

chanically dissipated during the rupture process. The rest of the available amount energy goes into the energy radiated by seismic waves E_R. The energy partition is represented Figure 4.1 in a graph with the value of stress as a function of slip for unit area of the fault plane. The static stress drop $\Delta\sigma = \sigma_1 - \sigma_0$ produces a displacement D. The elastic energy $\Delta U = E_G + E_R$ is the available energy for the dynamic process of faulting, and is expressed as

$$\Delta U = \int_S \Delta\sigma D \, \mathrm{d}S \tag{4.2}$$

in Figure 4.1. The triangular area with a base from 0 to D and a height from σ_1 to σ_0 represents ΔU. The radiation efficiency $\eta = E_R/\Delta U$ (Husseini, 1977) is defined as the ratio between the radiated energy and the elastic energy, and is bounded between 0 and 1. η is a useful parameter for quantifying the dynamic efficiency of an earthquake. For instance, in the model of Orowan (1960), the stress drop is instantaneous, meaning that all the available energy goes into E_R and $\eta = 1$ (Savage and Wood, 1971). However, many studies show that η widely varies (Venkataraman and Kanamori, 2004; Vassiliou and Kanamori, 1982; Kanamori, 1977), implying that the fracture energy E_G has to be incorporated into the energy balance during dynamic rupture propagation.

4.1.2 Fracture surface energy and slip-weakening law

The fracture energy E_G is the amount of energy released over the entire surface to extend the fault. This energy flows into the tip of the fracture front and plays a role in the stability and the growth of the fracture. In the case of a crack model with length a, fracture mechanics impose that the extension is controlled by two quantities: the fracture energy per unit surface area required to create a new fault surface G_c (J.m^{-2}) and the crack extension force G (J.m^{-2}). For a crack in Mode III, (i.e. antiplane rupture, the direction of slip is perpendicular to the rupture propagation) growing at speed V_r, G is expressed as $G = G^* g(V_r)$ with:

$$G^* = \frac{K^2}{2\mu}, \tag{4.3}$$

where μ is the rigidity and $K = \Delta\sigma\sqrt{a/2}$ the stress intensity factor. G^* is the static extension force (that can be understood as equivalent to ΔU per unit surface area), and as $K \propto \sqrt{a}$, G^* linearly increases with the crack size. $g(V_r)$ is a function depending of V_r such as:

$$g(V_r) = 1/\sqrt{1 - V_r^2/\beta^2} \tag{4.4}$$

with β the shear wave speed (Kostrov, 1964; Eshelby, 1969).

The growth of the crack is then governed by the equation of motion $G = G_c$. This relation is particularly important as it relates the evolution of V_r to G_c. In static case $g(0) = 1$, the crack starts to destabilize if the condition $G^* = G_c$ with $G_c = K_c/2\mu$ (the Griffith rupture criterion) is respected.

For the dynamic case, the energy balance at the crack tip imposes that $G_c = G = G^* g(V_r)$ (1). This equality controls the rupture velocity V_r and the rest of the available energy converted into radiated energy. Since G^* linearly grows with the crack size and if G_c remains constant, $g(V_r)$ has to decrease to conserve the energy balance so that V_r rapidly approaches β. In contrast, if G_c abruptly increases $g(V_r)$ has to increase and the rupture may stop. Crack propagates at subshear rupture velocities when G_c increases in the same manner as G^* so that $g(V_r)$ is approximately constant. Given that the fracture energy E_G is the energy released over the fault surface S, we can finally relate it to G:

$$E_G = \int G \, \mathrm{d}S = g(V_r) \int G^* \, \mathrm{d}S \tag{4.5}$$

Relation 4.5 therefore suggests that for a large rupture velocity, small amount of elastic energy ΔU is used for E_G, implying that ΔU is mostly converted into radiated energy E_R. Such model of fracture dynamics emphasizes the critical role of G_c in the rupture propagation. As we will see in the following, G_c distribution is a key parameter controlling the earthquake dynamics.

In addition to crack theory, frictional model presents a view of an earthquake as a rupture occurring on pre-existing faults. This model assumes that fault remains locked as a consequence of the frictional interaction on either side of the fault. Earthquakes are then produced in a "stick-slip" way when the dynamic friction exceeds the static friction. In terms of stress conditions, rupture propagates when, locally on the fault, the stress field τ_0 reaches the peak strength τ_y. At this stage, an instantaneous stress drop is not physically acceptable, hence a critical slip-weakening distance D_c is required in order that τ_y decreases to the residual stress τ_1 as seen in Figure 4.2. Before the steady slip at constant stress τ_1, D_c takes place over the "process zone" behind the crack front, implying that τ_y decreases to τ_1 over a finite distance δr. The existence of such process zone also removes slip rate and stress singularities at the crack tip. This latter model is called the "slip-

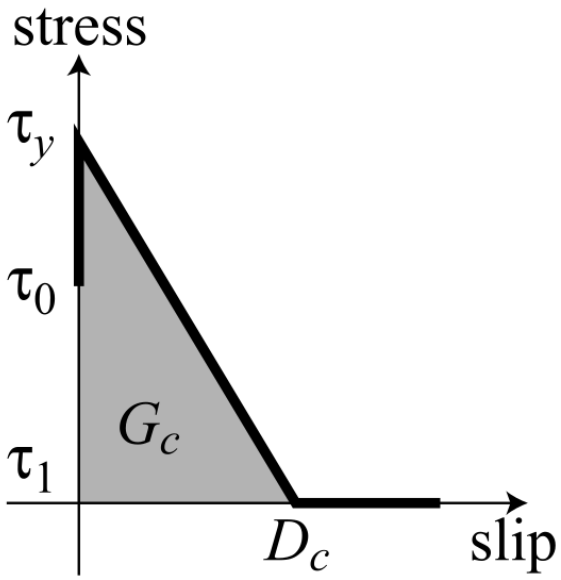

Figure 4.2 – Slip-weakening friction law represented as the stress as a function of slip. The slip-weakening distance D_c is required to shrink the stress from the peak strength τ_y to the residual stress τ_1. Fault is uniformly loaded at stress τ_0 before the rupture. G_c represents the surface fracture energy supplied to create a new surface. Graph is from Ide and Aochi (2005).

weakening friction model" (Ida, 1972) as it introduces a stress (hence friction) decrease from τ_y to τ_1 when slip increases from 0 to D_c.

In the crack model, G_c is the energy needed to produce new surface of faulting and has to verify condition (1) in order for the rupture to propagate. In the slip-weakening friction model, energy is dissipated because the dynamic stress drop $\Delta\tau_d = \tau_y - \tau_1$ includes a critical slip-weakening distance D_c. As such, G_c can be expressed as a function of the parameters of the slip-weakening friction law:

$$G_c = \frac{1}{2}\Delta\tau_d D_c \tag{4.6}$$

and is represented by the grey shaded area in Figure 4.2. equation 4.6 successfully connects crack and friction models, as it relates the fracture mechanics parameter G_c with the stress field near the fault as well as the material strength.

Besides the effect of G_c on dynamic rupture propagation, τ_0, τ_y and τ_1 have also an important role on the rupture velocity regime. Such stress parameters are gathered in the parameter S (Andrews, 1976; Das and Aki, 1977):

$$S = \frac{\tau_y - \tau_0}{\tau_0 - \tau_1}. \tag{4.7}$$

Andrews (1976) and Das and Aki (1977) study the effect of the S value on rupture velocity for a constant G_c value, and these two studies find that below 1.63, rupture velocity reaches supershear values (more or less early depending on G_c). For instance, a low material strength τ_y or a high initial stress field τ_0 tend to decrease S and enhance the

rupture velocity. As we will see in the following, a suitable balance between G_c and stress conditions on a fault is necessary to produce realistic rupture scenarios.

4.1.3 Formulation of the dynamic problem and numerical method

Based on the previous theoretical considerations, we study spontaneous dynamic rupture propagation by solving the elastodynamic equations relating the stress and particle velocity in a uniform elastic medium. According to the previous definition of the slip-weakening law, rupture propagation is controlled by: the friction parameters D_c, τ_y and τ_1 and the initial stress τ_0. They are included in the formulation of the dynamic problem as boundary and initial conditions. We adopt the boundary integral equation method (BIEM) (Fukuyama and Madariaga, 1998; Aochi et al., 2000) on a planar 2-D fault. This method estimates the stress field on the fault plane with a spatio-temporal convolution of the Green function and the slip velocity. On each spatial grid and for each time, the discrete slip velocity is a boxcar function.

Aochi and Ide (2004) take advantage of this property to produce a multi-scaling dynamic rupture based on a renormalization technique. The purpose of their approach is to efficiently model dynamic propagation regardless of the size of the rupture process. In order to have equivalent physical details for the growth of small and large earthquakes, elastodynamic equations are solved on 64×64 spatial grids for a set of four subspaces with different scales. Once rupture reaches the edge of a subspace, slip velocity functions are scaled up by a factor of 4 in both space and time, so that the lower subspace is composed of 16×16 spatial points with time steps 4 times longer in the upper subspace. The seismic moment release as well as D_c are normalized in order to conserve their value in each subspace. The smallest subspace has physical dimension of $256\,\mathrm{m} \times 256\,\mathrm{m}$ and an initial time step $\Delta t_{ini} = 0.33\,\mathrm{ms}$, meaning that after 3 renormalizations, the size of the whole space is $16.384\,\mathrm{km} \times 16.384\,\mathrm{km}$ and the final time step $\Delta t_{fin} = \Delta t_{ini} \times 4^3 = 0.0211\,\mathrm{s}$. Direction of slip is restricted to one direction on the fault, the same x-axis direction as the applied stress.

This dynamic model has therefore the ability to reproduce rupture process from a tiny event to an earthquake whose dimension is equivalent to the seismogenic layer width. The role of the dynamic quantities previously introduced in Section 4.1.2 on the development phase of earthquakes is examined through the analysis of the simulated Source Time Functions. Since the interaction between those dynamic parameters is very nonlinear, our approach in the following is to introduce step by step heterogeneities in the model, before finally approaching the most realistic scenarios. The next Section starts with continuous and discontinuous growth of D_c as a function of the hypocentral distance in a homogeneous initial stress field τ_0.

4.2 Rupture propagation on continuous and discontinuous growing fracture surface energy

Whether or not G_c is an intrinsic property on the fault is still debated. However, observational evidence highlights that most likely G_c grows with the final size of an earthquake

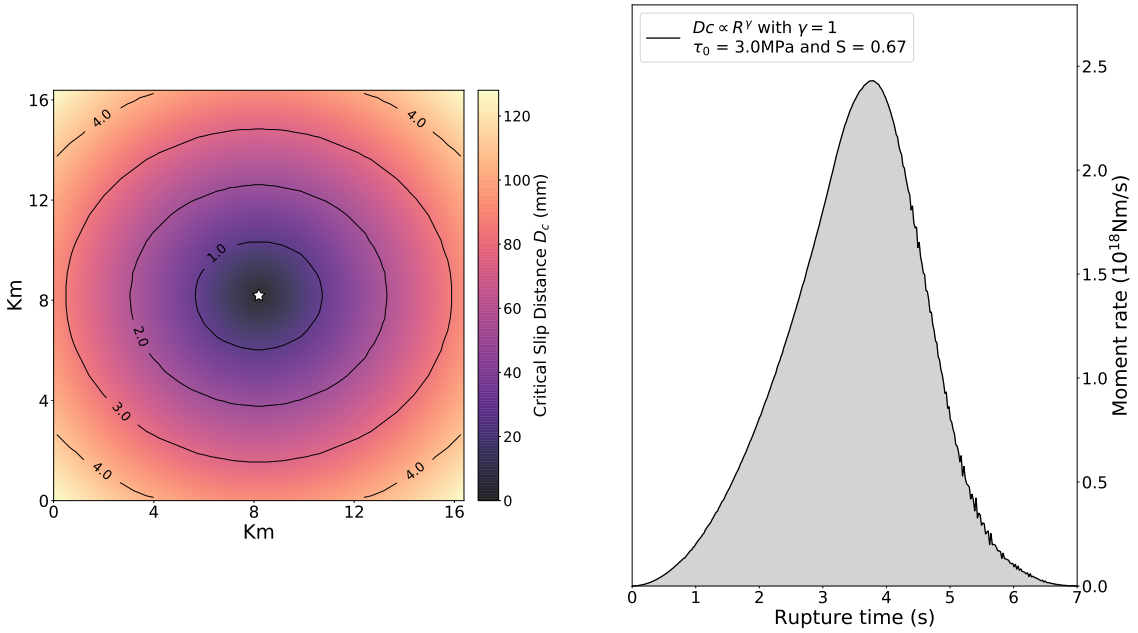

Figure 4.3 – Left: representation of the largest subspace of the fault of dimension $16.384\,\text{km} \times 16.384\,\text{km}$. Right: simulated STF for $\eta = 1$ in equation 4.8 and $S = 0.67$.

(Abercrombie and Rice, 2005; Lancieri et al., 2012). These studies spanning several order of magnitudes find values between $10^4\,\text{J/m}^2$ and $10^9\,\text{J/m}^2$. Aochi and Twardzik (2019) show equivalent correlation by collecting results from dynamic inversions. This scale-dependent G_c is often thought to originate from larger areas of inelastic deformation for larger earthquakes. As G_c is proportionnal to D_c under a uniform stress condition according to equation 4.6, we hereafter deal with D_c as a function of the earthquake size. The first study of Aochi and Ide (2004) using the multi-scaling approach in a homogeneous initial stress field τ_0 examines the effect of the coefficient η in the relation:

$$D_c \propto R^{\eta} \tag{4.8}$$

with R the hypocentral distance. They numerically demonstrate that for $\eta = 1$, rupture propagates self-similarly at constant subshear velocity, while smaller and larger η values lead to supershear rupture velocity and rupture arrest, respectively.

In addition to rupture velocity changes, we propose to examine the effect of different evolution of D_c as well as different values of τ_0 in light of the observations made in Chapter 2 with the STFs of the SCARDEC catalog. More particularly, our purpose is to adapt equation 4.7 and 4.8 in order to retrieve consistent STFs properties.

4.2.1 Continuous fracture surface energy

In our first simulation, we keep $\eta = 1$ in equation 4.8, and assign for values of τ_0, τy and τ_1 3 MPa, 5 MPa and 0 MPa respectively (the same as Aochi and Ide (2004)). The rigidity μ is equal to 32.4 GPa and the P and S wave velocities to $V_p = 6.0\,\text{km.s}^{-1}$ and $V_s = 3.46\,\text{km.s}^{-1}$ respectively. The rupture artificially initiates at $t = 0$ in the middle

of the first subspace in a stress-free circular area of 15 m and then propagates in larger subspaces. We make several tests to find the suitable proportionality coefficient relating R and D_c such as the simulated STF is in agreement with SCARDEC observations. As shown in Figure 4.3 our optimal linear increase of D_c is chosen so that furthest points from the hypocenter have D_c values equal to $D_{cmax} = 128$ mm. In accordance with Aochi and Ide (2004), we observe a constant rupture velocity around 2.5 km.s^{-1} in mode II (i.e. horizontally in the left panel of the Figure 4.3) and consequently a very smooth STF growth. The rupture grows in every directions before hitting the fault bounds at a time where the peak STF is approximately reached.

Such optimal linear increase of D_c is selected on the basis of suitable values of moment acceleration as a function of moment rate in the development phase, as shown in Figure 4.4. Indeed, after extracting the development phase with the method detailed in Section 2.2.1 (blue growth in the middle of the Figure 4.4), moment acceleration values from the simulation are computed according to the procedure in Section 2.2.2 (blue dots in the bottom of the Figure 4.4). The blue linear fit (calculated in the same way as previous Chapters, see details in Section 2.3.1) shows a trend close the SCARDEC dotted line, meaning that such D_c values are well adapted to reproduce realistic STFs. In contrast, when we assign other proportional coefficients, we observe that larger D_c values lead to an early arrest of the rupture while lower ones produce too high moment acceleration values. We do not intent here to exactly fit the black dotted line with equivalent slope and intersect, because as we will see in the following, it necessitates a more complex fault configuration. Instead, we first select D_c evolution which generates simulated moment acceleration values in the same order of magnitude as the SCARDEC ones.

The effect of the non-dimensional parameter S on STFs is also studied by varying the value of the homogeneous initial stress τ_0. According to in equation 4.7, S is inversely dependent to τ_0. We test three different values for τ_0 leading to three different values of S. These configurations are represented Figure 4.4 with τ_0 values of $2.7, 3.0, 3.5$ MPa, and consequently S values equal to $0.85, 0.67, 0.43$ in green, blue and red respectively. Top of the Figure 4.4 depicts with the black line the linear increase of D_c together with the evolution of the rupture time as a function of distance from hypocenter. As expected from theoretical considerations (Andrews, 1976), S is anticorrelated with the rupture velocity. In mode II, ruptures with $S = 0.85$ (green) and $S = 0.43$ (red) have rupture velocities of 2 km.s^{-1} and 3.4 km.s^{-1} respectively. This latter rupture velocity is equivalent to V_s and therefore excludes such low S value as a realistic overall configuration. At the bottom of the Figure 4.4 we represent the evolution of the moment acceleration as a function of moment rate during the development phase. For the three fits, S has no influence on the value of the slope $m \simeq 0.5$. This value stands for the self-similar growth of the development phase, i.e. a temporal evolution of the moment rate with a power $n_d = 1/(1-m) = 2$ (more details in Section 2.9). This self-similar behavior is consistent considering that $\eta = 1$ (constant rupture velocity) and the static stress drop $\Delta\tau = \tau_0 - \tau_1$ is constant. However, and consistently with the kinematic study of the crack (Section 3.2.3), the variation of S (hence $\Delta\tau$) is correlated with the intercept $\log(\beta)$ of the fits. As a consequence, while $\tau_0 = 2.7$ and 3.5 MPa are respectively too low and too large to reproduce SCARDEC fit, $\tau_0 = 3$MPa gives acceptable results. Such simple parametric study therefore constrains at a

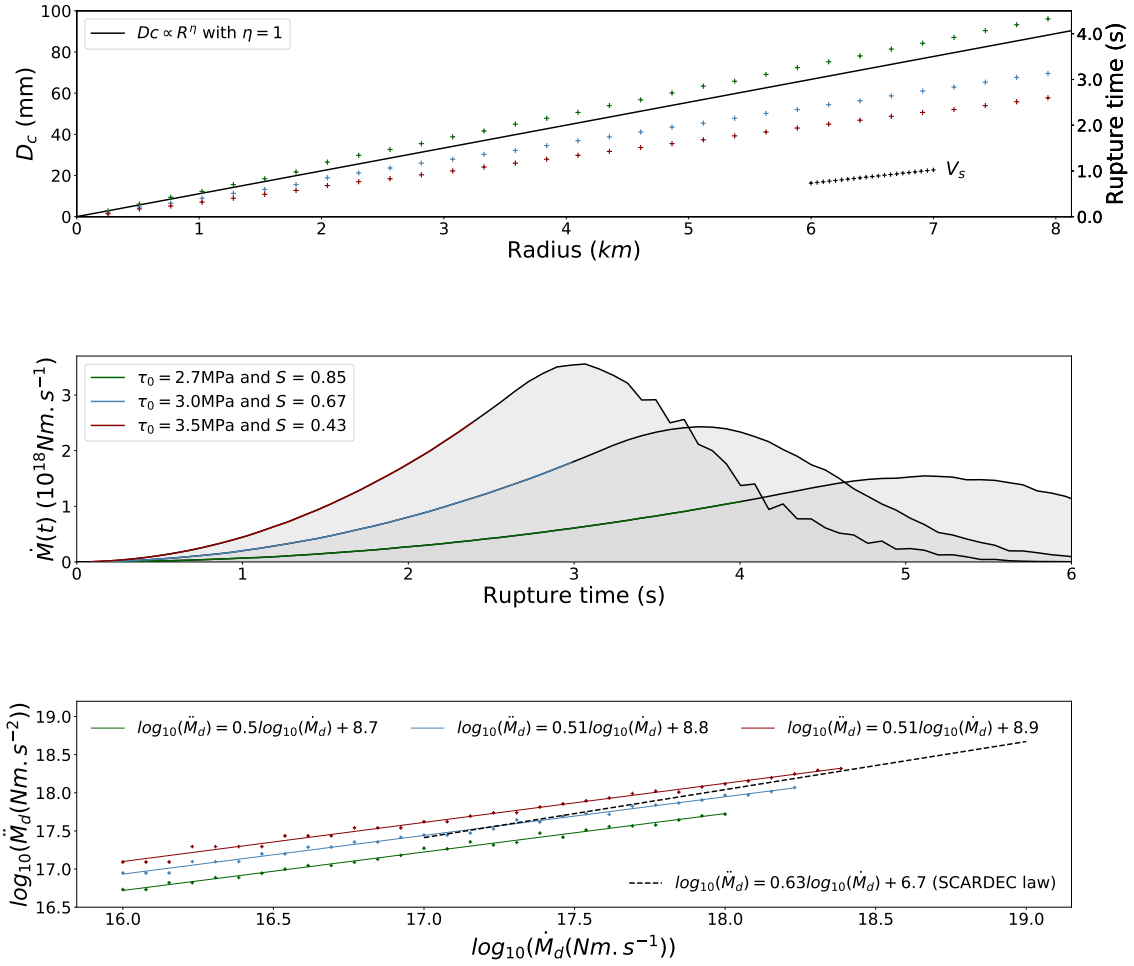

Figure 4.4 – Top: Evolution of D_c (black line) together with the rupture time (colored crosses) as a function of the distance from the hypocenter. Green, blue and red colors refer to $S = 0.87, 0.67, 0, 43$ respectively. Rupture time as a function of distance for V_s velocity is represented by black crosses. Middle: STFs for the different S values. Bottom: Moment acceleration as a function of moment rate. Colored lines are the fits calculated with the colored points. Dotted black line is the fit from SCARDEC observations.

very first order the values of $\tau_0 = 3\,\text{MPa}$ and a linear increase of D_c with $D_{cmax} = 128\,\text{mm}$, which will be our reference values in the following.

The self-similar growth of STFs in the case of equation 4.8 with $\eta = 1$ however does not explain the rapid evolution of the moment acceleration as a function of moment rate seen in SCARDEC observations, as represented by the slope $m = 0.63$ of the black dotted line in Figure 4.4. One way to modify this property is to adapt the η value such as the rupture velocity is not constant anymore. Unlike the study of Aochi and Ide (2004), we do not select extreme η values leading to a complete arrest of the rupture before reaching the fault bounds or supershear rupture velocities all along the rupture process. Instead, we slightly adjust η and compare the simulated STFs, by taking advantage of the previous analysis ($\tau_0 = 3\,\text{MPa}$ and $D_{cmax} = 128\,\text{mm}$ fixed). Figure 4.5 represents three different configurations, with $\eta = 0.89$, 1 and 1.2 in green, blue and red respectively. The blue color is exactly the same configuration as the blue color in Figure 4.4. At the top, colored lines illustrate profiles for the three values of η. The first observation is that, for $\eta = 0.89$ and 1.2, evolution of rupture times is not linear as a function of distance from hypocenter, implying that the rupture velocity changes during the rupture process. For $\eta = 1.2$, rupture easily starts then propagates slower as a consequence of the rapid increase of D_c. Conversely, for $\eta = 0.89$, high D_c values are early reached, constraining the rupture to be slow at the beginning, before it progressively accelerates as the increase of D_c is less pronounced. These rupture velocity variations cause a modification of the evolution of the moment acceleration as a function of moment rate during the development phase as summarized at the bottom of Figure 4.5. While for $\eta = 1.2$, rupture deceleration generates a modest increase on the moment acceleration with coefficient $m = 0.45$, the case of $\eta = 0.89$ in green has coefficients $m = 0.63$ and $\log(\beta) = 6.7$ and is in agreement with SCARDEC observations. This configuration is very similar to the analytical configuration developed in Section 2.3.3 for a kinematic formulation of a crack model. It has been shown that the evolution of the moment acceleration of SCARDEC STFs can be fully explained by a rupture acceleration of the form pt^γ with $\gamma = 0.23$. We can also determine the coefficient γ in our dynamic simulation in order to compare the kinematic and dynamic view of a crack propagation. To do so, we first fit in log-log scale the evolution of the rupture times as a function of the crack radius, represented by the green crosses at the top of Figure 4.6. We finally use the coefficients from this fitting law to derive the average evolution of the rupture velocity with time $v_{rd}(t)$. Such rupture acceleration is shown in the middle of Figure 4.6. We find $\gamma = 0.13$, meaning that as in the kinematic crack model, $v_{rd}(t)$ accelerates very rapidly to classical rupture velocities, then slowly increases during the remaining part of the development phase. However, as for the kinematic model, this interpretation requires that larger earthquakes with longer development phases have higher local rupture velocities, which is not clearly observed for real earthquakes.

4.2.2 Discontinuous fracture surface energy

Dynamic simulations carried out in Section 4.2.1 are useful to provide a first insight of the global tendency for various D_c evolution and initial stress τ_0. However, the simulated STFs are simple, and complexity has to be added in order to reproduce the variability found in real rupture propagation. As a very first step towards complexity, we consider a

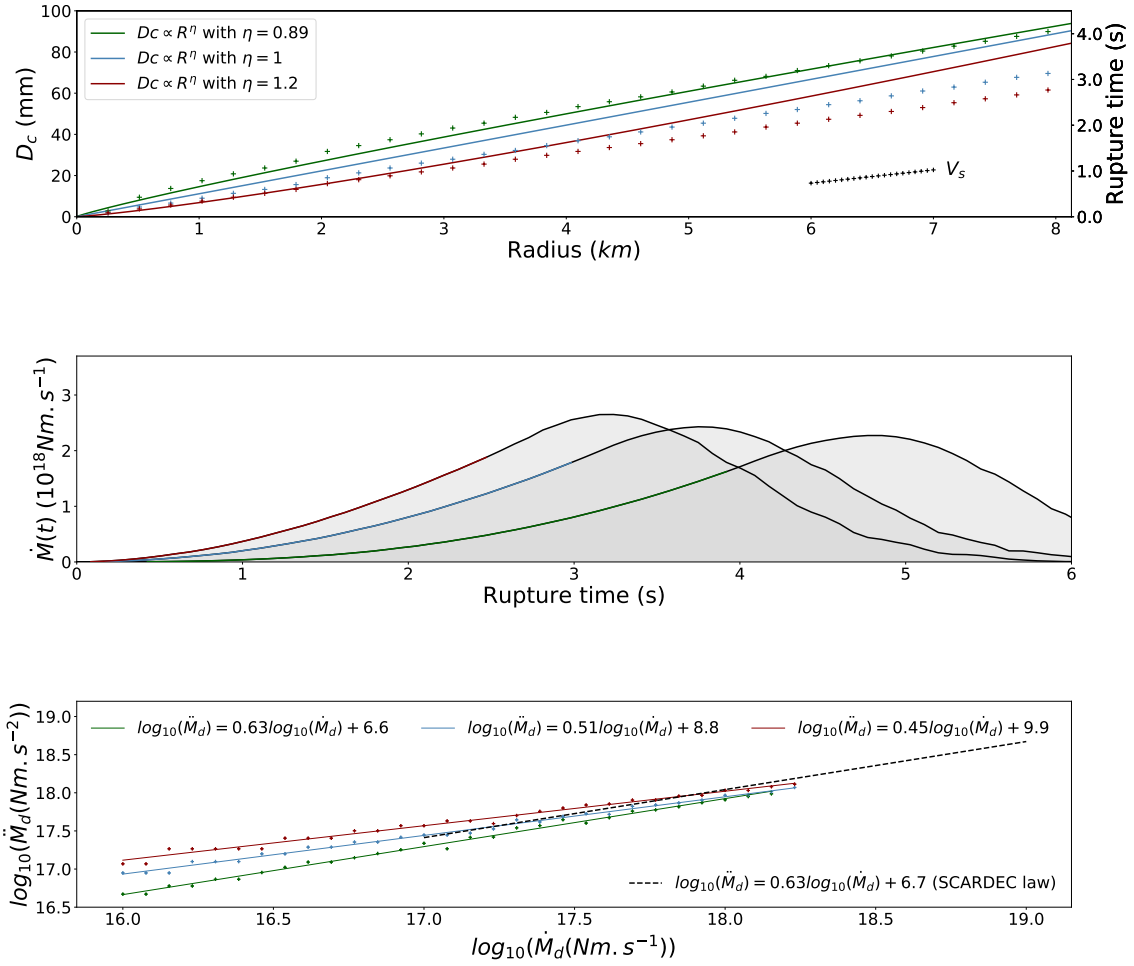

Figure 4.5 – Top: Evolution of $D_c \propto R^{\eta}$ together with the rupture time (crosses) as a function of the distance from the hypocenter for three different values of η. Green, blue and red colors refer to $\eta = 0.89, 1, 1.2$ respectively. Rupture time as a function of distance for V_s velocity is represented by black crosses. Middle: STFs for the different η values. Bottom: Moment acceleration as a function of moment rate. Colored lines are the fits calculated with the colored points. Dotted black line is the fit from SCARDEC observations.

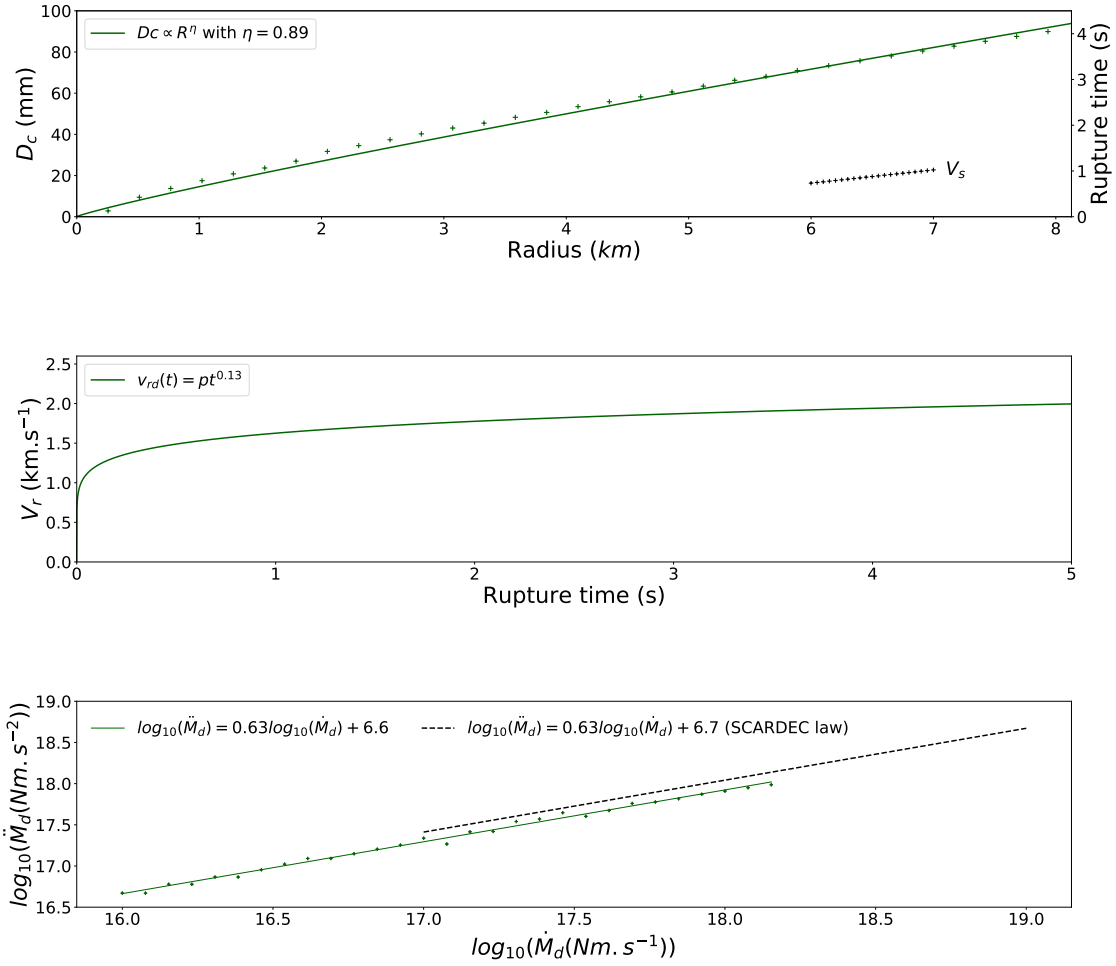

Figure 4.6 – Top: Evolution of $D_c \propto R^{0.89}$ together with the rupture time (crosses) as a function of the distance from the hypocenter. Rupture time as a function of distance for V_s velocity is represented by black crosses. Middle: average rupture velocity acceleration $V_{rd}(t)$ deduced from the evolution of the rupture time as a function of the distance from the hypocenter. Bottom: Moment acceleration as a function of moment rate. Dotted black line is the fit from SCARDEC observations.

serie of $n+1$ discrete concentric circular patches of radius r_n and critical slip D_{cn}. The centers of all circular patches with different radii are superimposed in the middle of a fault as in Section 4.2.1. Instead of a continuous linear increase with the radius of the crack, the evolution of D_c is supposed discontinuous such as:

$$r_n = 2^n r_0 \quad \text{and} \quad D_{cn} = 2^n D_{c0} \tag{4.9}$$

with r_0 and D_{c0} the radius and D_c value of the smallest patch respectively. We assume $r_0 = 22.5\,\text{m}$, $D_{c0} = 0.25\,\text{mm}$, so that $r_8 = 5.67\,\text{km}$ and $D_{c8} = 64\,\text{mm}$ ($n = 8$). Such configuration enables to respect exactly the same relation as in equation 4.8 with $\eta = 1$ except that D_{cn} transitions are now step-like. Points at a distance beyond r_8 from the hypocenter are assigned with $D_{cmax} = 128\,\text{mm}$. We keep a homogeneous initial stress $\tau_0 = 3\,\text{MPa}$. Figure 4.7 represents on the left the distribution of D_c on the fault as well as the simulated STF on the right. Step-like transition between each patch acts as a barrier to the rupture propagation, as demonstrated by the irregular spaces between the contours of the rupture front every second. Such behavior is directly related to the balance between energy release rate G and G_c. Since only G gradually increases with the size of the crack, rupture suddenly slows down when it goes through a larger patch (hence larger G_c). Then rupture continues to extend after G sufficiently grows to rebalance the energy budget. The rupture complexity is even more visible when looking at the simulated STF, whose growth is composed of several successive monotonic phases. Each monotonic phase corresponds to a propagation in a given patch, and their duration increases as the radius of the patches increases. As an example, the two last monotonic phases are associated to the propagation in patches with $D_{c7} = 32\,\text{mm}$ and $D_{c8} = 64\,\text{mm}$. Declining phases are also longer for higher step-like transition of D_c. On the basis of these remarks about the complexity of the STF shape, we can easily distinguish the discrete radius-D_c relation expressed in equation 4.9.

A second configuration is to consider the same case as in Figure 4.7 but with an infinite size for r_8, meaning that now points with a distance from the hypocenter beyond $r_7 = 2.88\,\text{km}$ have $D_c = 64\,\text{mm}$. We show this configuration in Figure 4.8. The colorbar for D_c is kept the same in order to clearly identify the difference with Figure 4.7. The calculated STF has exactly the same evolution as the STF in Figure 4.7, as a result of an equivalent D_c evolution, until it propagates in the last subspace. This finally creates a peak moment rate value twice larger as a consequence of the constant D_{c8} over most of the surface of the last subspace. Despite this feature, rupture velocity does not reach supershear values as the rupture reaches the model boundary. Figure 4.9 highlights the similarities and differences of both models by showing D_c evolution and the associated STFs. In order to examine the effect of such break in D_c-scaling on the development phase, we represent the evolution of the moment acceleration as a function of moment rate as shown in the bottom of the Figure 4.9. Despite its more complex rupture growth with combination of several monotonic phases, model without break in D_c-scaling (in red) has a slope value of $m = 0.51$, meaning that the development phase still has a self-similar property. However, when the rupture is not constrained by a background D_{cmax}, the fit (in green) displays $m = 0.6$ and thus approaches SCARDEC observations.

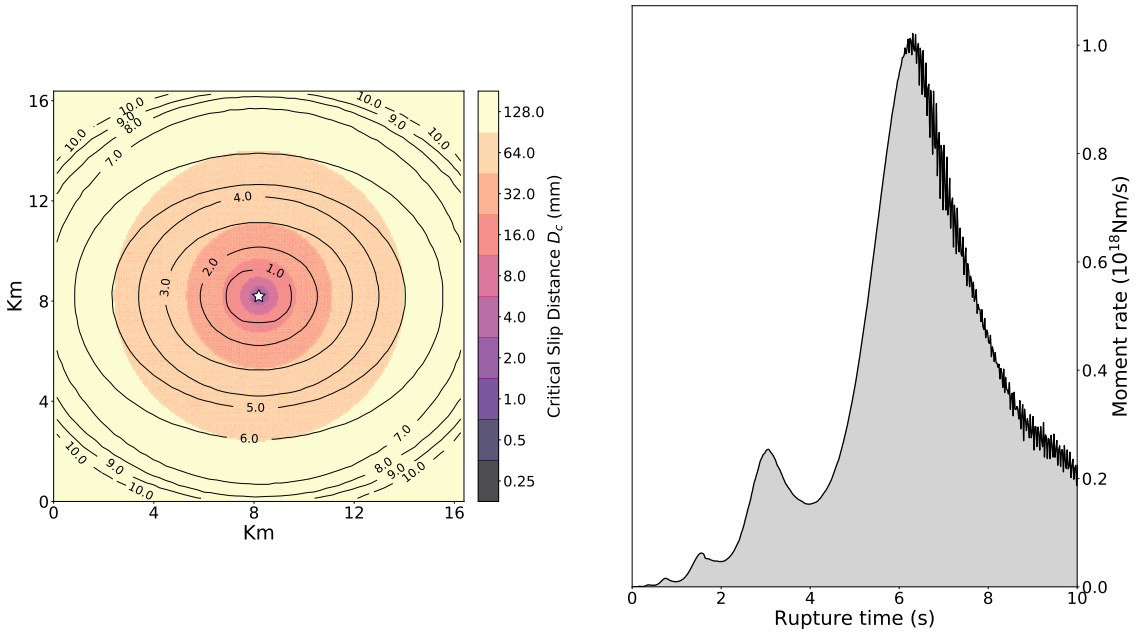

Figure 4.7 – Left: representation of the largest subspace of the fault of dimension $16.384\,\text{km} \times 16.384\,\text{km}$. Discrete colorbar shows the step-like evolution of D_c with the distance from the hypocenter (white star). Contours of the rupture front every second are represented by the black lines. Right: simulated STF.

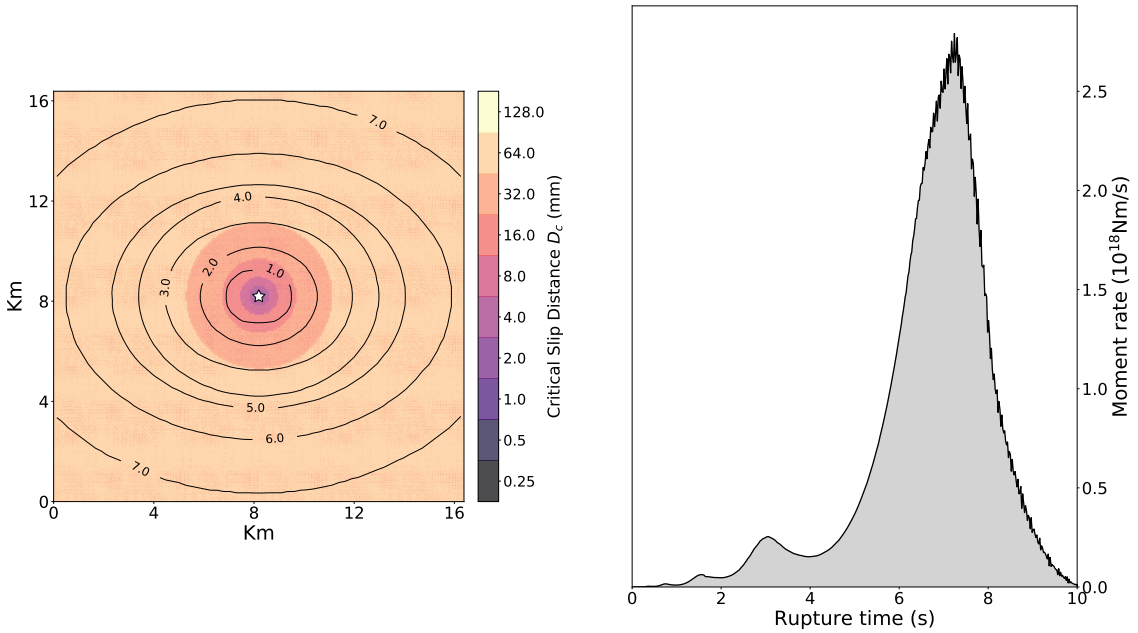

Figure 4.8 – Left: representation of the largest subspace of the fault of dimension $16.384\,\text{km} \times 16.384\,\text{km}$, with an infinite size for the largest patch. Discrete colorbar shows the step-like evolution of D_c with the distance from the hypocenter (white star). Contours of the rupture front every second are represented by the black lines. Right: simulated STF.

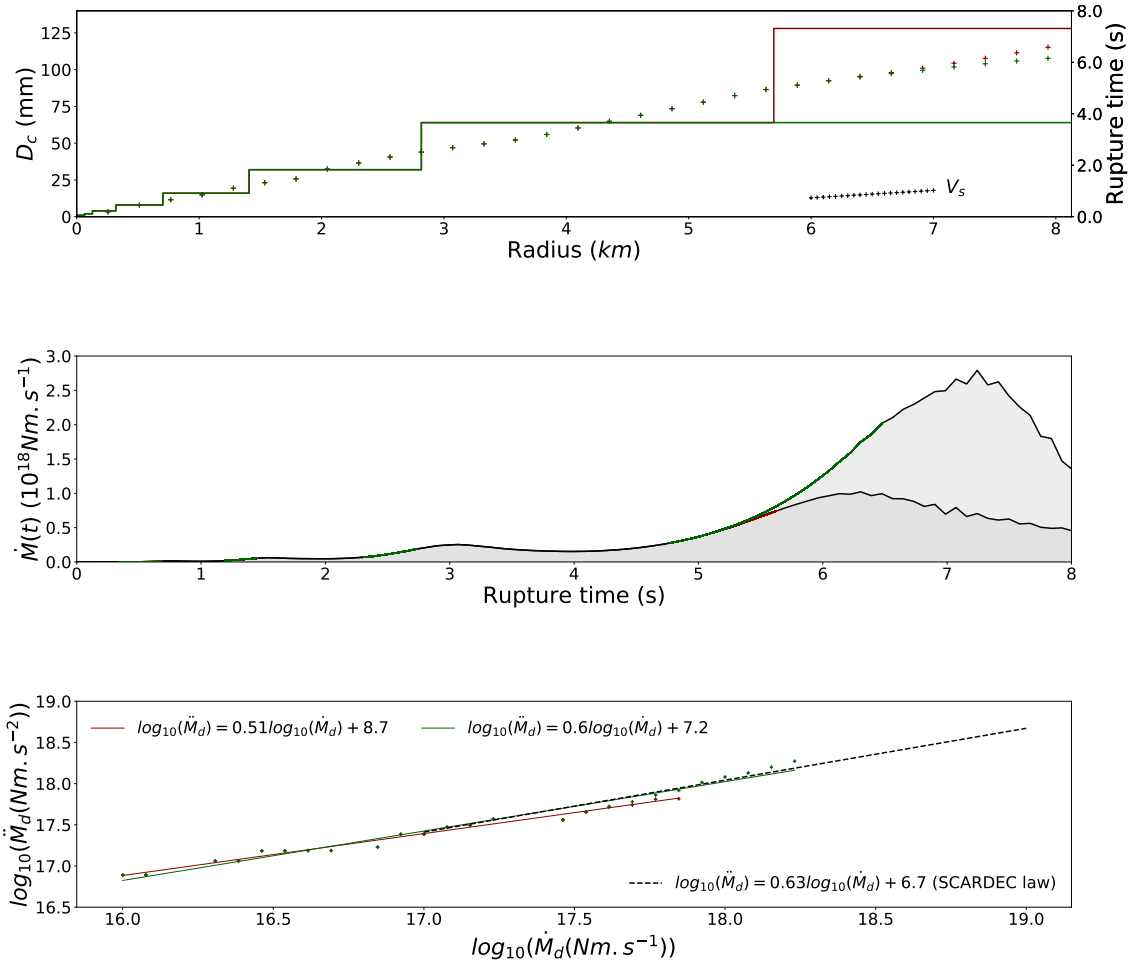

Figure 4.9 – Top: step-like evolution of D_c together with the rupture time (crosses) as a function of the distance from the hypocenter for models in Figures 4.7 (in red) and 4.8 (in green). Rupture time as a function of distance for V_s velocity is represented by black crosses. Middle: STFs for both models. Bottom: Moment acceleration as a function of moment rate. Colored lines are the fits calculated with the colored points. Dotted black line is the fit from SCARDEC observations.

In this model, one assumption to approach SCARDEC observations is to consider that an earthquake is represented by the rupture of small patches preceding one large patch on the fault which controls the main properties of the development phase. As seen previously, even if the beginning of the rupture process is self-similar as it propagates gradually into patches of larger and larger sizes, the rupture of the last dominant patch reproduces consistent moment accelerations. A possible explanation is that the rupture initiates on self-similar growing patches, before triggering a much larger favorable patch whose size is representative of the final magnitude size. The D_c distribution on the left of the Figure 4.8 can therefore be seen as a nondimensional representation of a fault, where earthquakes of all sizes are the result of such configuration. Variation of the fault dimension would determine the size of a characteristic patch and the final size of the earthquake. This explanation however implies that the steady hierarchical structure with regular increase of patch size is not respected since last patch dominates the other ones, which also leads to break the global self-similar behavior.

4.3 Effect of heterogeneous distribution of fracture surface energy on the development phase

4.3.1 Multiscale fractal D_c distribution of circular patches

The two models in Section 4.2 suggest breaks in self-similar properties in order to reproduce the observational evolution of the moment acceleration as a function of moment rate during the development phase. Our observations likely originate from a more complex fault system, as proposed by recent studies of Okuda and Ide (2018) and Ide (2019). They observe identical features for initial seismic waveforms of small and large earthquakes, suggesting a magnitude-independent signal just like our observations in Chapter 2. This universal rupture growth is explained by a cascade model where hierarchical structures with increasing sizes are successively triggered with no information about the final size before the rupture stops. Whether a rupture grows into a small or large earthquake depends on physical properties of the fault, such as D_c. In contrast with the D_c distribution shown in Figure 4.7, irregularities on faults are often considered to follow a fractal number-size distribution, so that numerous small events can trigger few larger ones depending on the spatial distribution of patches. Numerical simulations (Noda et al., 2013; Ide and Aochi, 2005) propose such heterogeneous fractal D_c distribution, and successfully reproduce various scales of cascading ruptures. The numerical approach of Ide and Aochi (2005) shows macroscopic self-similar properties, as well as magnitude-independent growth of STFs over a large magnitude range. This similarity with the SCARDEC STFs leads us to explore the effect of heterogeneous distribution of D_c on the development phase.

Based on the fault model of Ide and Aochi (2005), we assume a self-affine fractal topography as an analogy of the heterogeneous D_c distribution, with the same power laws as in equation 4.9. This parametrization is based on the parametric study done in Section 4.2.1 which constrains the evolution of D_c as a function of the patch size. In contrast with Section 4.2.2, the number-size distribution of patches is fractal, with N_n the number of circular patches of the n-th order and $D = 2$ the fractal dimension such as:

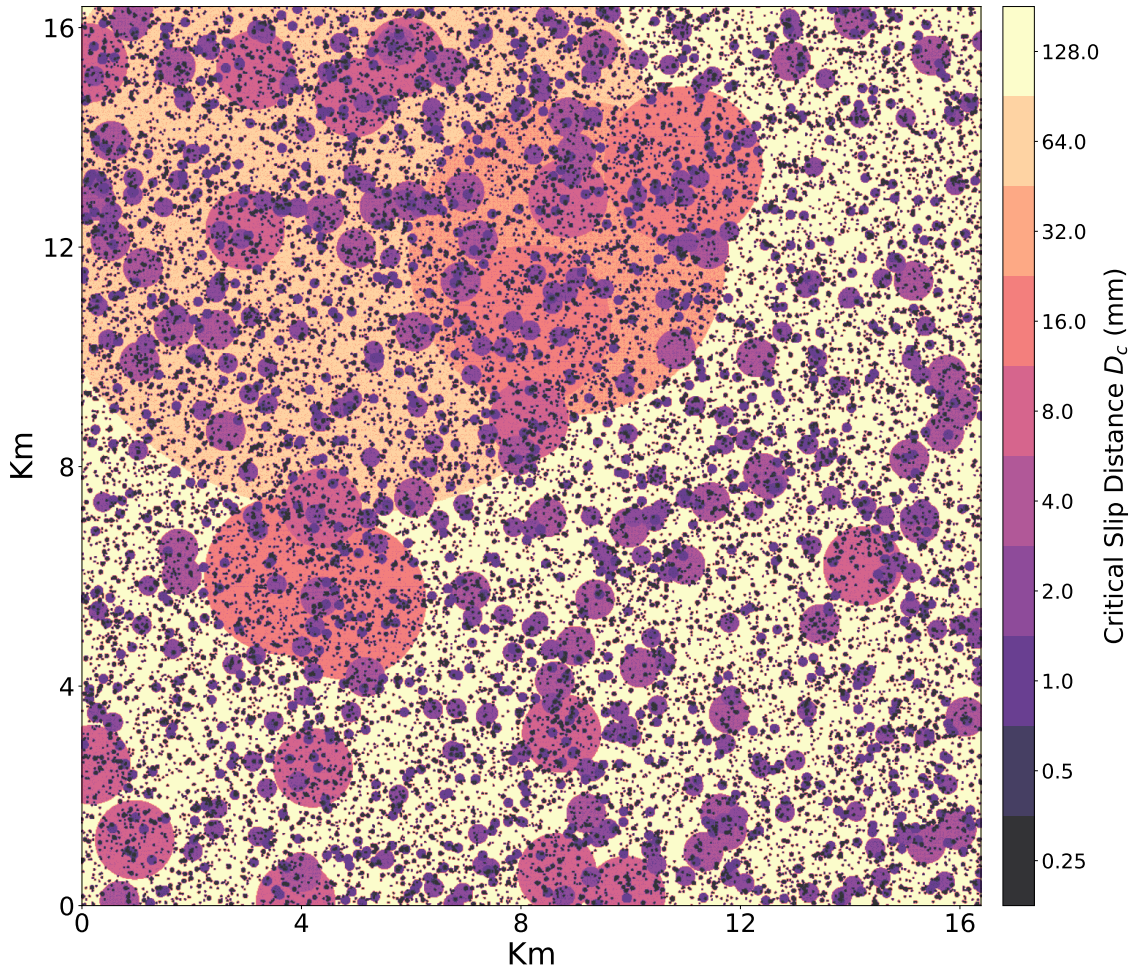

Figure 4.10 – Representation of a fault heterogeneity map from a random circular patches position. The number of circular patches follows a fractal size-number relation. D_c is assigned on each patch following equation 4.9. Fault dimension is $16.384\,\text{km} \times 16.384\,\text{km}$ with 4096×4096 points.

$$N_n = 2^{-Dn} N_0, \tag{4.10}$$

where $N_0 = 16384$ is the number of the smallest patches. We keep $r_0 = 22.5\,\text{m}$ as well as $D_{c0} = 0.25\,\text{mm}$, so that for the 7th order of patch, there is $N_7 = 1$ patch of radius $r_7 = 2.88\,\text{km}$ with $D_{c7} = 32\,\text{mm}$. We add also a 8-th patch of radius $r_8 = 5.76\,\text{km}$ with $D_{c8} = 64\,\text{mm}$, and a final "background" $D_{cmax} = 128\,\text{mm}$. As such, we create consistent fault heterogeneity map which still takes into account the D_c evolution determined in Section 4.2.1. A random realization of patches position following this procedure is shown in Figure 4.10. When several circular patches are superimposed, we assign the smallest D_c value on the fault plane. Peak strength $\tau_y = 5\,\text{MPa}$ and residual stress $\tau_1 = 0\,\text{MPa}$ are the same as previously. Distribution of D_c is generated on 4096×4096 elements in order to have the same spatial discretization as the smallest subspace (grid size 4 m). The procedure of artificial rupture initiation with a stress-free region on 15 m is done in all the zero-order patches, i.e. $N_0 = 16384$ earthquakes are artificially triggered. We assume a homogeneous initial stress field $\tau_0 = 3\,\text{MPa}$ before each event in order to only isolate the effect of heterogeneous D_c. Ide and Aochi (2005) successfully reproduce classical frequency-magnitude power law decay close to the Gutenberg-Richter relation. In the following, we analyze only the growth of earthquakes which break the whole space since the model is by design a cascade process where large earthquakes start on the same small patches as the small ones.

4.3.2 Complex rupture propagation of largest events

We generate fault heterogeneity maps in which we simulate earthquakes with an initiation on each of the smallest patches. Depending on the patch distribution, some heterogeneity maps do not produce earthquakes which propagate in the "background" infinite patch. We finally obtain 6 different maps where suitable patch distributions create an earthquake with cascade propagation into all patches. Such maps are represented together with the contours of the rupture front every second in Figure 4.11. In order to clearly distinguish the effect of D_c distribution on the rupture propagation, we superimpose the 4096×4096 initial heterogeneity map with contours of the rupture front in Figure 4.11. We observe complex rupture propagations due to the stochastic distribution of patches. Ruptures have a clear preferential direction of propagation, as a result of the random patches distribution. The "background" D_{cmax} in particular acts systematically as a barrier and constrains the rupture to first propagate into patches with smaller D_c. For instance in map d) in Figure 4.11, although the rupture starts from one of the smallest patches and propagates into larger ones, it reaches D_{cmax} after $\sim 1\,\text{s}$ to the right, which causes a leftward rupture propagation. This preferential rupture direction is less pronounced when largest patches are closer to each other, as in cases of f) and a). We also note that when rupture propagates into the largest patches as the one with $D_{c8} = 64\,\text{mm}$, the smaller overlying patches locally increase the rupture velocity. This effect is for example observed in map b) for the contour of the rupture at 3 s, where rupture preferentially breaks the small patch with $D_{c5} = 8\,\text{mm}$ to the left.

Dynamic simulations offer a direct insight on the interaction between dynamic and kine-

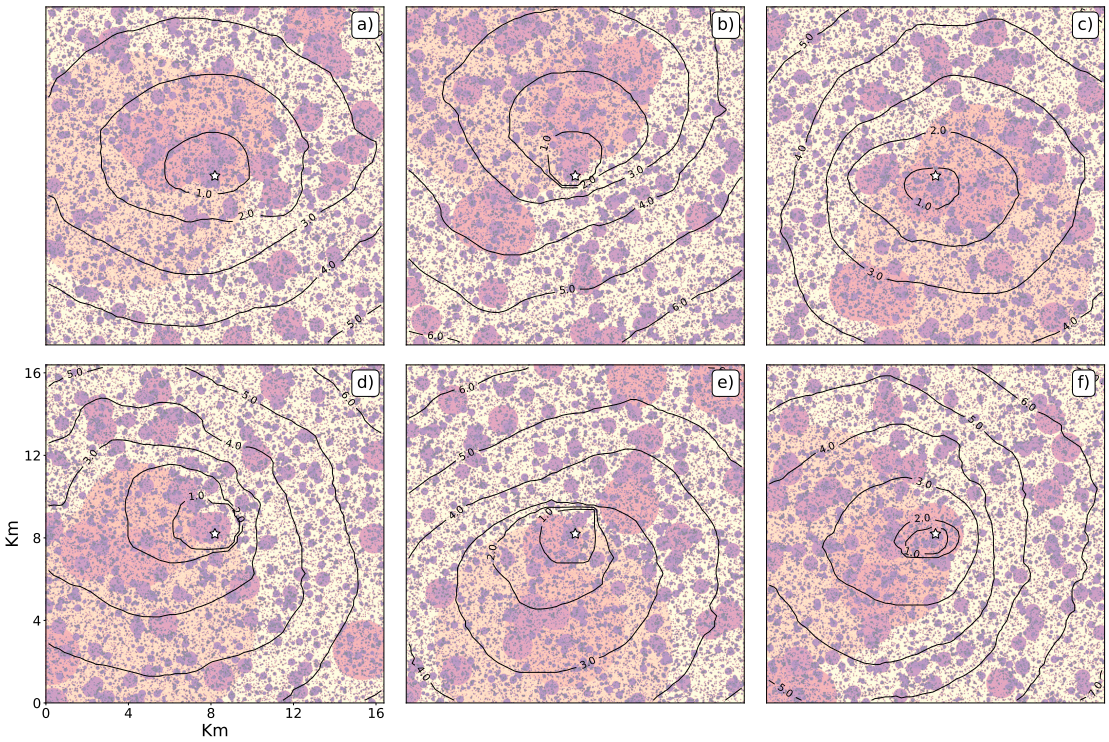

Figure 4.11 – Representation of six fault heterogeneity maps from a random circular patches position. White star is the position of the hypocenter. Colorbar and b) are the same as in Figure 4.10. Black lines show the contours of the rupture front every second.

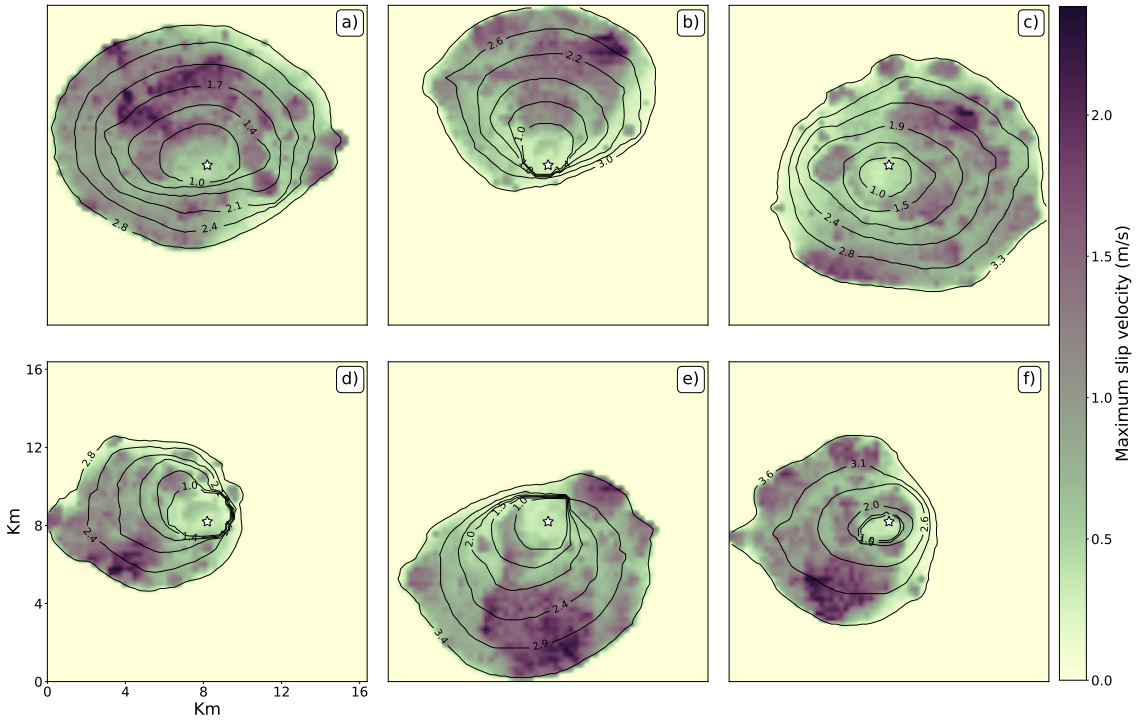

Figure 4.12 – Representation of the maximum slip velocity for the six simulations with D_c distributions in Figure 4.11. White star is the position of the hypocenter. Black lines show the contours of the rupture front for six different times. Maximum slip velocity is extracted before the rupture front reaches fault bounds.

matic properties of the rupture. As we saw previously that moment rate evolution is dependent on slip velocity and surface rupture expansion, we represent in Figure 4.12 the maximum slip velocity, stopping at the time when rupture reaches the fault bounds. After this time, surface rupture expansion is constrained by the fault dimension and affects the evolution of the moment rate; stopping phase is generated by the model boundary, such as the entire rupture process starts to slow down. We therefore analyze in the following the rupture process only until this time. There is a clear correlation between rupture velocity and slip velocity, as shown by the purple colors associated with large surface ruptured in short times.

In order to summarize observations from Figures 4.11 and 4.12, we see that rupture starts to propagate on the smallest patches with small D_c and slows down when reaching the "background" with D_{cmax}. Such effect leads to a preferential direction of propagation. As soon as the rupture reaches the largest patches with large D_c, rupture velocity as well as slip velocity locally increase when smaller patches are broken inside. This local correlation is consistent with other dynamic studies (Bizzarri, 2012; Schmedes et al., 2010) and has been shown to be required for the kinematic crack with variable rupture velocity in Section 3.2. The next paragraph analyzes the simulated STFs and their development phases for the six heterogeneous D_c maps, in order to have a more detailed comparison with the SCARDEC observations.

4.3.3 Simulated STFs extracted from dynamic simulations for heterogeneous D_c distribution

One of the origins of source variability comes from heterogeneous D_c distribution on the fault plane. Fractal size-number relation for circular patches modifies the rupture propagation and generates preferential direction of propagation as well as local correlation between rupture velocity and slip velocity. Therefore, the simulated STFs are expected to also show variable moment rate evolution. At the top of the Figure 4.13, we show the simulated STFs calculated for the six fault heterogeneity maps in Figure 4.11. The stochastic spatial distribution of the patches leads to different growth for each STF, with peak moment rates reached at various times. The phases leading to these peak moment rates, that we refer to as development phases in this manuscript, are also growing at different absolute times. As depicted by the colored moment rate evolution, the end of each realistic development phase corresponds to the time where rupture reaches fault bounds. Incidentally, this representation clearly outlines the interest of our method of calculating local moment accelerations at given moment rates. Indeed, development phases in Figure 4.13 have approximate similar growth but shifted in time, meaning that a local slope computation at a given time would have a value which depends on the start of the development phase.

We also verify that during the growth of the rupture process for each heterogeneity map, rupture behavior classically observed in real earthquakes is retrieved. Rupture velocity values are qualitatively inferred from the contours of the rupture front in Figure 4.11. Although rupture may locally propagate at supershear velocity, as on the left of the maps d) and f) at $\sim 3\,s$ and $\sim 4\,s$ respectively, most of the rupture propagations globally occur

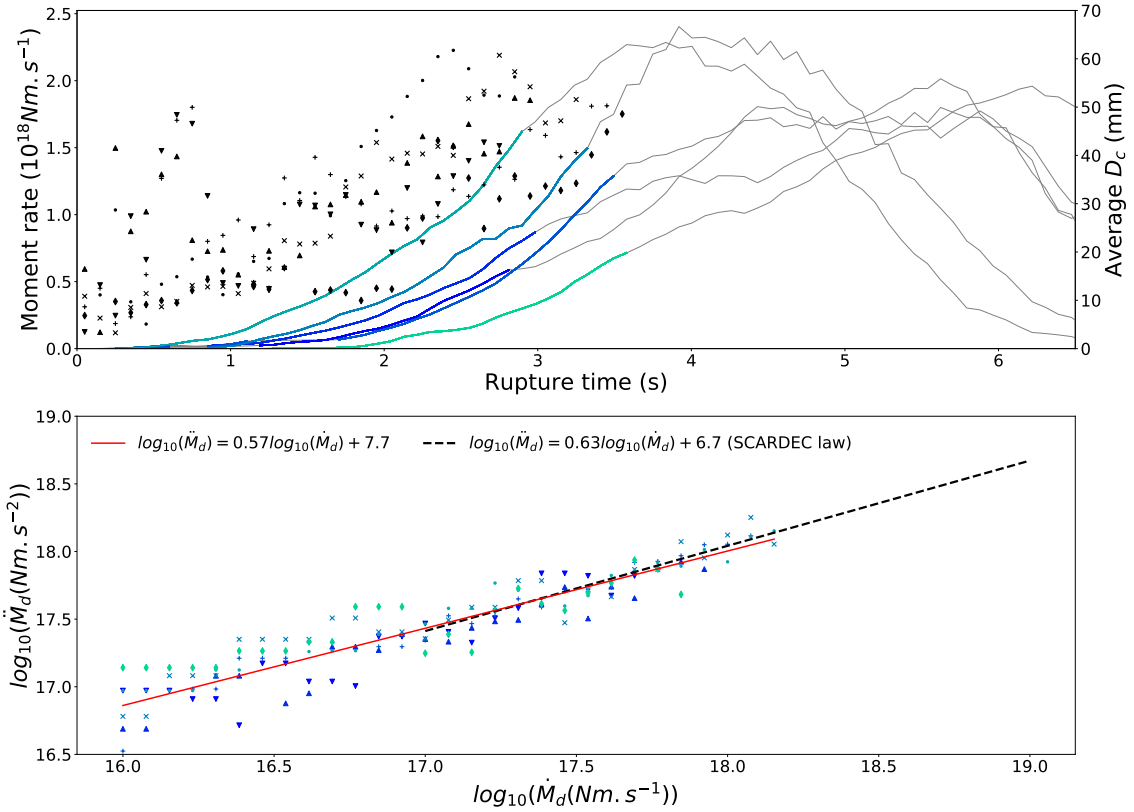

Figure 4.13 – Top: simulated STFs for the six heterogeneous maps in Figure 4.11 with colored development phases. For each STF, the average evolution of the D_c at the rupture front as a function of rupture time is represented by a specific marker. Bottom: Moment acceleration as a function of moment rate. Markers are individual moment acceleration values used to compute the linear fit. Red line is the linear fit calculated from the accelerations of the six STFs. Dotted black line is the fit to SCARDEC observations.

at subshear rupture velocities. As theoretically developed in Section 4.1.2 and observed in simulations in Section 4.2, such behavior of the rupture velocity is driven by a linear increase of D_c with the distance from hypocenter. In order to confirm this trend on our heterogeneous model, we plot at the top of the Figure 4.13 the moment rate together with the average D_c value at the rupture front as a function of time. Each marker style represents the average increase of D_c of one STF. On average, D_c value at the rupture front linearly increases with time, with variability due to complex D_c distribution. As the rupture velocity is globally constant, the increase of D_c on the rupture front as a function of distance from the hypocenter is also approximately linear. Stable subshear rupture velocity as well as linear trend for D_c with distance from the hypocenter therefore implies that at global scale rupture simulations are statistically self-similar.

We investigate the effect of heterogeneous D_c distribution on the development phase by computing the moment acceleration as a function of moment rate. The individual moment acceleration values for each STF are represented by a specific marker and color at the bottom of the Figure 4.13. The red linear fit is computed from the individual moment acceleration values of all STFs. The value of $m = 0.57$ is slightly lower than the slope of SCARDEC observations ($m = 0.63$), but substantially higher than the self-similar development phase ($m = 0.5$). In contrast with models of Sections 4.2 and 4.2.2 where

$m > 0.5$ were obtained only by introducing breaks in global self-similar assumptions, this current heterogeneous model shows non self-similar development phase despite global self-similar properties. Since the only difference between these models is the addition of heterogeneous fractal D_c distribution, we infer that this dynamic complexity is a first step towards the reproduction of the SCARDEC observations. As briefly discussed in the analysis of Figure 4.12, rupture is transiently accelerating when it propagates over small patches with small D_c overlying large patches with large D_c. Given that this local rupture velocity variability has a positive correlation with slip velocity, it generates steep moment accelerations that contribute to increase the m value. We therefore connect the variability of kinematic parameters such as rupture velocity and slip velocity (required to approach SCARDEC observations) to the dynamic effect of heterogeneous fractal D_c. However, additional dynamic complexities are likely necessary since the SCARDEC observations are not fully reproduced. As a consequence, we add in Section 4.4 random initial stress field in order to build more realistic rupture scenarios.

4.4 Combination of heterogeneities from random initial stress field and fractal fracture surface energy

4.4.1 Random spatial initial stress field

Besides heterogeneity of friction parameters such as D_c, variability in the rupture process also originates from heterogeneous initial stress field on the fault before the earthquake. While experimental (Nielsen et al., 2010; Latour et al., 2013) and numerical (Ripperger et al., 2007; Aochi and Ide, 2009) studies analyze its effect on rupture complexity, it is not straightforward to understand how these two dynamic parameters interact. The model of Aochi and Ide (2009) simulates the evolution of the initial stress field as a consequence of a sequence of earthquakes reproducing the classical view of seismic cycle. After each event, static stress change is computed over the fault plane meaning that the location of the next event is influenced by the new stress field redistribution. The initial stress field during the sequence therefore constantly evolves and is controlled by stress accumulation and release due to earthquake interaction. Inspired by works of Andrews (1980, 1981); Frankel (1991), the approach of Ripperger et al. (2007) for the distribution of the heterogeneous stress field is different, as they use a spectral description with power law decay at high wave numbers controlled by a correlation length. However, this dynamic model considers a scale-independent fracture energy with the purpose of investigating the effect of initial stress heterogeneity only, as we do for D_c heterogeneity in Section 4.3. We choose to use in this Section the approach of Ripperger et al. (2007) to generate heterogeneous initial stress field. Indeed, heterogeneous initial stress controlled by a sequence of earthquakes as in Aochi and Ide (2009) restricts the analysis to one seismic system, while the SCARDEC observations come from diverse tectonic contexts and periods.

Initial stress field is generated by selecting 64×64 random values corresponding to the spatial grids of the subspace on which rupture propagation is solved. A 2-D Fourier transform is performed in the spectral domain and a power decay at high wave numbers

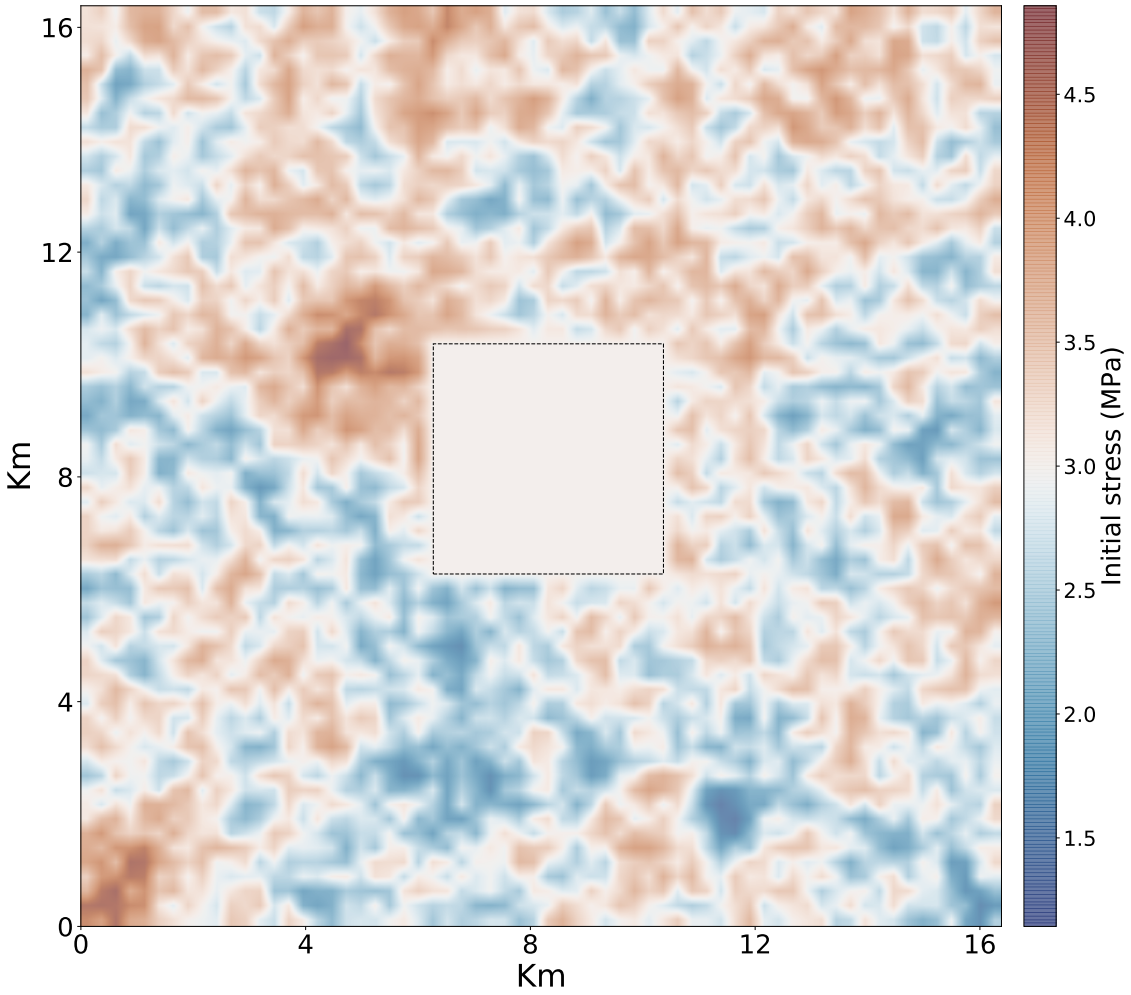

Figure 4.14 – Representation of the initial stress heterogeneity map from a spectral description with power law decay at high wave numbers controlled by a correlation length equal to the fault length L. Associated initial stress distribution is represented in Figure 4.15. Heterogeneous random initial stress is generated only in the last subspace on the fault, implying a constant initial stress in smaller subspaces as it is shown by the $L/4 \times L/4$ white square in the middle of the fault.

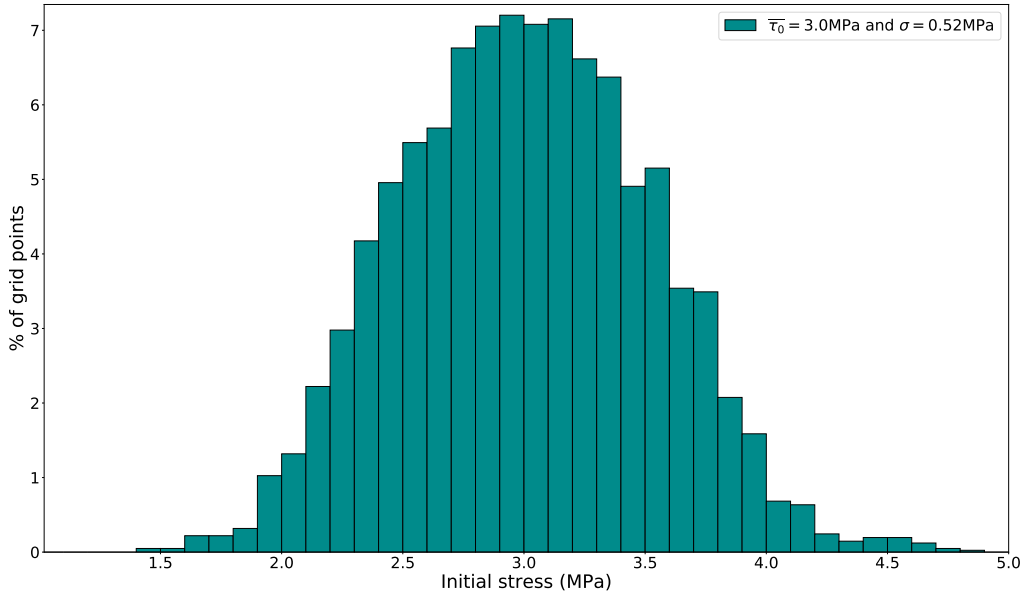

Figure 4.15 – Initial stress distribution for 64 × 64 grid points of the fault in Figure 4.14. Average initial stress $\overline{\tau_0}$ and standard deviation σ are equal to 3 MPa and 0.52 MPa respectively. Such σ is selected to have τ_0 values included between residual stress $\tau_1 = 0$ MPa and peak strength $\tau_y = 5$ MPa.

is imposed with the formulation:

$$\tau_0(k) \propto \frac{1}{1 + (k/k_c)^2} \quad \text{if } k > k_c \tag{4.11}$$

where $k = \sqrt{k_x^2 + k_y^2}$ with k_x and k_y the wave number components in the two spatial directions, and $k_c = 2\pi/L$ with L the fault length. At low wave numbers ($k < k_c$), random values are not modified. We then apply a 2-D inverse Fourier transform in order to retrieve the spatial distribution of τ_0. We finally add the average value $\overline{\tau_0}$ and adapt the standard deviation σ so that τ_0 is included between residual stress $\tau_1 = 0$ MPa and peak strength $\tau_y = 5$ MPa. Figure 4.14 represents one random realization of initial stress distribution for the last subscale of the fault. The correlation length L smooths the stress variation while it does not change the average stress value, as shown by Figure 4.15 with the τ_0 distribution. Average stress value is equal to $\overline{\tau_0} = 3$ MPa and $\sigma = 0.52$ MPa and distribution is Gaussian. We then keep the average initial stress field as in Section 4.3 except that we introduce variability leading to have areas with high (in red) and with low (in blue) initial stresses. In terms of slip-weakening friction law (Figure 4.2), a local increase of τ_0 puts a point closer to failure as it is closer to τ_y. In contrast, a point with local decrease of τ_0 requires higher stress accumulation before it can reach τ_y. We also note that as a consequence of the renormalization technique for the computation of the dynamic rupture, only the last subspace has heterogeneous random initial stress whereas smaller ones have a homogeneous $\tau_0 = 3$ MPa. It explains why in Figure 4.14 a square with dimension $L/4 \times L/4$ in the middle of the last subspace has no initial stress variation.

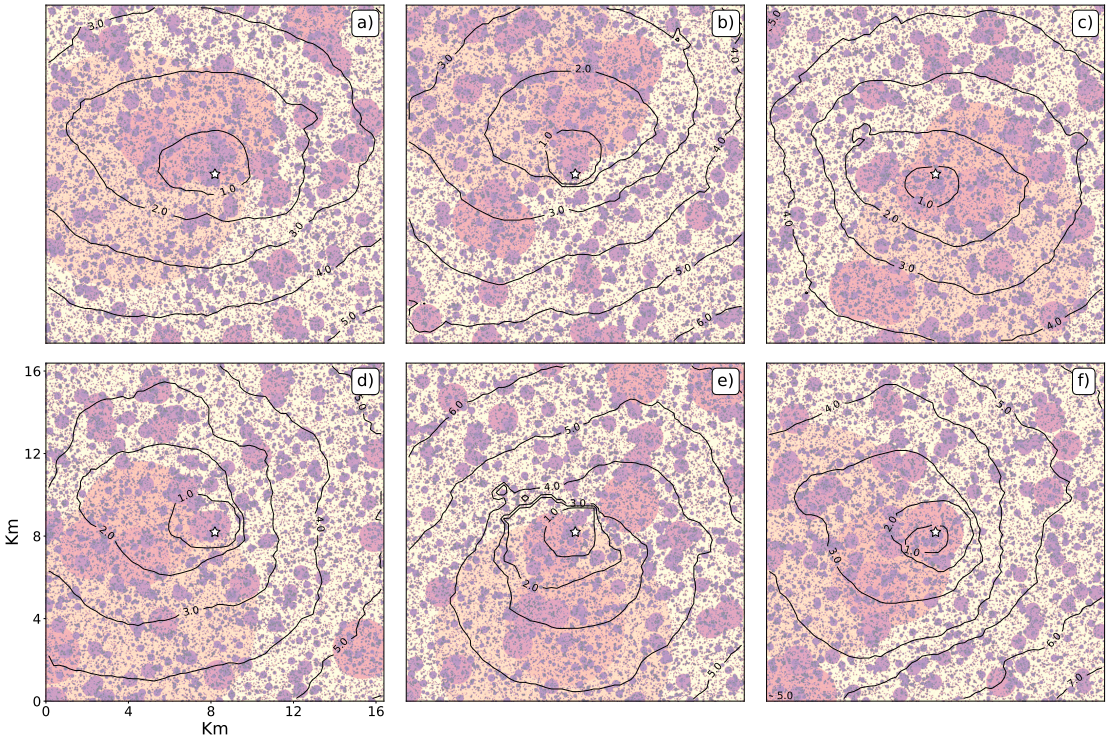

Figure 4.16 – Representation of six fault heterogeneity maps from a random circular patches position. Initial stress field is also heterogeneous and same as in Figure 4.14. White star is the position of the hypocenter. Colorbar and D_c heterogeneity map shown in b) are the same as in Figure 4.10. Black lines show the contours of the rupture front every second.

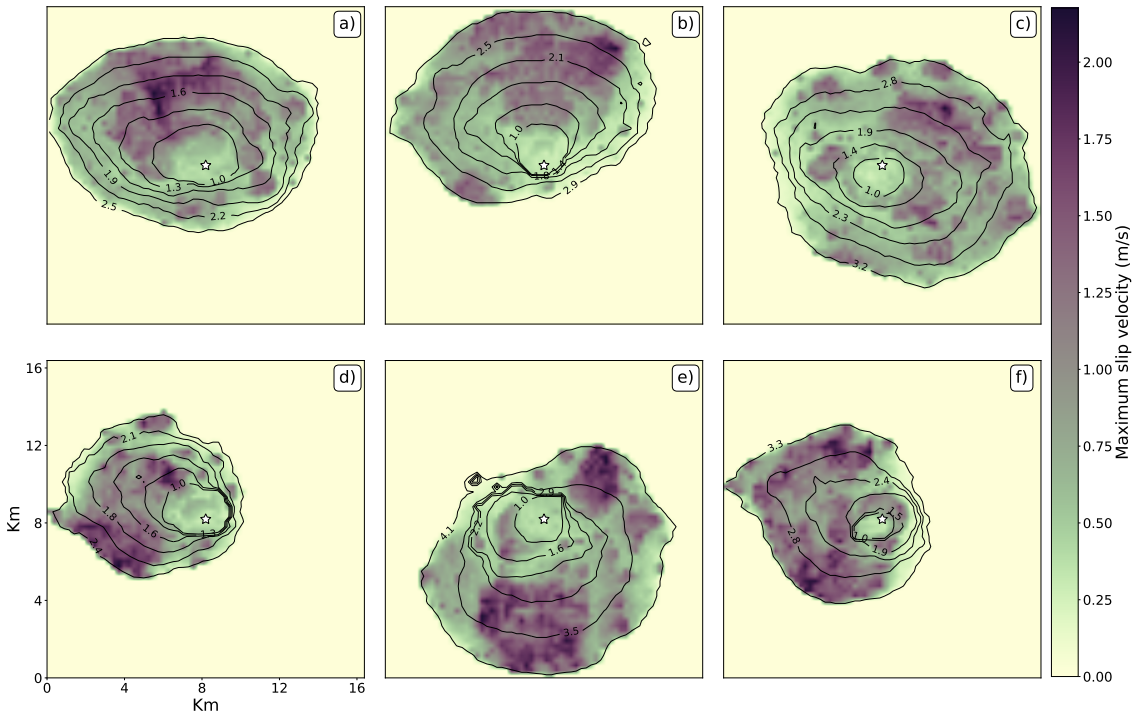

Figure 4.17 – Representation of the maximum slip velocity for the six simulations with D_c and τ_0 distribution in Figures 4.16 and 4.14, respectively. White star is the position of the hypocenter. Black lines show the contours of the rupture front for six different times. Maximum slip velocity is extracted before the rupture front reaches fault bounds.

4.4.2 Properties of the development phase for models combining heterogeneous D_c and τ_0 maps

We generate the same 6 heterogeneity maps of D_c as in Section 4.3 and we impose now the same heterogeneity map of τ_0 in Figure 4.14 for the 6 simulations. The result of these simulations in terms of rupture propagation is shown in Figure 4.16, and can be directly compared with Figure 4.11 in order to estimate the effect of heterogeneous τ_0. Contours of the rupture front every second shows even greater rupture complexity with very different local rupture velocities for the same rupture time. Although the preferential direction of propagation is still mainly controlled by the distribution of D_c, heterogeneous τ_0 produces more often supershear and very low rupture velocities. As an example, in a) of Figure 4.16, propagation to the left between 1 s and 2 s is locally supershear, which was not the case in a) of Figure 4.11. If looking at heterogeneous τ_0 in Figure 4.14, this clear acceleration corresponds to the location of high initial stress area. In contrast, we see in d) of Figure 4.16 that rupture propagation toward the bottom is more difficult than in d) of Figure 4.11 as a consequence of a low initial stress observed in Figure 4.14. We infer from these simulations that rupture velocity variability has two origins: as in Figure 4.11, when rupture propagates in largest patches, the break of smaller patches increases locally the rupture velocity. This effect is now accentuated or reduced if at the same location there is a high or low initial stress, respectively. However, τ_0 is on average the same and there is no correlation between distributions of D_c and τ_0. We then expect that although rupture velocity variability is higher than in Section 4.3, global rupture propagation is not modified. In order to confirm this hypothesis, we average the times at which ruptures reach the bounds for the six simulations. This average time is equivalent to the one for simulations in Figure 4.3, meaning the global average rupture velocity is the same with homogeneous and heterogeneous τ_0 distributions. Finally, Figure 4.17 shows also clear correlation between rupture velocity and slip velocity. However, in contrast with rupture velocity, we do not observe a higher slip velocity variability than in Figure 4.12. It would indicate that τ_0 has a more prominent effect on rupture velocity than on slip velocity.

The simulated STFs are represented at the top of the Figure 4.18, together with the average evolution of D_c at the rupture front (shown with markers). Such evolution confirms that despite more complex rupture propagation generated by heterogeneous τ_0, global rupture looks statistically self-similar as D_c increases with rupture time. As in Section 4.3, such evolution constrains the rupture velocity to keep a global constant subshear value. Heterogeneous τ_0 has a role on the development phase since colored moment rate evolution are not equivalent to the ones in Figure 4.13, meaning that the simulated STFs include the complex surface rupture expansion seen in Figure 4.16. We represent at the bottom of the Figure 4.18 the individual moment accelerations (colored markers) as a function of moment rate for each STF during the development phase. All the values are then used to compute the linear fit (in red) that we compare with the linear evolution of the SCARDEC observations (black dotted line). The value of $m = 0.61$ is very close to the SCARDEC observations ($m = 0.63$), as well as the intersect value $\log \beta$. Combination of both heterogeneous D_c and τ_0 are therefore shown to reproduce the observed development phase.

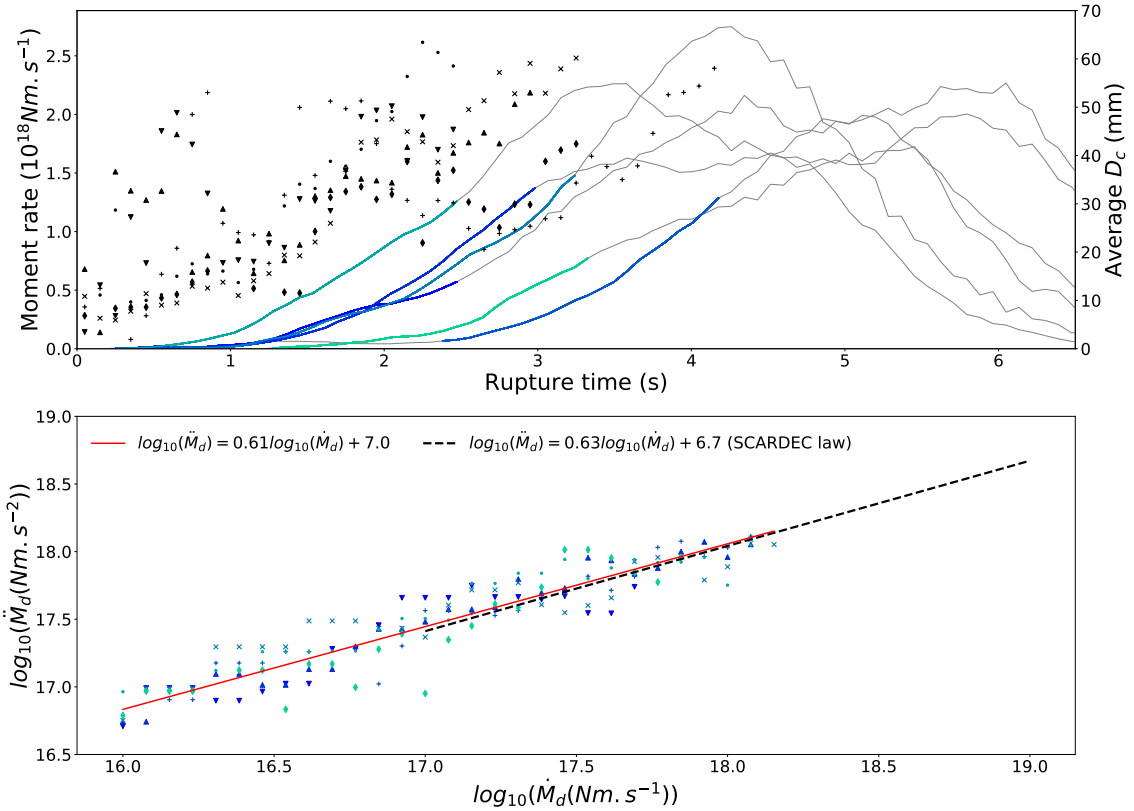

Figure 4.18 – Top: simulated STFs for the six heterogeneous maps in Figure 4.16 with colored development phases. Heterogeneous initial stress map is represented in Figure 4.14. For each STF, the average evolution of the D_c on the rupture front as a function of rupture time is represented by a specific marker. Bottom: Moment acceleration as a function of moment rate. Markers are individual moment acceleration values used to compute the linear fit. Red line is the linear fit calculated from the accelerations of the six STFs. Dotted black line is the fit from SCARDEC observations.

4.4.3 Discussion and conclusion

The dynamic model that we develop in this Section reproduces global and transient properties of the rupture process as a result of dynamic heterogeneities on the fault. As the rupture successively propagates into larger patches, D_c linearly increases with the hypocentral distance. This dynamic constraint affects the rupture velocity so that its average value remains stable during the rupture process. As a result of the random patches distribution, rupture preferentially breaks the most favorable D_c areas, leading to complex rupture propagation. For example, when part of the rupture front propagates into the largest patches, presence of overlying smaller patches locally increase the rupture velocity. In contrast, when part of the rupture front rapidly reaches the "background" D_{cmax}, the rupture velocity decreases. As the slip velocity is correlated with rupture velocity, such variability produces high moment accelerations. In addition to the dynamic effect of heterogeneous D_c, a random distribution of τ_0 also contributes to add complexity to the rupture propagation. Consistently with theoretical considerations, we observe that the effect of τ_0 is less critical, as written by Ripperger et al. (2007):"whereas G_c enters the "crack tip equation of motion", by its local value, stress drop contributes as a weighted spatial average through the integral defining the stress intensity factor". However, a high variability of τ_0 over the fault plane increases the complexity of the rupture propagation, which generates local accelerations and decelerations. These combined dynamic D_c and τ_0 heterogeneities result in high variability of the kinematic parameters and in particular of rupture velocity and slip velocity, which finally reproduce the SCARDEC observations. It is important to note there is no need for a spatial anti-correlation between τ_0 and D_c to approach observational data. If it were necessary, it would imply that static stress drop correlates with the size of patches, and the size of events, which would break the global self-similar assumption.

Conclusions et Perspectives

Synthèse des résultats

Les observables sismologiques enregistrés à travers les réseaux d'instruments mondiaux portent l'information sur le processus de rupture sismique. Grâce au développement de ces réseaux ainsi que de la qualité des instruments qui les composent, des analyses globales ont été menées sur la sismicité mondiale afin d'extraire les caractéristiques de la source sismique. Dans cet esprit, des méthodes ont été développées afin de créer des catalogues regroupant les paramètres principaux des séismes. La méthode SCARDEC (Vallée et al., 2011; Vallée and Douet, 2016) remplit ce rôle en retrouvant simultanément pour plus de 3000 séismes de $M_w > 5.7$ le mécanisme au foyer, le moment sismique, la profondeur et la fonction source. Cette dernière a un intérêt particulier puisqu'elle donne l'opportunité d'étudier l'histoire spatio-temporelle de la rupture. De plus, l'approche déconvolutive de la méthode SCARDEC permet de prendre en compte la complexité de la source en retrouvant les fonctions source apparentes à chaque station.

À partir du catalogue SCARDEC, plusieurs études se sont penchées sur l'analyse des paramètres de source macroscopiques (Vallée, 2013; Courboulex et al., 2016; Chounet et al., 2017; Chounet and Vallée, 2018), en s'attachant notamment à démontrer le comportement auto-similaire des séismes à l'échelle globale par le biais de l'estimation de la durée totale de la rupture T, de la chute de contrainte statique $\Delta\sigma$, de la vitesse de rupture V_r, de l'énergie radiée E_R. En outre, l'histoire temporelle du taux de moment décrite par les STFs donne l'opportunité d'étudier les comportements transitoires du processus de rupture, notamment la croissance moyenne des STFs. Meier et al. (2017) et Melgar and Hayes (2019) révèlent un comportement similaire de cette croissance, au moins jusqu'à ce qu'une proportion significative du moment sismique a été relâchée.

Cependant, l'observation des STFs indique que la croissance réelle d'un séisme peut se produire à des moments très différents dans le processus global. Une approche prenant pleinement en compte cette diversité des STFs est nécessaire pour étudier les propriétés physiques de la propagation de la rupture. Cette thèse s'est donc attachée à décrire le comportement de la phase menant aux épisodes principaux de relâchement du moment sismique, que nous avons nommée phase de développement. À l'instar des études portant sur le début des STFs, notre analyse a dans un premier temps pour but de déterminer si un signal déterministe est présent dans la phase de développement des séismes. Pour ce faire, 2221 STFs du catalogue SCARDEC ont été utilisées, en sélectionnant les événements peu profonds de mécanisme normal/inverse. Afin de ne pas utiliser l'information sur le temps

hypocentral, les accélérations de moment locales pour plusieurs taux de moment sont calculées au sein de la phase de développement. Ces mesures se révèlent être indépendantes de la magnitude, suggérant un processus où petits et grands séismes diffèrent uniquement par la durée de leur phase de développement.

Grâce à ces valeurs de pentes locales pour un ensemble de taux de moment, nous avons pu ensuite quantifier l'évolution moyenne du taux de moment $\dot{M}_d(t)$ en fonction du temps. Cette analyse estime que $\dot{M}_d(t)$ croît comme $\dot{M}_d(t) \propto t^{n_d}$ avec $n_d \simeq 2.7$ dans la phase de développement. Ce résultat indique que la croissance auto-similaire classique, où le taux de moment évolue en t^2 avec une vitesse de rupture et une chute de contrainte constantes, n'est pas adaptée à nos observations. La phase de développement est par conséquent une phase transitoire non auto-similaire, présente dans un processus plus global dont les propriétés macroscopiques respectent les conditions d'auto-similarité. Parmi les nombreux facteurs susceptibles d'expliquer ce comportement, nous avons développé analytiquement un modèle de crack où l'évolution spécifique du taux de moment est due à une augmentation de la vitesse de rupture de la forme $v_{rd}(t) \propto t^{0.2}$. Même si cette formulation permet d'atteindre très rapidement des valeurs de vitesse de rupture classiquement observées, elle implique que la vitesse de rupture augmente avec la durée de la phase développement. Étant donné que cette durée augmente également avec la magnitude, la vitesse de rupture augmenterait légèrement avec la taille finale des séismes, ce qui n'est pas confirmé par les observations. Cette corrélation a aussi le désavantage de briser la loi auto-similaire globale, qui considère une vitesse de rupture en moyenne constante pour tous les séismes.

Nous avons par la suite confronté nos observations à la vision cinématique de la rupture afin de mieux cerner les potentielles origines du comportement non auto-similaire de la phase de développement. Le catalogue *SRCMOD*, une base de données de distribution de glissement obtenue par inversion cinématique sur une faille finie, est exploitée afin d'étudier la variation spatiale de la chute de contrainte. À l'image de l'hypothèse précédente sur l'évolution de la vitesse de rupture, une augmentation de la chute de contrainte avec la durée de le phase de développement, et donc la magnitude, pourrait être à l'origine du signal non auto-similaire. Pour tous les modèles issus d'une inversion conjointe, la chute de contrainte statique est estimée sur la faille. Une valeur moyenne de cette chute de contrainte $\Delta\sigma_{main}$ est ensuite calculée au niveau des zones principales de glissement, représentant la phase de développement sur la faille. Les résultats de cette analyse ne suggèrent pas de corrélation entre $\Delta\sigma_{main}$ et la magnitude, et confirment donc qu'en moyenne une chute de contrainte constante pour tous les séismes est une propriété robuste du processus de rupture.

L'origine de l'évolution du taux de moment observée est également explorée dans un modèle de crack cinématique où une variabilité sur la vitesse de rupture radiale est ajoutée. Ce genre de modèle présente l'avantage de posséder des propriétés globales auto-similaires, avec une chute de contrainte constante (par définition du crack cinématique) et une vitesse de rupture distribuée autour d'une valeur moyenne équivalente pour tous les séismes. Par un processus brownien générant de manière stochastique des valeurs de vitesse de rupture en fonction de la durée de la rupture, nous créons des catalogues synthétiques de STFs pour une vitesse moyenne $\overline{v_r} = 2.5\,\mathrm{km.s^{-1}}$ avec une variabilité Δ et une valeur de chute de

contrainte $\Delta\sigma$ constante sur la faille. Afin d'explorer diverses configurations, nous adaptons le couple $(\Delta, \Delta\sigma)$ de manière à obtenir les valeurs optimales Δ_{opt} et $\Delta\sigma_{opt}$ reproduisant au mieux les observations. Lorsque les STFs synthétiques sont soumises à la même analyse que les observations issues du catalogue SCARDEC, c'est-à-dire une représentation de l'accélération de moment en fonction du taux de moment, nous déduisons que le couple $(\Delta_{opt}, \Delta\sigma_{opt})$ avec $\Delta_{opt} = 450\,\mathrm{m.s}^{-3/2}$ et $\Delta\sigma_{opt} = 1{-}3\,\mathrm{MPa}$ permet de retrouver l'évolution caractéristique de la phase de développement. Même si ce modèle possède des limitations car les variations de vitesse de rupture se font sur l'ensemble du front de rupture, une forte variation de la vitesse de rupture associée à une faible valeur de chute de contrainte expliquent relativement bien nos observations. La corrélation entre vitesse de rupture et vitesse de glissement induite par la formulation du crack est en particulier un ingrédient nécessaire à la génération de fortes valeurs d'accélération de moment. Cette corrélation est confirmée par des études dynamiques (Schmedes et al., 2010; Bizzarri, 2012).

Afin de prendre en compte la complexité spatiale du glissement qui n'est pas présente dans le modèle de crack circulaire, nous utilisons le modèle cinématique "composite" *RIK* développé par Ruiz et al. (2011) et mis à disposition par Gallovič (2016). Ce modèle génère des patches circulaires avec une relation fractale liant leur taille et leur nombre, et au sein desquels l'évolution spatiale du glissement est équivalente à la formulation du crack. Cette représentation d'un séisme implique que l'amplitude du spectre du glissement final décroît proportionnellement à k^{-2} pour les grands nombres d'ondes. Après une paramétrisation appropriée du modèle pour retrouver les propriétés auto-similaire globales de la source, des catalogues synthétiques de STFs sont générés pour une vitesse de rupture constante, une même distribution de patches et une localisation aléatoire des hypocentres sur la faille. Nous observons que différentes évolutions linéaires du temps de montée $\tau(R_n)$ en fonction du rayon des patches R_n ont un rôle important sur les valeurs d'accélération de moment dans la phase de développement. En comparaison avec les observations SCARDEC, une évolution avec des $\tau(R_n)$ courts génère de fortes accélérations de moment très tôt dans le processus de rupture tandis qu'une évolution avec des $\tau(R_n)$ plus longs produit de faibles accélérations de moment quand la rupture atteint des taux de moment importants. L'ajout dans le modèle *RIK* d'une vitesse de rupture variable, qui plus est corrélée avec la vitesse de glissement permet de se rapprocher des observations SCARDEC. Même si ces interprétations suggèrent que la corrélation entre vitesse de rupture et vitesse de glissement est de nouveau nécessaire pour reproduire des scénarios de ruptures réalistes, le modèle *RIK* ne reproduit pas totalement les observations SCARDEC.

L'étude dynamique de la rupture a l'avantage de fournir une description plus physique du processus, puisqu'elle traite de l'interaction entre les conditions de contraintes et la résistance à la friction, qui est à l'origine du glissement sur la faille. Dans cette optique, nous nous basons sur l'étude de Aochi and Ide (2004) en utilisant dans un premier temps une loi "slip-weakening" dans une configuration simple où le paramètre de friction D_c croît linéairement avec la distance à l'hypocentre et avec une contrainte initiale τ_0 homogène. Nous mettons en place une rapide étude paramétrique pour estimer l'évolution de D_c ainsi que la valeur de τ_0 requises en vue de générer des STFs avec des propriétés globale cohérentes. Au premier ordre, sur une faille de dimensions $16.384\,\mathrm{km} \times 16.384\,\mathrm{km}$, les simulations dynamiques indiquent qu'une augmentation linéaire de D_c de manière à

atteindre un $D_{cmax} = 128\,\text{mm}$ aux extrémités de la faille associée à $\tau_0 = 3\,\text{MPa}$ permettent d'obtenir des STFs simulées en accord avec les propriétés auto-similaires globales observées.

Dans un deuxième temps, nous intégrons ces contraintes sur D_c et τ_0 dans un modèle de distribution fractale de patches circulaires (Ide and Aochi, 2005), dans le but de générer des ruptures déclenchées en cascade (Okuda and Ide, 2018; Ide, 2019). Cette configuration est une première étape vers la description hétérogène d'un plan de faille, où la distribution des patches de rayons r_n associée à des D_{cn} participe à reproduire les irrégularités de topographie sur la faille. Des événements sont simulés sur plusieurs distributions aléatoires de patches et montrent une propagation complexe de la rupture avec une direction de propagation préférentielle contrôlée par la position des patches avec les plus faibles D_c. Lors de la propagation au sein des plus grands patches, la vitesse de rupture ainsi que la vitesse de glissement augmentent localement lorsque des plus petits patches superposés sont rompus. Cette corrélation est clairement visible dans les phases de développement, où l'accélération de moment en fonction du taux de moment montre un comportement non auto-similaire se rapprochant des observations SCARDEC.

Enfin, nous avons complété ce modèle en générant une distribution aléatoire de la contrainte initiale τ_0, en plus de la distribution fractale aléatoire de D_c. Cette configuration permet d'inclure deux types d'hétérogénéité et représente de manière statistique les conditions initiales les plus réalistes sur la faille. L'ajout d'un τ_0 variable rend la propagation de la rupture encore plus complexe, même si son rôle est moins déterminant que G_c dans la direction préférentielle de propagation. La variabilité de la vitesse de rupture s'accroît, et les STFs simulées montrent une accélération de moment en fonction du taux de moment qui s'approche de très près des observations SCARDEC. Ces résultats indiquent que le comportement des paramètres cinématiques (tel que la corrélation entre vitesse de rupture et vitesse de glissement) nécessaire à un comportement non auto-similaire est issu d'une forte hétérogénéité des paramètres dynamiques sur la faille. De plus, les lois auto-similaire globales sont retrouvées puisqu'en moyenne sur le front de rupture, D_c augmente linéairement avec la durée de la rupture, impliquant une vitesse de rupture moyenne constante tout au long du processus.

Perspectives d'amélioration des modèles

Ce paragraphe détaille les principaux axes de travail que nous aimerions développer afin d'apporter de nouvelles contraintes sur l'origine de l'évolution du taux de moment lors de la phase de développement exposée dans le Chapitre 2.

Dans la Section 3.2 du Chapitre 3, nous ajoutons une variation de vitesse radiale à partir de la formulation cinématique d'un crack circulaire. Pour ce faire, nous introduisons l'équation d'un bruit brownien en 1-D pour représenter l'évolution temporelle de la vitesse radiale, où l'amplitude de la variation par rapport au point précèdent est contrôlée par la variable aléatoire : $\mathcal{N}(0, \Delta^2 dt)$ dont la variance est égale au produit de l'intervalle temporel dt et Δ une variable à définir. C'est à partir de cette variable Δ que nous générons des vitesses de rupture plus ou moins variables, en considérant $dt = 0.1\,\text{s}$ constant. Par exemple, pour reproduire les observations SCARDEC, nous avons déduit que $\Delta = \Delta_{opt} = 450\,\text{m.s}^{-3/2}$.

Cependant, ce paramètre ne permet pas directement de quantifier la variabilité de la vitesse de rupture, car son unité n'est pas équivalente à une vitesse. De plus, la valeur Δ_{opt} est adaptée uniquement pour le dt choisi, car d'après l'équation ci-dessus, une valeur différente de dt affecte la variance de $\mathcal{N}$. Par conséquent, une formulation différente pourrait être introduite pour générer des vitesses de rupture aléatoires, de manière à ce que la variabilité soit dépendante d'une seule variable ayant pour dimension une vitesse. Il pourrait être alors possible de quantifier la variabilité nécessaire pour reproduire les observations SCARDEC. Puisque dans ce modèle, les variations de vitesse se font instantanément sur l'ensemble du front de rupture et dans une seule direction, cette variabilité serait considérée comme une valeur minimum. En effet, pour des modèles où la variation de la vitesse de rupture ne se fait que sur une partie du front de rupture, un gain de surface équivalent requiert une variabilité plus élevée. Enfin, afin de représenter de manière plus réaliste la complexité de la propagation de la rupture, une variation azimutale de la vitesse de rupture semble également nécessaire. Dans ce cas, il faudrait générer des gains de surface équivalents au crack avec variation de vitesse radiale, tout en conservant une chute de contrainte constante en arrière du front de rupture.

Le modèle RIK présenté en Section 3.3 du Chapitre 3 présente certains avantages, dont celui de représenter fidèlement une amplitude spectrale du glissement qui diminue de manière proportionnelle à k^{-2} pour les nombres d'ondes élevés. De plus, nous avons montré qu'il est possible de générer des catalogues de STFs qui respectent les lois auto-similaires. Néanmoins, la phase de développement, quel que soit le catalogue généré, n'explique pas les observations SCARDEC, malgré une corrélation entre vitesse de rupture et vitesse de glissement. Pour y remédier, nous estimons qu'à l'instar de la formulation du crack cinématique, l'histoire passée de la rupture doit contrôler sa propagation. Dans le cas du crack, l'expansion surfacique au cours du temps est systématiquement associée à une augmentation de la vitesse de glissement au niveau du front de rupture (avec la présence d'une zone de cohésion), conduisant à avoir des accélérations de moment corrélées au temps de rupture. Ce n'est pas le cas pour le modèle RIK où la localisation aléatoire de l'hypocentre peut entraîner une rupture anticipée des plus gros patches de glissement qui créent des fortes accélérations très tôt pendant la rupture. Une localisation plus réaliste des hypocentres, en particulier loin des plus grandes valeurs de glissement, pourrait permettre de régulièrement générer les fortes accélérations de moment à la fin de la phase de développement. Enfin, la loi linéaire reliant le temps de montée $\tau(R_n)$ au rayon des patches R_n pourrait être adaptée de manière à devenir $\tau(R_n) \propto R_n^{\eta}$ avec $\eta < 1$. Cette nouvelle relation aurait l'avantage d'avoir pour des petits R_n des $\tau(R_n)$ relativement longs produisant des accélérations de moment équivalentes à celle des observations SCARDEC pour de faibles taux de moment. En outre, la faible augmentation de $\tau(R_n)$ pour des grands R_n produiraient de fortes accélérations pour de grands taux de moment.

L'analyse des modèles dynamiques hétérogènes faite Sections 4.3 et 4.4 dans le Chapitre 4 met en lumière l'effet des paramètres dynamiques, D_c et τ_0 sur les paramètres cinématiques de la rupture tels que la vitesse de rupture et la vitesse de glissement. D'un point de vue statistique, cette analyse mériterait l'ajout de nouvelles distributions aléatoires de D_c afin d'effectuer notre analyse sur un plus grand nombre de STFs. Même si les propriétés globales des séismes semblent être auto-similaires, avec notamment une vitesse de rupture constante

au cours de la rupture, une analyse plus quantitative pourrait confirmer cette tendance. Par exemple, nous pourrions estimer l'évolution surfacique de la rupture en fonction du temps, qui devrait nous indiquer des variabilités locales de la vitesse de rupture tout en conservant une évolution globale en t^2. La loi fractale reliant le nombre de patches et leur taille pourrait également être modifiée de manière à diminuer ou augmenter le nombre de patches de plus petites tailles, tout en gardant la dimension fractale $D = 2$. D'après nos interprétations, lorsque la rupture se propage dans les plus gros patches, ce sont les patches de tailles inférieures à l'intérieur qui créent une variation locale de la vitesse de rupture et donc de la vitesse de glissement. Par conséquent, si leur nombre diffère, cet effet serait diminué ou accentué, et générerait probablement une évolution différente de l'accélération de moment dans la phase de développement.

Une seule carte d'hétérogénéité de τ_0 a été incluse dans notre analyse, avec une valeur d'écart-type donnée. Une confirmation robuste de nos résultats devrait inclure plusieurs cartes avec plusieurs valeurs d'écart-type, pour quantifier quelle variabilité pour τ_0 est attendue pour reproduire les observations SCARDEC. Aussi, à l'image de l'étude de Ripperger et al. (2007), plusieurs distributions stochastiques de τ_0 sont statistiquement représentatives des conditions sur la faille avant l'occurrence d'un séisme. Nous pourrions mettre en place ces différentes configurations et observer leur effet sur l'accélération de moment dans la phase de développement.

Implications et perspectives pour la dynamique de la rupture

La reproduction des observations SCARDEC a des implications sur les conditions dans lesquelles les séismes se produisent. La paramétrisation de notre modèle hétérogène nous permet de contraindre au premier ordre les valeurs des paramètres dynamiques qui génèrent des scénarios de rupture réalistes. Nous avons extrait une évolution spécifique de D_c qui représente la complexité intrinsèque moyenne d'une faille à partir de patches dont le nombre et la taille suivent une loi fractale. En considérant ces caractéristiques comme stables à l'échelle de plusieurs cycles sismiques, nos résultats peuvent servir de bases pour les inversions dynamiques de grands séismes dont l'objectif est de retrouver la localisation de ces principales aspérités. La génération de signaux synthétiques sera donc contrainte par les propriétés de la phase de développement extraites par notre étude.

La distribution exacte de la contrainte initiale sur la faille ne peut être déterminée avant l'occurrence d'un séisme. Cependant, nous estimons statistiquement que certaines propriétés de cette contrainte sont requises pour respecter les observations. L'une d'entre elles requiert une valeur intermédiaire de la variabilité pour générer des phases d'accélération transitoires avec de fortes accélérations de moment. Une faible valeur de l'écart-type ne permet pas de générer des ruptures suffisamment complexes. À l'inverse, une très grande valeur d'écart-type produirait des zones avec des contraintes négatives très défavorables à la propagation de la rupture, entraînant une probabilité très faible de rompre l'intégralité de la faille. Nos estimations ajoutent donc un ingrédient réaliste, qui peut directement être mis en lien avec la distribution de la contrainte initiale avant l'occurrence d'un grand séisme à la fin du cycle sismique.

D'un point de vue observationnel, l'évolution de l'accélération de moment ne respectant

pas l'auto-similarité peut également conduire à améliorer les études sur l'aléa sismique. La contribution de la complexité de la source sur la génération des mouvements du sol est encore mal estimée. Le lien entre la fonction source et le déplacement du sol en champ lointain implique que l'accélération de moment doit avoir une corrélation avec la vitesse du mouvement du sol. Les fortes accélérations locales observées dans notre étude devraient donc avoir une influence sur la valeur du "Peak Ground Velocity" (PGV). Les modèles de prédiction pourraient intégrer nos observations afin de mieux anticiper l'intensité du mouvement du sol.

Références

Abercrombie, R. and Leary, P. (1993). Source parameters of small earthquakes recorded at 2.5 km depth, cajon pass, southern california: implications for earthquake scaling. *Geophysical Research Letters*, 20(14):1511–1514.

Abercrombie, R. E., Poli, P., and Bannister, S. (2017). Earthquake directivity, orientation, and stress drop within the subducting plate at the hikurangi margin, new zealand. *Journal of Geophysical Research: Solid Earth*, 122(12).

Abercrombie, R. E. and Rice, J. R. (2005). Can observations of earthquake scaling constrain slip weakening? *Geophysical Journal International*, 162(2):406–424.

Aki, K. (1967). Scaling law of seismic spectrum. *Journal of geophysical research*, 72(4):1217–1231.

Aki, K. and Richards, P. G. (2002). *Quantitative seismology*. University Science Books.

Allen, R. M. and Kanamori, H. (2003). The potential for earthquake early warning in southern california. *Science*, 300(5620):786–789.

Allmann, B. P. and Shearer, P. M. (2009). Global variations of stress drop for moderate to large earthquakes. *Journal of Geophysical Research: Solid Earth*, 114(B1).

Andrews, D. (1976). Rupture velocity of plane strain shear cracks. *Journal of Geophysical Research*, 81(32):5679–5687.

Andrews, D. (1980). A stochastic fault model: 1. static case. *Journal of Geophysical Research: Solid Earth*, 85(B7):3867–3877.

Andrews, D. (1981). A stochastic fault model: 2. time-dependent case. *Journal of Geophysical Research: Solid Earth*, 86(B11):10821–10834.

Aochi, H., Fukuyama, E., and Matsu'ura, M. (2000). Spontaneous rupture propagation on a non-planar fault in 3-d elastic medium. *pure and applied geophysics*, 157(11-12):2003–2027.

Aochi, H. and Ide, S. (2004). Numerical study on multi-scaling earthquake rupture. *Geophysical Research Letters*, 31(2).

Aochi, H. and Ide, S. (2009). Complexity in earthquake sequences controlled by multiscale heterogeneity in fault fracture energy. *Journal of Geophysical Research: Solid Earth*, 114(B3).

Aochi, H. and Twardzik, C. (2019). Imaging of seismogenic asperities of the 2016 ml 6.0 amatrice, central italy, earthquake through dynamic rupture simulations. *Pure and Applied Geophysics*, pages 1–16.

Archuleta, R. J. and Ji, C. (2016). Moment rate scaling for earthquakes 3.3≤ m ≤5.3 with implications for stress drop. *Geophysical Research Letters*, 43(23).

Béjar-Pizarro, M., Carrizo, D., Socquet, A., Armijo, R., Barrientos, S., Bondoux, F., Bonvalot, S., Campos, J., Comte, D., De Chabalier, J., et al. (2010). Asperities and barriers on the seismogenic zone in north chile: state-of-the-art after the 2007 m w 7.7 tocopilla earthquake inferred by gps and insar data. *Geophysical Journal International*, 183(1):390–406.

Bernard, P., Herrero, A., and Berge, C. (1996). Modeling directivity of heterogeneous earthquake ruptures. *Bulletin of the Seismological Society of America*, 86(4):1149–1160.

Beroza, G. C. and Ellsworth, W. L. (1996). Properties of the seismic nucleation phase. *Tectonophysics*, 261(1-3):209–227.

Beroza, G. C. and Mikumo, T. (1996). Short slip duration in dynamic rupture in the presence of heterogeneous fault properties. *Journal of Geophysical Research: Solid Earth*, 101(B10):22449–22460.

Beroza, G. C. and Spudich, P. (1988). Linearized inversion for fault rupture behavior: Application to the 1984 morgan hill, california, earthquake. *Journal of Geophysical Research: Solid Earth*, 93(B6):6275–6296.

Bilek, S., Lay, T., and Ruff, L. (2004). Radiated seismic energy and earthquake source duration variations from teleseismic source time functions for shallow subduction zone thrust earthquakes. *Journal of Geophysical Research: Solid Earth*, 109(B9).

Bizzarri, A. (2012). Rupture speed and slip velocity: What can we learn from simulated earthquakes? *Earth and planetary science letters*, 317:196–203.

Boatwright, J. and Choy, G. L. (1992). Acceleration source spectra anticipated for large earthquakes in northeastern north america. *Bulletin of the Seismological Society of America*, 82(2):660–682.

Boore, D. M. (1983). Stochastic simulation of high-frequency ground motions based on seismological models of the radiated spectra. *Bulletin of the Seismological Society of America*, 73(6A):1865–1894.

Bouchon, M. (1976). Teleseismic body wave radiation from a seismic source in a layered medium. *Geophysical Journal International*, 47(3):515–530.

Bouchon, M. and Vallée, M. (2003). Observation of long supershear rupture during the magnitude 8.1 kunlunshan earthquake. *Science*, 301(5634):824–826.

Brune, J. N. (1970). Tectonic stress and the spectra of seismic shear waves from earthquakes. *Journal of geophysical research*, 75(26):4997–5009.

Burridge, R. and Willis, J. (1969). The self-similar problem of the expanding elliptical crack in an anisotropic solid. In *Mathematical Proceedings of the Cambridge Philosophical Society*, volume 66, pages 443–468. Cambridge University Press.

Causse, M., Dalguer, L., and Mai, P. M. (2013). Variability of dynamic source parameters inferred from kinematic models of past earthquakes. *Geophysical Journal International*, 196(3):1754–1769.

Chinnery, M. (1964). The strength of the earth's crust under horizontal shear stress. *Journal of Geophysical Research*, 69(10):2085–2089.

Chounet, A. (2018). Propriétés génériques du processus sismique derivée de l'analyse systématique des fonctions source. *PhD thesis*.

Chounet, A. and Vallée, M. (2018). Global and interregion characterization of subduction interface earthquakes derived from source time functions properties. *Journal of Geophysical Research: Solid Earth*, 123(7):5831–5852.

Chounet, A., Vallée, M., Causse, M., and Courboulex, F. (2017). Global catalog of earthquake rupture velocities shows anticorrelation between stress drop and rupture velocity. *Tectonophysics*.

Colombelli, S., Zollo, A., Festa, G., and Picozzi, M. (2014). Evidence for a difference in rupture initiation between small and large earthquakes. *Nature communications*, 5:3958.

Courboulex, F., Vallée, M., Causse, M., and Chounet, A. (2016). Stress-drop variability of shallow earthquakes extracted from a global database of source time functions. *Seismological Research Letters*, 87(4):912–918.

Dahlen, F. (1974). On the ratio of p-wave to s-wave corner frequencies for shallow earthquake sources. *Bulletin of the Seismological Society of America*, 64(4):1159–1180.

Danré, P., Yin, J., Lipovsky, B. P., and Denolle, M. A. (2019). Earthquakes within earthquakes: Patterns in rupture complexity. *Geophysical Research Letters*.

Das, S. and Aki, K. (1977). A numerical study of two-dimensional spontaneous rupture propagation. *Geophysical journal international*, 50(3):643–668.

Das, S. and Kostrov, B. (1983). Breaking of a single asperity: rupture process and seismic radiation. *Journal of Geophysical Research: Solid Earth*, 88(B5):4277–4288.

Denolle, M. A. (2019). Energetic onset of earthquakes. *Geophysical Research Letters*, 46(5):2458–2466.

Denolle, M. A. and Shearer, P. M. (2016). New perspectives on self-similarity for shallow thrust earthquakes. *Journal of Geophysical Research: Solid Earth*, 121(9):6533–6565.

Dong, G. and Papageorgiou, A. S. (2003). On a new class of kinematic models: symmetrical and asymmetrical circular and elliptical cracks. *Physics of the Earth and Planetary Interiors*, 137(1-4):129–151.

Doornbos, D. (1982). Seismic moment tensors and kinematic source parameters. *Geophysical Journal International*, 69(1):235–251.

Dunham, E. M. and Archuleta, R. J. (2004). Evidence for a supershear transient during the 2002 denali fault earthquake. *Bulletin of the Seismological Society of America*, 94(6B):S256–S268.

Dunham, E. M., Favreau, P., and Carlson, J. (2003). A supershear transition mechanism for cracks. *Science*, 299(5612):1557–1559.

Ekström, G., Nettles, M., and Dziewoński, A. (2012). The global cmt project 2004–2010: Centroid-moment tensors for 13,017 earthquakes. *Physics of the Earth and Planetary Interiors*, 200-201:1 – 9.

Ellsworth, W. and Beroza, G. (1995). Seismic evidence for an earthquake nucleation phase. *Science*, 268(5212):851–855.

Ellsworth, W. L. and Beroza, G. C. (1998). Observation of the seismic nucleation phase in the ridgecrest, california, earthquake sequence. *Geophysical research letters*, 25(3):401–404.

Eshelby, J. (1969). The elastic field of a crack extending non-uniformly under general anti-plane loading. *Journal of the Mechanics and Physics of Solids*, 17(3):177–199.

Frankel, A. (1991). High-frequency spectral falloff of earthquakes, fractal dimension of complex rupture, b value, and the scaling of strength on faults. *Journal of Geophysical Research: Solid Earth*, 96(B4):6291–6302.

Fukuyama, E. and Madariaga, R. (1998). Rupture dynamics of a planar fault in a 3d elastic medium: rate-and slip-weakening friction. *Bulletin of the Seismological Society of America*, 88(1):1–17.

Furumoto, M. and Nakanishi, I. (1983). Source times and scaling relations of large earthquakes. *Journal of Geophysical Research: Solid Earth*, 88(B3):2191–2198.

Galetzka, J., Melgar, D., Genrich, J. F., Geng, J., Owen, S., Lindsey, E. O., Xu, X., Bock, Y., Avouac, J.-P., Adhikari, L. B., et al. (2015). Slip pulse and resonance of the kathmandu basin during the 2015 gorkha earthquake, nepal. *Science*, 349(6252):1091–1095.

Gallovič, F. (2016). Modeling velocity recordings of the mw 6.0 south napa, california, earthquake: Unilateral event with weak high-frequency directivity. *Seismological Research Letters*, 87(1):2–14.

Gallovič, F. and Brokešová, J. (2007). Hybrid k-squared source model for strong ground motion simulations: Introduction. *Physics of the Earth and Planetary Interiors*, 160(1):34–50.

Geller, R. J. (1976). Scaling relations for earthquake source parameters and magnitudes. *Bulletin of the Seismological Society of America*, 66(5):1501–1523.

Hartzell, S. and Mendoza, C. (1991). Application of an iterative least-squares waveform inversion of strong-motion and teleseismic records to the 1978 tabas, iran, earthquake. *Bulletin of the Seismological Society of America*, 81(2):305–331.

Haskell, N. (1964). Total energy and energy spectral density of elastic wave radiation from propagating faults. *Bulletin of the Seismological Society of America*, 54(6A):1811–1841.

Hayes, G. P. (2017). The finite, kinematic rupture properties of great-sized earthquakes since 1990. *Earth and Planetary Science Letters*, 468:94–100.

Heaton, T. H. (1990). Evidence for and implications of self-healing pulses of slip in earthquake rupture. *Physics of the Earth and Planetary Interiors*, 64(1):1–20.

Houston, H. (2001). Influence of depth, focal mechanism, and tectonic setting on the shape and duration of earthquake source time functions. *Journal of Geophysical Research: Solid Earth*, 106(B6):11137–11150.

Houston, H., Benz, H. M., and Vidale, J. E. (1998). Time functions of deep earthquakes from broadband and short-period stacks. *Journal of Geophysical Research: Solid Earth*, 103(B12):29895–29913.

Husseini, M. I. (1977). Energy balance for motion along a fault. *Geophysical Journal International*, 49(3):699–714.

Ida, Y. (1972). Cohesive force across the tip of a longitudinal-shear crack and griffith's specific surface energy. *Journal of Geophysical Research*, 77(20):3796–3805.

Ide, S. (2019). Frequent observations of identical onsets of large and small earthquakes. *Nature*, 573(7772):112–116.

Ide, S. and Aochi, H. (2005). Earthquakes as multiscale dynamic ruptures with heterogeneous fracture surface energy. *Journal of Geophysical Research: Solid Earth*, 110(B11).

Ishihara, Y., Fukao, Y., Yamada, I., and Aoki, H. (1992). Rising slope of moment rate functions: the 1989 earthquakes off east coast of honshu. *Geophysical research letters*, 19(9):873–876.

Kanamori, H. (1977). The energy release in great earthquakes. *Journal of geophysical research*, 82(20):2981–2987.

Kanamori, H. (2004). The diversity of the physics of earthquakes. *Proceedings of the Japan Academy, Series B*, 80(7):297–316.

Kanamori, H. and Anderson, D. L. (1975). Theoretical basis of some empirical relations in seismology. *Bulletin of the seismological society of America*, 65(5):1073–1095.

Kanamori, H. and Rivera, L. (2008). Source inversion ofwphase: speeding up seismic tsunami warning. *Geophysical Journal International*, 175(1):222–238.

Kennett, B. and Engdahl, E. (1991). Traveltimes for global earthquake location and phase identification. *Geophysical Journal International*, 105(2):429–465.

Kiser, E. and Ishii, M. (2011). The 2010 mw 8.8 chile earthquake: Triggering on multiple segments and frequency-dependent rupture behavior. *Geophysical Research Letters*, 38(7).

Kostrov, B. (1964). Selfsimilar problems of propagation of shear cracks. *Journal of Applied Mathematics and Mechanics*, 28(5):1077–1087.

Lancieri, M., Madariaga, R., and Bonilla, F. (2012). Spectral scaling of the aftershocks of the tocopilla 2007 earthquake in northern chile. *Geophysical Journal International*, 189(1):469–480.

Latour, S., Voisin, C., Renard, F., Larose, E., Catheline, S., and Campillo, M. (2013). Effect of fault heterogeneity on rupture dynamics: An experimental approach using ultrafast ultrasonic imaging. *Journal of Geophysical Research: Solid Earth*, 118(11):5888–5902.

Lykotrafitis, G., Rosakis, A. J., and Ravichandran, G. (2006). Self-healing pulse-like shear ruptures in the laboratory. *Science*, 313(5794):1765–1768.

Madariaga, R. (1976). Dynamics of an expanding circular fault. *Bulletin of the Seismological Society of America*, 66(3):639–666.

Mai, P., Somerville, P., Pitarka, A., Dalguer, L., Song, S., Beroza, G., Miyake, H., Irikura, K., Abercrombie, R., McGarr, A., et al. (2006). On scaling of fracture energy and stress drop in dynamic rupture models: Consequences for near-source ground-motions. *GEOPHYSICAL MONOGRAPH-AMERICAN GEOPHYSICAL UNION*, 170:283.

Mai, P. M. and Beroza, G. C. (2000). Source scaling properties from finite-fault-rupture models. *Bulletin of the Seismological Society of America*, 90(3):604–615.

Mai, P. M. and Beroza, G. C. (2002). A spatial random field model to characterize complexity in earthquake slip. *Journal of Geophysical Research: Solid Earth*, 107(B11):ESE–10.

Mai, P. M. and Thingbaijam, K. (2014). SRCMOD: An online database of finite-fault rupture models. *Seismological Research Letters*, 85(6):1348–1357.

McGuire, J. J. (2004). Estimating finite source properties of small earthquake ruptures. *Bulletin of the Seismological Society of America*, 94(2):377–393.

McGuire, J. J., Zhao, L., and Jordan, T. H. (2002). Predominance of unilateral rupture for a global catalog of large earthquakes. *Bulletin of the Seismological Society of America*, 92(8):3309–3317.

Meier, M.-A., Ampuero, J., and Heaton, T. H. (2017). The hidden simplicity of subduction megathrust earthquakes. *Science*, 357(6357):1277–1281.

Meier, M.-A., Heaton, T., and Clinton, J. (2016). Evidence for universal earthquake rupture initiation behavior. *Geophysical Research Letters*, 43(15):7991–7996.

Melgar, D. and Hayes, G. P. (2017). Systematic observations of the slip pulse properties of large earthquake ruptures. *Geophysical Research Letters*, 44(19):9691–9698.

Melgar, D. and Hayes, G. P. (2019). Characterizing large earthquakes before rupture is complete. *Science Advances*, 5(5):eaav2032.

Meng, L., Ampuero, J.-P., Stock, J., Duputel, Z., Luo, Y., and Tsai, V. (2012). Earthquake in a maze: Compressional rupture branching during the 2012 mw 8.6 sumatra earthquake. *Science*, 337(6095):724–726.

Müller, G. (1985). The reflectivity method: a tutorial. *Journal of Geophysical Research*.

Nielsen, S. and Madariaga, R. (2003). On the self-healing fracture mode. *Bulletin of the Seismological Society of America*, 93(6):2375–2388.

Nielsen, S., Taddeucci, J., and Vinciguerra, S. (2010). Experimental observation of stick-slip instability fronts. *Geophysical Journal International*, 180(2):697–702.

Noda, H., Nakatani, M., and Hori, T. (2013). Large nucleation before large earthquakes is sometimes skipped due to cascade-up—implications from a rate and state simulation of faults with hierarchical asperities. *Journal of Geophysical Research: Solid Earth*, 118(6):2924–2952.

Ohnaka, M. and Yamashita, T. (1989). A cohesive zone model for dynamic shear faulting based on experimentally inferred constitutive relation and strong motion source parameters. *Journal of Geophysical Research: Solid Earth*, 94(B4):4089–4104.

Okuda, T. and Ide, S. (2018). Hierarchical rupture growth evidenced by the initial seismic waveforms. *Nature communications*, 9(1):3714.

Olson, E. L. and Allen, R. M. (2005). The deterministic nature of earthquake rupture. *Nature*, 438(7065):212.

Orowan, E. (1960). Mechanism of seismic faulting. *Rock deformation*, 79:323–345.

Podvin, P. and Lecomte, I. (1991). Finite difference computation of traveltimes in very contrasted velocity models: a massively parallel approach and its associated tools. *Geophysical Journal International*, 105(1):271–284.

Ripperger, J., Ampuero, J.-P., Mai, P., and Giardini, D. (2007). Earthquake source characteristics from dynamic rupture with constrained stochastic fault stress. *Journal of Geophysical Research: Solid Earth*, 112(B4).

Rubin, A. M. and Ampuero, J.-P. (2005). Earthquake nucleation on (aging) rate and state faults. *Journal of Geophysical Research: Solid Earth*, 110(B11).

Rubino, V., Rosakis, A., and Lapusta, N. (2017). Understanding dynamic friction through spontaneously evolving laboratory earthquakes. *Nature communications*, 8:15991.

Ruff, L. J. (1999). Dynamic stress drop of recent earthquakes: Variations within subduction zones. In *Seismogenic and Tsunamigenic Processes in Shallow Subduction Zones*, pages 409–431. Springer.

Ruiz, J., Baumont, D., Bernard, P., and Berge-Thierry, C. (2011). Modelling directivity of strong ground motion with a fractal, k- 2, kinematic source model. *Geophysical Journal International*, 186(1):226–244.

Sato, R. (1972). Stress drop for a finite fault. *Journal of Physics of the Earth*, 20(4):397–407.

Sato, T. (1994). Seismic radiation from circular cracks growing at variable rupture velocity. *Bulletin of the Seismological Society of America*, 84(4):1199–1215.

Sato, T. and Hirasawa, T. (1973). Body wave spectra from propagating shear cracks. *Journal of Physics of the Earth*, 21(4):415–431.

Savage, J. and Wood, M. (1971). The relation between apparent stress and stress drop. *Bulletin of the Seismological Society of America*, 61(5):1381–1388.

Scherbaum, F. and Bouin, M.-P. (1997). Fir filter effects and nucleation phases. *Geophysical Journal International*, 130(3):661–668.

Schmedes, J., Archuleta, R. J., and Lavallée, D. (2010). Correlation of earthquake source parameters inferred from dynamic rupture simulations. *Journal of Geophysical Research: Solid Earth*, 115(B3).

Somerville, P., Irikura, K., Graves, R., Sawada, S., Wald, D., Abrahamson, N., Iwasaki, Y., Kagawa, T., Smith, N., and Kowada, A. (1999). Characterizing crustal earthquake slip models for the prediction of strong ground motion. *Seismological Research Letters*, 70(1):59–80.

Tanioka, Y. and Ruff, L. J. (1997). Source time functions. *Seismological Research Letters*, 68(3):386–400.

Tinti, E., Fukuyama, E., Piatanesi, A., and Cocco, M. (2005). A kinematic source-time function compatible with earthquake dynamics. *Bulletin of the Seismological Society of America*, 95(4):1211–1223.

Uchide, T. and Ide, S. (2010). Scaling of earthquake rupture growth in the parkfield area: Self-similar growth and suppression by the finite seismogenic layer. *Journal of Geophysical Research: Solid Earth*, 115(B11).

Vallée, M. (2013). Source time function properties indicate a strain drop independent of earthquake depth and magnitude. *Nature communications*, 4:2606.

Vallée, M., Charléty, J., Ferreira, A. M., Delouis, B., and Vergoz, J. (2011). Scardec: a new technique for the rapid determination of seismic moment magnitude, focal mechanism and source time functions for large earthquakes using body-wave deconvolution. *Geophysical Journal International*, 184(1):338–358.

Vallée, M. and Douet, V. (2016). A new database of source time functions (stfs) extracted from the scardec method. *Physics of the Earth and Planetary Interiors*, 257:149–157.

Vassiliou, M. and Kanamori, H. (1982). The energy release in earthquakes. *Bulletin of the Seismological Society of America*, 72(2):371–387.

Venkataraman, A. and Kanamori, H. (2004). Effect of directivity on estimates of radiated seismic energy. *Journal of Geophysical Research: Solid Earth*, 109(B4).

Vidale, J. E. and Houston, H. (1993). The depth dependence of earthquake duration and implications for rupture mechanisms. *Nature*, 365(6441):45.

Yagi, Y. (2004). Source rupture process of the 2003 tokachi-oki earthquake determined by joint inversion of teleseismic body wave and strong ground motion data. *Earth, planets and space*, 56(3):311–316.

Ye, L., Lay, T., Kanamori, H., and Rivera, L. (2016). Rupture characteristics of major and great (mw $\geq$ 7.0) megathrust earthquakes from 1990 to 2015: 1. source parameter scaling relationships. *Journal of Geophysical Research: Solid Earth*, 121(2):826–844.

Yoffe, E. H. (1951). Lxxv. the moving griffith crack. *The London, Edinburgh, and Dublin Philosophical Magazine and Journal of Science*, 42(330):739–750.

Zeng, Y., Anderson, J. G., and Yu, G. (1994). A composite source model for computing realistic synthetic strong ground motions. *Geophysical Research Letters*, 21(8):725–728.

Zhang, G., Vallée, M., Shan, X., and Delouis, B. (2012). Evidence of sudden rupture of a large asperity during the 2008 mw7. 9 wenchuan earthquake based on strong motion analysis. *Geophysical Research Letters*, 39(17).

Zheng, G. and Rice, J. R. (1998). Conditions under which velocity-weakening friction allows a self-healing versus a cracklike mode of rupture. *Bulletin of the Seismological Society of America*, 88(6):1466–1483.

Zollo, A., Lancieri, M., and Nielsen, S. (2006). Earthquake magnitude estimation from peak amplitudes of very early seismic signals on strong motion records. *Geophysical Research Letters*, 33(23).

Résumé

Notre compréhension de la physique de la source sismique, qui donne naissance à des séismes de toute magnitude, requiert l'observation d'une large population d'événements. Les méthodes d'analyse systématique de la sismicité mondiale remplissent ce rôle et permettent d'extraire les propriétés des séismes puis de les confronter aux modèles de rupture sismique. La méthode SCARDEC fait partie de ces méthodes et retrouve les fonctions source d'événements sur une large gamme de magnitudes ($M_w > 5.7$). La fonction source, puisqu'elle décrit l'évolution temporelle du taux de moment, est un observable privilégié pour l'analyse des propriétés transitoires de la rupture. L'objectif de notre étude est d'observer le développement de la rupture lors de ces séismes afin de plus précisément contraindre les modèles cinématiques et dynamiques de la source. La première partie de notre travail s'intéresse au développement des séismes à partir du catalogue SCARDEC. La phase menant au pic de la fonction source ("phase de développement") est extraite pour caractériser son évolution. À partir du calcul des accélérations de moment pour des taux de moment donnés, nous observons que l'évolution du taux de moment pendant la phase de développement est indépendante de la magnitude finale. Une analyse quantitative de l'augmentation du taux de moment en fonction du temps indique que cette phase ne respecte pas la dépendance en t^2 de la loi auto-similaire, suggérant une variation transitoire de la vitesse de rupture et/ou de la chute de contrainte. Ces observations sont dans un deuxième temps confrontées aux modèles cinématiques de la source. Un modèle de crack avec des variations radiales de la vitesse de rupture, associées à une faible chute de contrainte, met en évidence que la corrélation entre vitesse de rupture et vitesse de glissement est un ingrédient nécessaire au comportement transitoire de la phase de développement vu dans les observations. Nous générons ensuite à partir du modèle composite fractal RIK des catalogues synthétiques de fonctions source. Ces derniers montrent également que la corrélation entre la vitesse de rupture et la vitesse de glissement, ainsi que la durée du temps de montée, ont une influence sur les valeurs de l'accélération de moment. Nous développons finalement des modèles dynamiques hétérogènes qui prennent en compte la physique de la rupture. Les distributions hétérogènes du paramètre de friction D_c et de la contrainte initiale τ_0 sur la faille participent à générer des scénarios de rupture particulièrement réalistes. La propagation de la rupture est en particulier influencée par ces deux paramètres dynamiques qui entraînent une direction de propagation préférentielle couplée à une variabilité plus locale de la vitesse de rupture. La corrélation entre vitesse de rupture et vitesse de glissement, mise en lumière dans les modèles cinématiques précédents, est retrouvée et permet la reproduction des observations SCARDEC. Ces résultats devraient fournir des contraintes additionnelles pour la constitution de scenarios réalistes de la dynamique de la rupture.

Summary

Our knowledge of earthquake source physics, giving rise to events of very different magnitudes, requires observations of a large population of earthquakes. The development of systematic analysis tools for the global seismicity meets these expectations, and allows us to extract the generic properties of earthquakes, which can then be integrated into models of the rupture process. Following this approach, the SCARDEC method is able to retrieve source time functions of events on a large range of magnitude ($M_w > 5.7$). The source time function (which describes the temporal evolution of the moment rate) is suitable for the analysis of transient rupture properties which provide insights into the generation of earthquakes of various sizes. The purpose of our study is to observe the rupture development of such earthquakes in order to add better constraints on kinematic and dynamic source models. The first part of our work focuses on the development of earthquakes through the analysis of the SCARDEC catalog. The phase leading to the peak of the source time function ("development phase") is extracted to characterize its evolution. From the computation of moment accelerations at prescribed moment rates, we observe that the evolution of the moment rate during the developement phase is independent of the final magnitude. A quantitative analysis of the moment rate increase as a function of time further indicates that this phase does not respect the steady t^2 self-similar growth, suggesting a transient variation of rupture velocity and/or stress drop. In a second part, these observations are compared with kinematic source models. A crack model with radial variations of the rupture velocity combined with low stress drop highlights that correlation between rupture velocity and slip velocity is a key feature for the transient behavior of the development phase previously observed. We then generate, using the composite fractal RIK model, synthetic catalogs of source time functions. This also supports that the correlation between rupture velocity and slip velocity, as well as the duration of the rise-time, have a strong effect on moment acceleration values. We finally develop heterogeneous dynamic models which take into consideration rupture physics. Heterogeneous distributions of the friction parameter D_c and the initial stress τ_0 contribute to generate highly realistic rupture scenarios. Rupture propagation is strongly influenced by these two dynamic parameters which induce a clear preferential direction of propagation together with a local variability of the rupture velocity. The correlation between rupture velocity and slip velocity highlighted by the previous kinematic models is retrieved and allows to reproduce the SCARDEC observations. These findings are expected to put further constraints on future realistic dynamic rupture scenarios.